EVALUATION OF UV-PCO AIR CLEANERS PERFORMANCE
AT LOW LEVEL VOCS CONCENTRATION

Alireza Aghighi

A Thesis

in

The Department

of

Building, Civil and Environmental Engineering

Presented in Partial Fulfillment of the Requirements

For the Degree of Master of Applied Science (Civil Engineering)

at Concordia University, Montréal, Québec, Canada

August 2013

CONCORDIA UNIVERSITY
School of Graduate Study

This is to certify that the thesis prepared

By: **Alireza Aghighi**

Entitled: **Evaluation of UV-PCO Air Cleaners Performance at Low Level VOCs Concentration**

and submitted in partial fulfillment of the requirements for the degree of

Master of Applied Science (Civil Engineering)

complies with the regulations of the University and meets the accepted standards with respect to originality and quality.

Signed by the final examining committee:

_____ Chair
Dr. Catherine Mulligan

_____ Examiner
Dr. Kudret Demirli

_____ Examiner
Dr. Zhi Chen

_____ Supervisor
Dr. Fariborz Haghighat

Approved by _____
        Chair of Department or Graduate Program Director

       _____
        Dean of Faculty

Date   _____

ABSTRACT

Evaluation of UV-PCO Air Cleaners Performance at low level VOCs Concentration

Alireza Aghighi

Volatile organic compounds (VOCs) constitute the vast majority of indoor air contaminants. In design of ultraviolet photo-catalytic oxidation (UV-PCO) air cleaner system, the focus must be in selecting an appropriate catalyst that can transform all contaminants to harmless gases. Some produced contaminants may promote or inhibit the photocatalytic reactions, or even lead to deactivation of the catalyst. The PCO reactions of two classes of VOCs, light alcohols and alkanes (C_5-C_{10}) were studied with different types of nano titanium dioxide catalysts. The influence of relative humidity on oxidation rate of tested VOCs was discussed in detail to establish ideal operational conditions for the selected group of VOCs.

A series of laboratory experiments was conducted with a pilot four-parallel duct system setup to test the VOCs in very low concentration levels which represents a typical indoor air environment. The experiments were carried out with different types of nano TiO_2 catalysts with UV lamps. A new type of titanium dioxide catalyst was specifically developed for this study to enhance the efficiency of PCO system. A systematic method was used to develop and test the synthesized photocatalysts, which helped to improve the overall performance of test system. The performance of different catalysts was studied at different humidity conditions and different VOCs concentrations.

The research objective was to develop a correlation between the PCO kinetic rate constants and physical characteristics of indoor VOCs. These correlations may be employed to eliminate the need of further experiments with every individual VOCs and they also could facilitate the design process of future PCO air cleaner. The physical characteristics of VOCs were used to estimate the performance of the PCO catalysts in a steady-state environmental test condition. The photocatalytic removal efficiency of VOCs and formation of intermediates and byproducts were studied with and without ozone generation UV lamps.

ACKNOWLEDGMENTS

Table of Contents

List of Figures

List of Tables

Nomenclature

Abbreviations

a	Superficial gas exposed catalyst surface area (m^2)
A	Area (cm^2)
ASHRAE	American society of heating, refrigerating and air-conditioning engineers
b.p.	Boiling point (ºC)
BET	Stephen brunauer, paul hugh emmett, and edward teller
C	Concentration (mg/m^3); BET constant
CB	Conduction band
cfm	Cubic feet per minute
CNS	Central nervous system
D	Diffusion coefficient (cm^2/s)
DAS	Data acquisition system
DFT	Density function theory
D_e	Effective diffusion ($D_e = (\varepsilon_p D)/\tau_p$)
e	Electron
E	Energy (J)
d	Hydraulic diameter; active site surface density
GC	Gas chromatograph
HAP	Hazardous air pollutants
HEPA	High efficiency particulate air
h	Hole; planck's constant ($h = 6.626 \times 10^{-34}$ J.s)
hv	Planck equation ($E = hv$)
HVAC	Heating, ventilating and air-conditioning
i	Diffraction peak intensity (a.u.)
I	Light Intensity (mW/cm^2)
IE (IP)	Ionization energy (formerly called *ionization potential*), (eV)
k	Apparent mass transfer coefficient; k_f external mass transfer ($mol/m^2.s$)
K	Langmuir adsorption equilibrium constant (m^3/mg); kinetic coefficient
l	Virtual thickness of the hydrodynamic boundary layer (cm)
L-H	Langmuir-hinshelwood
LPG	Liquefied petroleum gas
m	Mass of catalyst (g)
MS	Mass spectrometer
MW	Molecular weight (g/mol)

n	number of active sites on the catalyst; order of reaction rate
N	Avogadro's number (6.023×10^{23} molecules.mol^{-1})
nc	Neutral center
NIH	U.S. national institutes of health
P	Pressure (atm)
PCO	Photocatalytic oxidation
ppb	Part per billion
ppm	Part per million
PTFE	Polytetrafluoroethylene
r	Reaction rate (mol/s)
RH	Relative humidity (%)
RSD	Relative standard deviation (%)
S	Specific surface area (m^2)
SEM	Scanning electron microscope
SG	Sol-Gel
SRR	Structure reactivity relationship
T	Temperature (ºC)
t	Time (s)
TD	Thermal desorber
TEM	Transmission electron microscopy
TVOC	Total volatile organic compound
UV	Ultraviolet
UVC	Ultraviolet (electromagnetic radiation subtype C)
UVGI	Ultraviolet germicidal irradiation
V	Volume (L)
v	Frequency (Hz)
VAC	Voltage alternating current (A)
VB	Valence band
VUV	Vacuum ultraviolet
VOC	Volatile organic compound
UV-PCO	Ultraviolet photocatalytic oxidation
x	Weight fraction
XRPD	X-ray powder diffraction
W	Weight of adsorbed gas (mg)
WHO	World health organization

Dimensionless numbers

Ca	Carberry number ($Ca = r/k_f.a.C_{bulk}$)
Sc	Schmidt number ($Sc = \mu/\rho.D$)
Sh	Sherwood number ($Sh = kf.dp/D$)
Da	Damköhler number (ratio of the k_{PCO} to the mass transfer rate)
Re	Reynolds number ($Re = v\rho d/\mu$)
J-factor	$Sh/Re.Sc^{1/3}$

Greek letters

β	Half width of maximum intensity
θ	Surface coverage; diffraction angle (º)
Φ	Thiele modulus
Ψ	Weisz modulus
ε	pore fraction (porosity)
λ	Wavelength (nm)
τ	Tortuosity factor; residence time (ms); particle diameter (μm)
μ	Viscosity (kg/m.s)
ν	Mean velocity (m/s)
ρ	Density (kg/m³)
η	Efficiency (%), effectiveness factor

Subscripts

0	Initial
A	Reactant A
ads	Adsorbed
atm	Atmospheric
cs	Cross-section
α	Intensity dependency power
e	Effective
f	Fluid
m	Monolayer surface coverage
n	Reaction order
p	Particle; Primary
s	Secondary
t	Total
w	Water

Chapter I: Introduction

1.1. Background

Indoor air pollution is among the top five environmental health risks [1]. The exposure to indoor air pollutants can cause adverse health effects to the building occupants. The associated health risk associated to VOCs as the major group of indoor air airborne pollutants with high toxicity in a low concentration level is one of the serious problems for residential and office building occupants. The VOCs can be emitted from numerous sources such as furniture, consumable products, electronic appliances, building materials, etc. Depending on the pollutant sources, the concentration level of variety of VOCs could increase in indoor air. The low flow rate of outdoor air ventilation along with building tightness typically helps to rapid accumulation of airborne pollutants much higher than safe threshold designated for the humans. For this reason, the maximum concentration of VOCs such as some alkane hydrocarbons and aldehydes in the new buildings can be three times higher than in the existing buildings [2]. In Canada, the ambient average concentration of total VOCs was reported as 57.5 ppb for 2010. Figure 1-1 shows the annual average daily VOCs concentration measured in different regions across Canada [3]. Figure 1-2 shows the distribution of VOCs emissions sources in Canada [4]. The reported data in these figures excluded the emissions from natural sources (e.g., forest fires) and open sources (e.g., prescribed burning).

The *NIH Household Product Database* lists the hazardous chemicals that can be found in most household products. This database shows that the emitted VOCs from these articles can produce serious health problems.
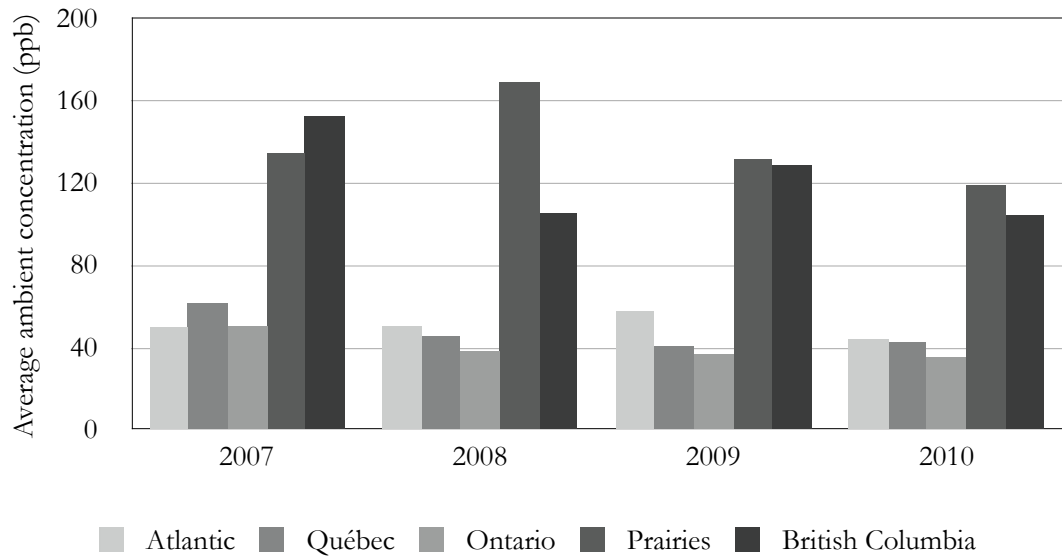
Figure 1-1. Average daily VOCs concentration in outdoor air, Canada (2007-2010)

In the US, *Clean Air Act* (CAA) 1990, included 189 air pollutants as *hazardous air pollutants* (HAPs). In the last decade, the Clean Air Act regulation resulted a reduction of emission rate from the listed compounds from classified sources. The report shows that the indoor air concentrations of some HAPs has decreased because of the reduction of outdoor contaminant levels and technology innovations in building materials and household products such as zero or low VOC paints, solvents, reformulated consumer products and new air cleaners, etc [2].
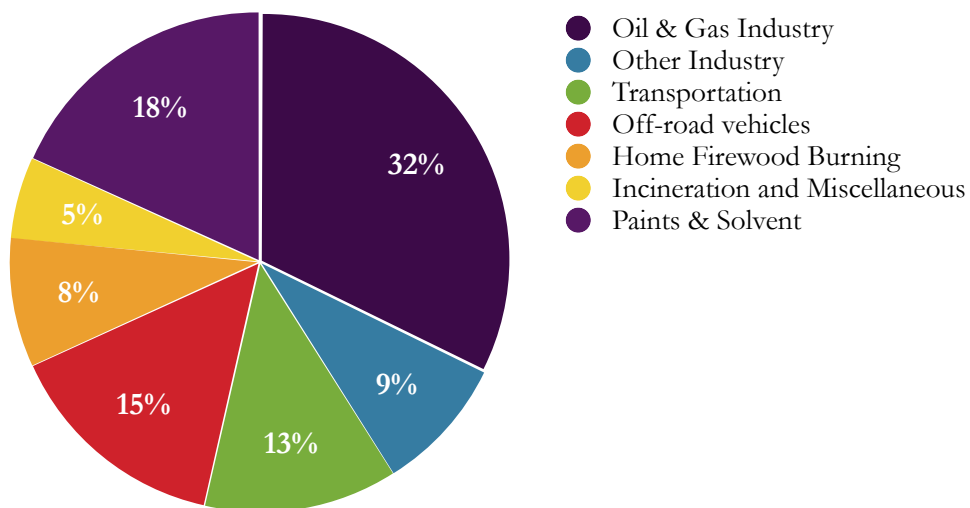
Figure 1-2. Distribution of air pollutant emissions by source, Canada (2010)

Removing pollutant sources or ventilating with outdoor air is the common solution to eliminate the indoor air pollutants. Depending on the building type or poor outdoor air quality, these solutions may not be possible. There are several available air cleaning technologies that can be used to remove gaseous airborne pollutant from indoor air using the adsorption or destruction process technologies. The adsorption process uses a sorbent media that adsorbs the pollutants from passing airstreams. Some of these air cleaning devices can be installed in the central *heating, ventilation and air-conditioning* (HVAC) systems or portable models can be used for specific rooms or limited areas. Figure 1-3 shows available air cleaning technologies for indoor air buildings [1].
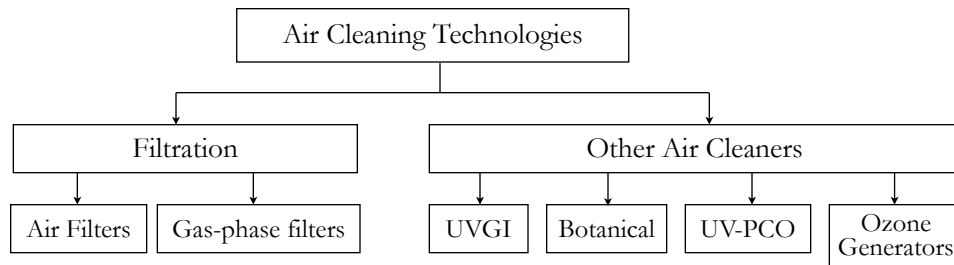
Figure 1-3. Most known technologies for indoor air cleaning systems

The filtration methods are divided into mechanical and gas-phase air filters:

(a) The mechanical filtration can remove airborne particles by capturing them on filter material. The HEPA filters are examples of mechanical filtration method.

(b) The gas-phase air filters use sorbent media or electrostatic charges to remove gaseous pollutants from the air. The sorbent filters are suitable for limited class of pollutants and they cannot remove all the gas-phase pollutants. The performance of gas-phase air filters gradually reduces as they reach to theirs capacity. For high pollutant circumstances, the lifetime of filters would be short and they need to be replaced more often. Electronic air cleaners use electrostatic attraction method to collect charged particles from the air. The charging of particles happens by two methods: ion generators or electrostatic precipitators. The electronic air cleaners can only remove small size particles, but they could not remove VOCs or other gas-phase pollutants from indoor air. Some models may produce ozone that can be introduced into air.

3

The UV-PCO is a novel technique which can remove a wide range of air pollutants. It is considered as a prominent technology for the next generation of air purification systems. This technology has attracted much interests in the last decades. The photocatalysis process involves a series of reactions in the presence of ultraviolet (UV) light and a semiconductor material as catalyst. Titanium dioxide is the most common catalyst material used in the PCO reactors. The exceptional molecular structure of TiO_2 with high surface area contributes to become an excellent candidate for PCO reactions. The detailed study of physical and chemical properties of TiO_2 particles helps to synthesis an efficient catalyst with a better degradation rate of organic compounds. The UV-PCO advantages could briefly be summarized as: the complete oxidation of a wide range of organic compounds to CO_2 and H_2O at ambient temperature. The possibility of using the solar energy to initiate the photo reactions instead of UV lamps is one of the attractive features of this technology, which could make it an ideal air treatment process for indoor air applications with low ppb concentration levels.

1.2. Research Objectives

Two key objectives of this research were the development of a high quality TiO_2 catalyst in order to enhance the PCO reactivity of indoor air applications. The removal efficiency of new PCO systems was investigated with *ultraviolet* (UV) illumination against different individual VOCs at different relative humidities. The performance of the new PCO catalysts was compared with a commercial PCO catalyst under similar test conditions. The other objective of this study was to develop a methodology to correlate the *ionization energy*[1] (IE) of selected compounds as a characteristic of physical and chemical properties with performance of PCO systems. The effect of different test operation parameters such as VOC inlet concentration, irradiation and relative humidity on reaction kinetics and byproducts generation was studied in detail.

---

[1] Also known as *ionization potential* (IP)

Chapter II: Literature Review

2.1. Introduction

Heterogeneous UV-PCO, like other heterogeneous catalytic processes is developed to minimize energy consumption, reduce pollution and increase efficiency for both industrial and nonindustrial applications. Main achievements in this area are probably due to the recent innovation and research in material science and light technologies. In recent years, there has been an increased number of published works in PCO which focused especially on gas-phase heterogeneous photocatalysis [5]. A photocatalytic oxidation system uses a semiconductor material such as TiO_2 as catalyst that works with ultraviolet radiation to convert adsorbed airborne emissions to benign substances such as water and dioxide carbon. The majority of available literature work is based on laboratory experimental research. Throughout these years, researchers could only study a limited number of VOCs among hundreds of known contaminants [6]. Presently, more than 60 volatile organic compounds have been studied exclusively on heterogeneous PCO reactions, namely formaldehyde, ethylene, acetaldehyde, toluene, benzene, xylene, etc [7-10]. Meanwhile, only a few common indoor inorganic compounds like ammonia, hydrogen sulfide, nitrogen oxides and ozone have been studied [11-13]. Most PCO uses nano-titanium dioxide as catalyst due to its relatively cheap price with a highly stable structure with chemically resistant to the reactants and reasonable reaction activity with many VOCs. Titanium dioxide itself is generally considered as a safe chemical and it can be found in toothpastes, paints, sunscreens, etc. It produces less byproducts in comparison to other types of catalysts [14]. Moreover, due to higher stoichiometry ratio of oxygen to VOCs, there is no need to employ excess oxidants like ozone or hydrogen peroxide to have complete reactions. Thus, abundant oxygen in the air is the main oxidant compound in the photocatalytic reactions. The complexity of PCO kinetics with unforeseen byproducts that can be generated from different PCO reactions, could make it very difficult to have an accurate efficiency prediction of PCO systems under various environmental test conditions. All these suggest that the applicability of PCO systems

performance in residential and commercial ventilation systems still is unclear and more research and development in this area is required.

2.2. Reaction Mechanisms

All photocatalytic reactions take place on the surface of catalyst. The PCO process can be divided into seven steps:

1- External diffusion: Transfer of VOC molecule from the fluid phase surrounding the catalyst particle (bulk fluid phase) to the external particle surface
2- Internal diffusion
3- Chemisorption of VOC molecule on an active site
4- Surface reaction of VOC (to CO_2 and H_2O and other byproducts)
5- Desorption of products
6- Internal diffusion: transport of products from the active sites through the pores towards the external surface
7- External diffusion: transfer from external particle surface to the bulk fluid phase.

The mass transfer limitation can be determined by reactor configuration (e.g. flow rate, temperature, catalyst type, porosity and VOCs concentration) where each one of the above mentioned steps can become rate limiting step in the overall reaction rate. Steps 3 to 5 refer to the surface reaction rate. These three steps are the most important steps for a number of reasons: First, the external mass transfer (step 1) usually is not a limiting factor for the mechanical ventilation systems. The contaminants can easily move from bulk gas stream (turbulent flow) and reach to the external catalyst surface. The knowledge of kinetics is essential to optimize a new photocatalytic reactor (size and type of catalyst bed) where the internal diffusion mostly depends on the catalyst characteristics such as pore size and catalyst morphology structure. The efficiency of surface reaction can be a challenging issue for certain VOCs where they have several transitional reactions which may require more time to complete mineralization and this could become a limiting step for overall efficiency of PCO reactions. The kinetics of every reaction depends on the adsorption energy where it is described as activation energy of reaction

that can be found from Arrhenius equation for homogeneous reactions. For heterogeneous reactions the surface coverage could be varied with temperature. The true activation energy at lower temperatures can be changed to apparent activation energy at higher temperature. By considering different PCO reactor configurations, the limiting step for mass transfer can be associated to steps 1, 2 and 6, 7 [15]. There are two types of mass transfer that we should consider: external and internal mass transfer.

2.3.1. External Mass Transfer

The mass transfer rate of reactants from the bulk fluid phase to the external surface of the catalyst can be described by [15]:

$$r = k_f \frac{A_p}{V_p}(C_b - C_s) \qquad (2\text{-}1)$$

Where r is the reaction rate; A_p/V_p is the ratio of outer specific area to volume of catalyst particles; C_b and C_s are the concentration of fluid at bulk and catalyst surface, respectively; k_f is the external mass transfer coefficient and it can directly be estimated by available mass transfer correlations. The value of k_f depends on the virtual liquid film thickness, which could be obtained from available correlations between *Sherwood number* (Sh), which is a function of *Reynolds number* (Re) and *Schmidt number* (Sc).

In the heterogeneous catalysts, the apparent reaction rates may be limited by fluid mass transport to film layer and surface reactions at the same time. In steady state conditions, it is possible to write a general mass balance with the transfer rate of reactants and surface reaction rates by *Langmuir Hinshelwood* (L-H) kinetic model as the following general equation [16]:

$$r = k_f(C_b - C_s) = \frac{kKC_s}{1 + KC_s} \qquad (2\text{-}2)$$

The above equation may be transformed to a dimensionless form as [17]:

$$r = k_f C_b \left(1 - \frac{C_s}{C_b}\right) = \frac{k \, \cancel{KC_b} \left(\frac{C_s}{C_b}\right)}{\cancel{KC_b} \left(\frac{1}{KC_b} + \frac{C_s}{C_b}\right)} \quad \Rightarrow \quad \frac{r}{k} = \frac{\left(1 - \frac{C_s}{C_b}\right)}{\underbrace{\left(\frac{k}{k_f C_b}\right)}_{Da}} = \frac{\left(\frac{C_s}{C_b}\right)}{\left(\underbrace{\frac{1}{KC_b}}_{\beta} + \underbrace{\frac{C_s}{C_b}}_{\bar{C}}\right)}$$

$$\Rightarrow \quad \boxed{\frac{r}{k} = \frac{1 - \bar{C}}{Da} = \frac{\bar{C}}{\beta + \bar{C}}} \qquad\qquad (2-3)$$

Where, Da is defined as *Damköhler number*, which is the ratio of surface reaction rate to the mass transfer rate. It can be used to examine dependency level of a reaction to external diffusion [15, 16]. At low *Reynolds* number, the surface reactions becomes mass transfer dependent and low *Damköhler* number (Da<Sh) represents the dependency of the system to the mass transfer rate, where *Da* number increases with *Sh* number [18].

Alternatively, *Carberry number* (Ca) could be used, which sometimes is more desirable; as it relates the *observed rate of reaction* to the *maximum rate of external mass transfer*[2]. Intrinsic reaction rate is the reaction rate per unit volume of catalyst particle which could occur only if the concentration throughout the particle is the same as the surface. Observed reaction rate is the reaction rate per unit volume of particle. This is an overall value being equal to the reaction rate per particle divided by the volume of the particle [19]. Alternatively, *j-factor* (J_D) was used widely as an alternative to *Sh* number to determine the mass transfer coefficient, with its analogy with heat transfer:

$$J_D = \frac{Sh}{Re \cdot Sc^{1/3}} \qquad\qquad (2-4)$$

In summary, the external mass transfer from bulk fluid and boundary layer diffusions are typically fast enough (with very high *Damköhler* number*)* in typical PCO systems with such high flow rates, where it could be ignored.

2.3.2. Internal Mass Transfer

Internal mass diffusion only can be considered if the catalyst material is porous. The internal mass transfer is represented by the effectiveness factor and is defined as the ratio

---

[2] [95]   J. M. Winterbottom and M. B. King, *Reactor design for chemical engineers*. Cheltenham, U.K.: Stanley Thornes, 1999.

between the actual reaction rate and rate in the absence of internal mass diffusion. Internal diffusion commonly is ignored due to the superficial diffusion to catalyst surface. However, internal diffusion can become significant when reaction rates are high and catalyst layer is thick and porous [15]. In design of PCO reactors, the thickness of the catalyst layer could be reduced to possible thinnest layer to avoid the influence of internal mass transfer on surface reaction kinetics.

Mass transfer coefficient in porous particles generally is described as *effective diffusion*, D_e, which depends on porosity, geometry and shape of the pores. There are several theoretical methods to determine D_e from porosity data, such as *Wilke*, *Burghardt* and *Kato* [20]. All three models have some limitations, and in comparison with experimental measurements, there is usually a variation up to a factor of two. It is common to determine the effective diffusivity by one of the experimental test methods: Wicke-Kallenbach cell, time-lag, sorption-rate, and chromatography experiments [21].

Similar to external mass transfer, it is necessary to know to which degree the system is under influence of internal mass transfer. To do this, it is better first to define the *Thiele Modulus*, Φ, which relates the intrinsic kinetics to the maximum effective rate of internal diffusion. Analogous to *second Damköhler* number[3] (Da^{II}) and *Carberry number* (Ca), there is *Weisz Modulus*, Ψ, which relates observed reaction rates to the internal mass transfer:

$$\text{Thiele Modulus:} \quad \Phi = \frac{V_p}{A_p}\sqrt{\frac{\frac{n+1}{2}k_v C^{n-1}}{D_e}} \qquad (2-5a)$$

$$\text{Weisz Modulus:} \quad \Psi = \left(\frac{V_p}{A_p}\right)^2 \frac{n+1}{2}\frac{r_{observed}}{D_e\, C_{surface}} \qquad (2-5b)$$

The Thiele and Weisz modulus can be related through *effectiveness factor*, η ($\Psi = \eta \cdot \Phi^2$). The value of D_e for the typical catalysts usually is between 0.3 to 0.6 and τ_p value is

---

[3] Second Damköhler number is the ratio of reaction rate to the rate of mass transfer: $Da^{II} = k_s / k_g$

usually between 2 to 8. For unknown cases, the mean average values of $\varepsilon_p = 0.5$ and $\tau_p = 4$ can be used for the calculations [22].

Concurrent to the mass transfer, sufficient light must be illuminated to the surface of catalyst to generate necessary electron-holes for PCO reactions. For photocatalytic reactors, generation of *electrons* (e^-) and *holes* (h^+) are so fast and the number of electrons generally is not a limiting step for photocatalyst reaction rates. Nevertheless, the number of photo-holes for n-type[4] semiconductor catalysts is much less than the electrons in the system. However, the high intensity of UV irradiation could accelerate the formation of electron-holes. At the same time, it also helps to have better light penetration in more surface areas which can affect the electron-hole recombination and the PCO reaction rates would be promoted afterwards [23].

2.3.3. Principle of PCO Reactions

Photocatalytic oxidation is a process, which involves different reaction steps:
Adsorption, electron and hole migration, dehydrogenation, hydrogen transfer, oxidation, pollutant degradation and desorption. Photocatalytic reactions unlike other conventional catalysts use the photonic activation instead of thermal activation method. All reactions happen on the catalyst surface. The photo-electronic exchange prescribes all the PCO steps in the system, which can be described as followings [14]:

1) Absorption of the photons by the catalyst surface;

2) Formation of electron-hole pairs;

3) Electron transfer reactions such as creation of negative charged anions (or ionosorption) of adsorbed oxygen molecules, radical formation, charge neutralization of adsorbate species and surface reactions;

When the catalyst surface is illuminated with high energy photons (*light energy* greater than *band gap energy*, $hv \geq E_G$), adsorbed photons excite the electrons in the catalyst from *valence band* (VB) to *conduction band* (CB). These highly reactive electron-holes

---

[4] '*n-type*' semiconductors have an electron abundance versus '*p-type*' which have an abundance of hole

in VB and CB can migrate to surface and initiate reduction reactions (O_2), which starts oxidation reactions of VOCs.
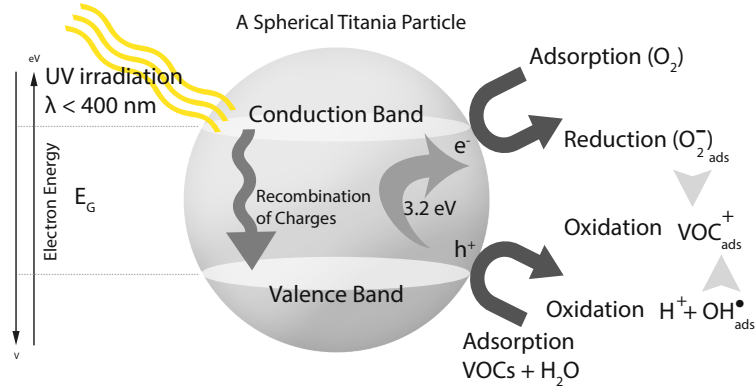
Figure 2-1. Reaction mechanisms of PCO on a catalyst particle (section 2.2, step four)

In presence of humidity, adsorbed water molecules can react with holes and produce hydroxyl radicals, which, in turn it can oxidize VOCs (Figure 2-1). The produced oxygen and hydroxyl radicals are the most important electrophiles and nucleophiles species in a photocatalytic process. The highly reactive hydroxyl radicals may act as traps for the VB holes where they can hinder the recombination of active electron-hole. The following equations describe the possible photoelectronic reactions on the catalyst surface, which include photo generated holes (h_{VB}^+) [24]:

$$hv + \text{TiO}_2 \rightarrow \text{TiO}_2 (h^+ + e^-) \qquad (2-6)$$

$$h^+ + e^- \rightarrow hv' + nc \qquad (2-7)$$

$$h^+ + \text{H}_2\text{O}_{ads} \rightarrow \text{OH}^\bullet_{ads} + \text{H}^+ \qquad (2-8)$$

$$h^+ + \text{OH}^-_{surf} \rightarrow \text{OH}^\bullet_{ads} \qquad (2-9)$$

$$h^+ + \text{VOC} \rightarrow \text{VOC}^+_{ads} \qquad (2-10)$$
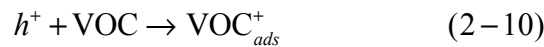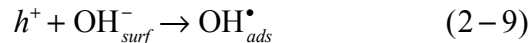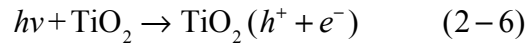
The produced h^+ in the valence band has options to join in different possible reactions. The holes can directly recombine with electrons (Eq. 2-7) or make a reaction with adsorbed oxygens (Eq. 2-12) or water molecules (Eq. 2-8).

The electron transfer to adsorbed oxygen molecules and creation of anionic O_2 species, can lead to reaction with OH$^\bullet$. The superoxides have a similar role as hydroxyl radicals and they can be engaged in the destruction of adsorbed VOCs:

11

$$O_{2\,ads} + e^-_{CB} \rightarrow O^-_{2\,ads} \qquad (2-11)$$

$$O_{2\,ads} + h^+ \rightarrow O_{2\,(g)} \qquad (2-12)$$

$$O^-_{2\,ads} + H^+ \rightarrow HOO\bullet \qquad (2-13)$$

$$O^-_{2\,ads} + \bullet OH \rightarrow HOO\bullet + O^-_{ads} \qquad (2-14)$$

$$2\,HOO\bullet \rightarrow O_2 + H_2O_{2\,ads} \qquad (2-15)$$
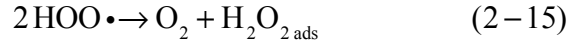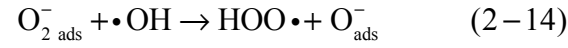
The produced hydroxyl peroxides can react with adsorbed oxygens and available photo electron-holes:

$$H_2O_{2\,ads} + O^-_{2\,ads} \rightarrow \bullet OH + OH^- + O_2 \quad (2-16)$$

$$H_2O_{2\,ads} + e^-_{CB} \rightarrow \bullet OH + OH^- \qquad (2-17)$$

$$H_2O_{2\,ads} + hv \rightarrow 2\bullet OH \qquad (2-18)$$
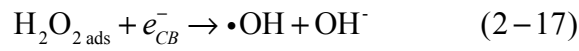
The hydroxyl radicals also are capable of migrating and carrying out direct destruction of absorbed VOCs on the catalyst surface:

$$\bullet OH + VOC_{ads} \rightarrow VOC_{oxd} + H_2O \qquad (2-19)$$

The hydroxyl radicals as described by the above equations are the most reactive species; they are able to nearly oxidize almost all VOC molecules and degrade them to benign products like carbon dioxide and water. There are two explanations for hydroxyl reactions [14]:

a) An indirect oxidation with adsorbed hydroxyl radicals on the surface (Eq. 2-9 to 2-12);

b) A direct oxidation through generated holes (Eq. 2-19);

Accordingly, it is obvious that the mechanism of PCO is based on hydroxyl radical attacks and •OH radicals play an important role in oxidizing the organic compounds. Moreover, some works have shown that there is a direct relationship between reaction rate constant of hydroxyl radical, k_{OH}, and reaction rate constant [25-27].
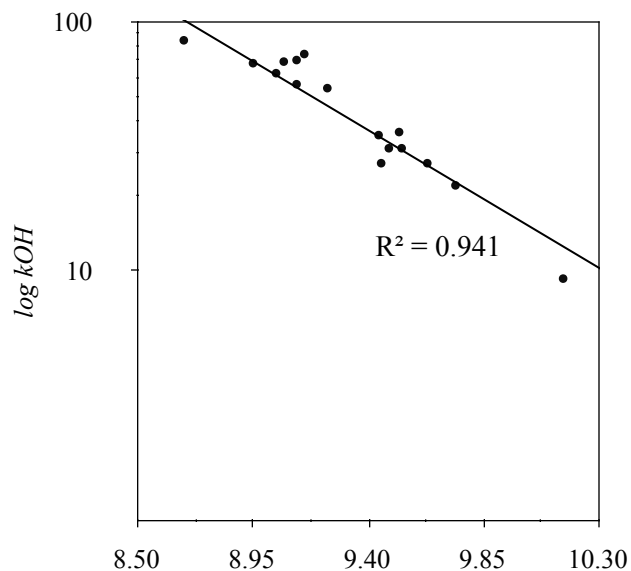
Figure 2-2. Ionization energy versus hydroxyl addition reactions for a selection of alkenes and alkynes. Data obtained from *Gaffney et al.* [25]

Although, there is much information about hydroxyl radical activity and organic compounds, there are also uncertainties about kinetics and mechanism of reactions, that create a gap in creating a comprehensive model. Therefore, it is essential to develop a systematic procedure to identify the kinetics behaviors which allows to predict PCO reaction rates of the VOCs.

A number of methods have been proposed for estimation of gas-phase hydroxyl radicals and reaction rates of VOCs. For example, *Gaffney et al.* used molecular physical properties of the organic compounds, such as *linear free energy*, *bond association energy* and *ionization energy* (IE) to correlate the hydroxyl radicals and reaction rate of reactants together (see Figure 2-2) [25]. They showed that ionization energy as a *structure reactivity relationship* (SRR) could be used for the development of correlations with organic compounds reaction rate. The *IE* also was used to predict the rate constants of OH radical and organic compounds reaction rate [28]. The correlations were extended further based on carbon-hydrogen bond dissociation energy. *Sattler et al.* developed a correlation based on a pseudo-first order L-H mechanism to predict photocatalytic reaction rates by means of physical properties of indoor VOCs [27]. They employed a miniature batch reactor (2.5×30 cm, TiO_2 coated glass plate) with saturated humidity

(>100% RH) and very high level of VOCs concentration (≥10ppm). The reason of such high level of humidity was to minimize the rate limiting effect of water vapor. This model cannot represent the actual indoor air operational conditions, and the experimental system setup was tested under a special laboratory test environment.

Yu el al. also studied the relationship between performance of PCO and physical-chemical properties of VOCs similar to the *Sattler* model [29]. *Yu*'s experiments were carried out under moderate conditions (0.1 to 9.0 ppm for VOCs, RH 20,50, 80%), which can resemble indoor environment conditions [29]. Their PCO kinetic results were completely followed by mono and bimolecular L-H model. They also tried to examine the connection of Langmuir adsorption constants and Henry's law for several VOCs. They found correlations only for similar molecule structures of VOCs. However, they could not find such a correlation between different classes of VOCs.

2.4. Ionization Energy (IE)

The term *ionization energy* (IE) is the minimum energy required to remove an electron from a molecule. The quantity of energy which is required to ionize a molecule was formerly known as *ionization potential* (IP) and it is measured in *electron volts* (eV). Ionization generally occurs when the adsorbed energy of molecule is larger than molecule's energy of ionization. As a result, this process yields a positive ion and a free electron. To ionize VOCs, output energy of UV lamps should be higher than molecules *IE*. As *IE* is a measure of electronic density of a molecule, a higher IE value means that the molecule requires more energy to ionize. It has an inverse connection with rate constants and can be an example of SRR. *IE* has two primary advantages:

It can be measured accurately as molecule characteristics, and it has already been measured for hundreds of organic compounds (Atkinson 1986, Grosjean 1990). Moreover, the experimental IE data for majority of compounds is available from NIST Standard Reference Database[5].

---

[5] NIST Chemistry WebBook: http://webbook.nist.gov/chemistry/

2.5. Kinetic Modeling of PCO

The understating of kinetic reactions is crucial to successfully predict the removal rate of contaminants in the PCO system with involved mechanisms. This generally can be determined by carrying out experiments in a reactor which is operated in single-pass or multi-pass. First, it is necessary to define efficiency percentage (η):

$$\eta\% = \left(1 - \frac{C_A}{C_{A0}}\right) \times 100 \qquad (2-20)$$

where, C_A, C_{A0} are the outlet and inlet concentration of the reactant species, respectively. The power law model generally has been used to describe the PCO reaction rates with an acceptable approximation [30]. Theoretically, power law expressed by the oxidation rate of reactant versus time ($r = -dC_A / dt = kC_A^n$), where k is the rate of oxidation reaction (s^{-1}); C_A is the concentration of adsorbed reactant and n is the order of reaction.

It has been shown that power law equation is applicable for the most ideal PCO reactions [7, 8]. By using separation of variables and integration, it can transform the standard equation to a general form:

$$r = kC^n = -\frac{V}{W}\frac{dC}{dt} \quad \rightarrow \quad \frac{kW}{V}\int_0^t dt = -\int_{C_o}^C \frac{dC}{C^n} = -\int_{C_o}^C C^{-n} dC \quad \rightarrow \quad \int_{C_o}^C C^{-n} dC = -\frac{kW}{V}t \qquad (2-21)$$

$$e.g. \qquad n = 1 \quad \rightarrow \quad C - C_o = -\frac{kW}{V}t \quad \rightarrow \quad C = C_o - \frac{kW}{V}t \qquad (2-22)$$

$$n = \frac{1}{2} \quad \rightarrow \quad C^{1/2} - C_o^{1/2} = -\frac{kW}{2V}t \quad \rightarrow \quad C^{1/2} = C_o^{1/2} - \frac{kW}{2V}t \qquad (2-23)$$

where k is the reaction rate constant; C is the concentration of VOC; n is the order of reaction; V is the volume of the reactor; W is the mass of catalyst and t is the reaction time. The above equations may be solved numerically by the iterative method and an initial guess for the n. To obtain the final equation, the experimental data fitting could be used to find the k value (slope of curve). If the experimental data do not match with rate equation, the selected order value is not a good choice. The calculation could be continued to converge to the best order value for the selected experimental system.

2.5.1. Langmuir-Hinshelwood (L-H)

The *Langmuir-Hinshelwood* (L-H) mechanism has been employed successfully in many PCO research studies. The L-H model consists of adsorption from the gas phase and desorption to the gas phase, separation of species on the surface and reactions between adsorbed species. The kinetic of photocatalysis follows the first order unimolecular L-H model:

$$r = k\theta = \frac{kKC}{1+KC} \qquad (2-24)$$

$$\frac{1}{r} = \left(\frac{1}{kKC} + \frac{1}{k} \right) \qquad (2-25)$$

where reaction rate varies proportionally with the surface coverage, θ. A linear regression analysis of the initial rate ($1/r$) versus the initial concentration of VOC ($1/C_{A0}$) gives the k and K values as the reaction rate constant and Langmuir adsorption constant of the VOC, respectively. However, in the presence of H_2O, the contribution of hydroxyl groups and their competition in adsorption with organic compounds should be considered too. The unimolecular L-H may not be valid in such cases, because it assumes that the reactant effectively reacts with each others; and also other species (e.g. water molecules contribution) were not considered in the model. The L-H expression is only valid with the initial conditions. During the PCO process, intermediates can be formed and their KC terms must be included in the LH equation, even when they have a weak adsorption on the catalyst surface. The L-H model assumed that adsorption and desorption are at equilibrium and surface reactions are not rate limiting. Similarly, the bimolecular L-H assumes above mentioned assumptions, but it includes the water vapor presence along with reactant reactions:

$$r_A = k \frac{K_{A1}C_A}{1 + K_{A1}C_A + K_{W1}C_W} \frac{K_{A2}C_W}{1 + K_{A2}C_A + K_{W2}C_W} \qquad (2-26)$$

where, K_{A1}, K_{A2}, K_{W1} and K_{W2} are the Langmuir equilibrium adsorption constants (ratio of adsorption to desorption rates, $C_{A\ (ads)}/C_A$); C_A and C_W are the concentration of contaminants and water vapor (ppm); first and second terms represent competitive

adsorption between the contaminant and H_2O molecules for an active site [31]. The equation rates which is commonly used for photocatalytic oxidation generally is a different forms of L-H; since the nature of PCO reactions for indoor air conditions always involve a mixture of VOCs and water vapor in the air, it is best to use a mono or bimolecular L-H rate equation, which has been used for indoor air [5].

In general, the TiO_2 catalyst kinetic model follows one of the rate expressions in table 2-1.

Table 2-1. General form of design equations for plug flow PCO reactors (Tompkins, 2005)

Kinetic Model of PCO			Reactor Design Equation	Reaction rate constant, k_A, K_A
Type	*Order*	*Rate Expression*		
	$1/2$	$-r_A = k_A C_A^{1/2} = k_A C_{A0}^{1/2}\sqrt{1-f_A}$	$\sqrt{1-f_A} = -\dfrac{k_A C_{A0}^{1/2}}{2}\cdot\dfrac{W}{F_{A0}}+1$	$k_A = \dfrac{-2\cdot slope}{C_{A0}^{1/2}}$
Power	1	$-r_A = k_A C_A = k_A C_{A0}(1-f_A)$	$\ln(1-f_A)=-k_A C_{A0}\cdot\dfrac{W}{F_{A0}}$	$k_A=\dfrac{-slope}{C_{A0}}$
low	$3/2$	$-r_A = k_A C_A^{3/2} = k_A C_{A0}^{3/2}(1-f_A)^{3/2}$	$\dfrac{1}{\sqrt{1-f_A}}=\dfrac{k_A C_{A0}^{3/2}}{2}\cdot\dfrac{W}{F_{A0}}+1$	$k_A=\dfrac{2\cdot slope}{C_{A0}^{3/2}}$
	2	$-r_A = k_A C_A^2 = k_A C_{A0}^2(1-f_A)^2$	$\dfrac{1}{1-f_A} = k_A C_{A0}^2\cdot\dfrac{W}{F_{A0}}+1$	$k_A = \dfrac{slope}{C_{A0}^2}$
L-H	$-$	$-r_A = \dfrac{k_A K_A C_A}{1+K_A C_A}$	$\dfrac{f_A}{\ln(1-f_A)} = k_A\dfrac{W}{F_{A0}\ln(1-f_A)}+\dfrac{1}{K_A C_{A0}}$	$k_A = slope$ $K_A = (\text{intercept } C_{A0})^{-1}$

Notes: W = mass of catalyst; f_A = fraction conversion; F_A = initial molar flow rate of reactant A entering the reactor

To obtain the Langmuir adsorption isotherm, it is usually assumed that adsorption occurs as monolayer over the surface of catalyst uniformly without any interaction between adsorbates and other molecules.

Alternatively, the validity of L-H model may be confirmed with the experimental data. After integration of eq. 2-22, the following relationship could be resulted:

$$\frac{\ln(C_i / C_o)}{C_i - C_o} = \frac{kKT}{C_i - C_o} - K \qquad (2-27)$$

A linear regression analysis of the $\ln(C_i / C_o)/(C_i - C_o)$ versus $1/C_i - C_o$ can confirm the validity of L-H with PCO surface reactions.

2.6. Hydroxyl Radical (OH)

Since the hydroxyl radicals initiate the oxidation of VOCs, it is necessary to have a good understanding of hydroxyl species and theirs mechanisms. The general principle of OH radicals reactions was described in section 2.3.3. Each organic compound reacts with different kinetics rates and these rates depend on their affinity with the OH radicals. Generally, OH radicals react with VOCs by one of these three mechanisms; *hydrogen abstraction*, *addition to multiple bonds* and *direct electron transfer*. The product of these reactions is an organic radical (e.g. eq. 2-19) which may react with other species and lead to complete degradation.

2.7. Ozone (O₃)

The ozone reaction with VOCs in the gas phase can contribute to their breakdown into smaller molecules as secondary reactions. The ozone molecule itself can be photolysis under UV irradiation [32]:

$$O_3 + hv\,(\lambda \leq 310nm) \rightarrow O_2 + O(^1D) \qquad (2-28)$$
$$O(^1D) + H_2O \rightarrow 2OH \qquad (2-29)$$
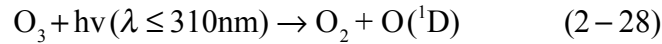
Depending on the ozone concentration, the production of hydroxyl radical may promote the degradation of VOCs with the described equations in section 2.3.3. The overall reaction for the ozone with VOCs can be written as following:

$$O_3 + VOCs \rightarrow Products \qquad (2-30)$$

The rate of ozone consumption in the system is:

$$\frac{-dC_{O_3}}{dt} = k_{O_3} \cdot C_{O_3} \cdot C \qquad (2-31)$$

Thus, the ozone reaction rate (k_{O3}) with VOCs for an ideal plug flow system can be determined by integrating from above equation [32]:

$$k_{O_3} = \frac{\ln\left[C_{O_3 o} - C_{O_3}\right]}{0.5(C_o + C)(\Delta t)} \qquad (2-32)$$

where C_{O_3o}, C_{O_3}, C_o and C are respectively the upstream and downstream concentration of ozone and VOCs; Δt is the reaction time which is defined as reaction time. It can be calculated from the flow rate and reactor length size.

However, the direct reaction of ozone with majority of VOCs happens very slowly under ambient indoor air conditions. For example, the degradation of n-butane with O_3 with concentration of <40ppb at 298 K and reaction rate of $k = 2.0 \times 10^{-23}$ can take more than 30 years. This shows that the VOCs reaction with ozone in the gas-phase is almost negligible. In this study, the produced ozone concentration in the system is much higher than atmospheric level. Therefore, the ozone reactions with water vapor and gas-phase oxygen reactions are the potential gas-phase processes which may affect the oxidation of VOCs. It seems that the produced hydroxy radicals by ozone photolysis are the most important species in the reactions, and the surface catalytic reactions are the dominant reactions in the PCO system.

2.7. Catalyst

2.7.1. Catalyst Material

Most used catalysts in PCO are made of chalcogenide metal oxides compounds, e.g.: titanium dioxide, zinc oxide, zirconium dioxide, tungsten tri-oxide or sulfides such as cadmium sulfide. The activity of these metal oxides can be initiated with a specific band-gap energy photons. The illuminated photons energy must be higher than catalyst band-gap energy. The medium band gap energy of these semiconductor catalysts is 1-3.3eV within their valance and conduction bands. Titanium dioxides, TiO_2, commonly has been used in pure form or doped with other metals (e.g. Pt, Ni) in most photocatalytic reactors. Most catalysts also are available commercially in deposited film of titanium dioxide forms. The crystallography of TiO_2 plays an important role in adsorption and photo degradation activity of gaseous reactants. The most abundant crystalline form of titanium dioxide can be divided to three polymorphs: *anatase* (tetragonal), *rutile* (tetragonal) and *brookite* (orthorhombic). Anatase and rutile are the most photocatalytic active forms of TiO_2.

TiO₂ rutile tetragonal crystal structure   TiO₂ anatase tetragonal crystal structure
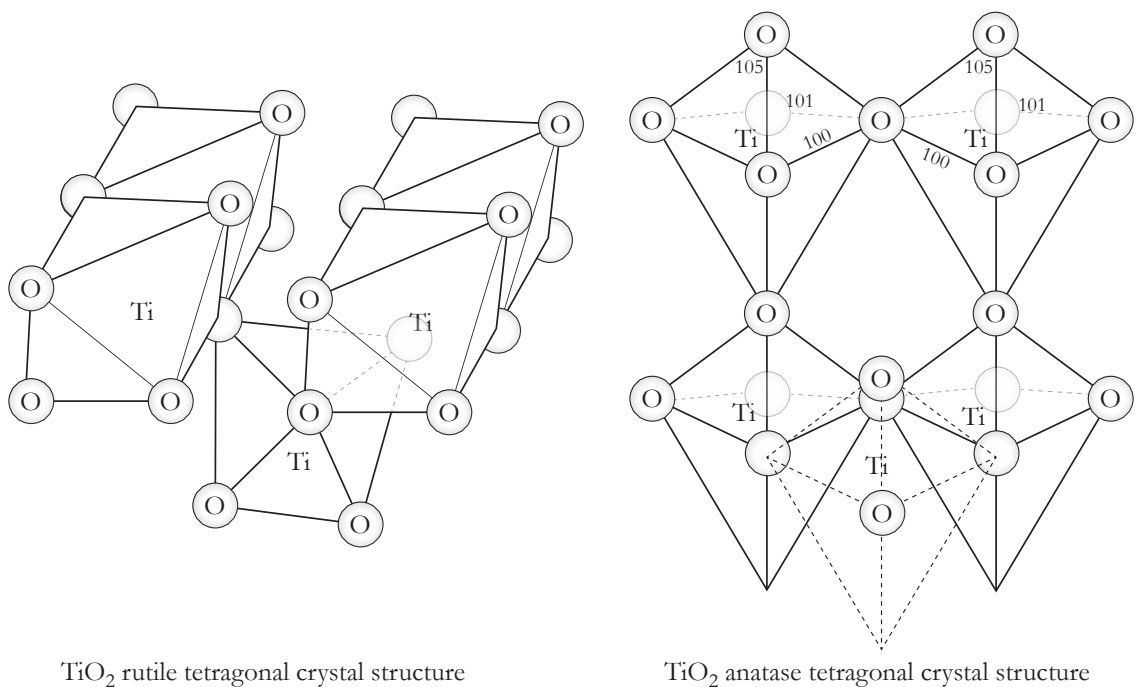
Figure 2-3. Compare rutile and anatase crystal structure of titanium oxide (reproduced from RRUFF™ Project)

Figure 2-3 shows the difference in the structure of anatase and rutile. This figure depicts that the Ti atom surrounded with labeled O (Oxygen) atoms. Among these structures, rutile is the more stable form. Rutile TiO_2 has a tetragonal unit cell with two Ti atoms and four O atoms. The Ti atoms are surrounded with six O atoms where the octahedral structure of O atoms are slightly disoriented to provide space for all the ions. The crystals are staked together with their long axis rotated by 90º which characterized the rutile crystal structure. Anatase TiO_2 has a tetragonal unit cell, where a cell unit contains four TiO_2 atoms. The coordination of Ti and O atoms are the same as rutile, but the octahedral structure of O atoms are more disported compare to rutile structure [33].

In high temperature (>550ºC), more anatase and less brookite phase tend to transform to rutile. However, brookite has a very low conversion rate and low photocatalytic activity [34, 35]. The broader band gap of anatase helps to have higher activity under a wider range of ultraviolet irradiations.

Titanium metal oxide shows low adsorption ability for non-polar substances due to its polar structure. *Bhattacharyya* [36] showed that using titanium dioxide with adsorbents

support can decrease such inhabitation to some extent. However, other properties may contribute to this problem, such as molecular symmetry, high vapor point (low boiling point) and size of molecule (very small molecules) cannot easily adsorb on catalyst surface (e.g. ethylene) [37]. It was found that the reaction rate has a direct and proportional relation with mass of catalyst and total number of active sites [14]:

$$r = k.n_T = k.d.m.S_{BET} \qquad (2-33)$$

Depending on the PCO reactor, above a certain amount of catalyst mass, the reaction rate becomes independent. Extra amount of catalyst can mask the photoactivity of the catalyst surface to some extent. Use an optimal amount of TiO_2 makes possible to have maximum absorption of produced photons and waste reduction of excessive catalyst (Figure 2-4).
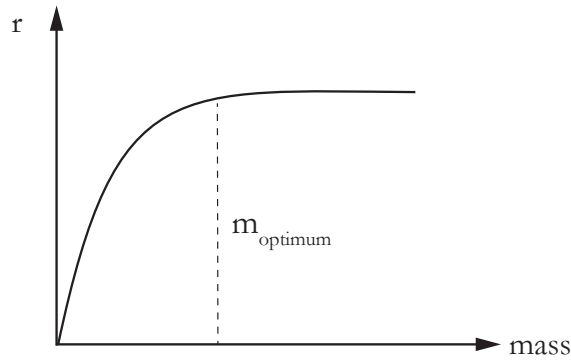
Figure 2-4. Effect of catalyst mass on PCO reaction rate

The catalyst mass depends on several reactor design configuration such as geometry, irradiation intensity, air flow rate and coverage ratio for all particles; moreover, photocatalyst operation conditions such as temperature and contaminant concentration must be considered for each application. The optimal catalyst mass amount should be determined regarding to application of PCO system to avoid excessive catalyst usage and maintain the maximum absorption of illuminated photons [14].

Various designs of PCO reactors are reported in the literature, such as power layer, plate [38], honeycomb [39], annular [40], packed-bed, fluidized-bed, optical fiber, mop fan and combined-adsorption type [41]. However, only a few of these types can be used for indoor air cleaner systems [42].

Theoretically, it is possible to obtain the large convective mass transfer rate and reaction rate for the plate type reactors, but the reaction area is much smaller than other types of reactors. In the honeycomb type reactor, the UV light is parallel to the reaction area, which results in low reaction rate even if reaction area and mass transfer are large. For the annular type reactor, the convective mass transfer rate and reaction area are small, even when the UV light irradiates on the reaction area directly. Ideally, the structure of a PCO reactor should have high specific surface area for a better reaction, support small passthrough channels with low air velocity for a higher residence time and have the UV light irradiate directly on the reaction surface. Normally, the structure of a PCO reactor consists of two key parts: the catalyst structure and the UV light source. The catalyst type is an important PCO design element which could improve the adsorption rate and overall PCO kinetic reactions of system.

2.7.2. Catalyst Support

The titanium dioxide can be deposited on a different type of supports. The support material can be: activated carbon, glass [41, 43, 44], silica [10], ceramic, metal and polymer [45]. The adsorption, stability and surface area of catalyst and the photocatalytic activity of the deposited TiO_2 particles can be improved significantly by selecting a suitable substrate material type. Therefore, a suitable type of substrate can extend the overall catalyst lifetime and it can also improve the partial oxidation reactions and desorption of end products.

2.7.3. Catalyst Lifetime, Degradation

The broad range of irresistible catalyst deactivation is generally related to high temperature operations, which leads to partial or complete catalyst deactivation. The catalyst deactivation at ambient air temperature generally is a reversible phenomena, which starts by decreasing the number active catalyst sites on the catalyst surface. There are several reasons that may lead to this loss: *a*) creation of reaction residues (intermediates) which are strongly adsorbed on the catalyst surface, this usually occurs for acidic intermediates (e.g. trichloroethylene, trichloropropene); *b*) some contaminants

like benzene, photo-polymerize on the catalyst, this happens more in absence of water; *c*) some inorganic contaminants (e.g. nitrogen and sulfur) may undergo a complete oxidation on the catalyst surface and block the active sites of catalyst; *d*) fouling by suspended particles (e.g. soot, dust) may fall on catalyst and block it pores [46]. Several works derived a relationship for deactivation based on reaction rate constants and length of operation [7, 47].

There are several treatments for regeneration of degraded catalysts, which can be used individually or in combination with catalyst regeneration. They are: exposing the catalyst to high flowing air under UV light, treating with H_2O_2 vapor or chlorine radical systems, heating the surface of catalyst, ozone purging with high humidity ratio. Many of these treatment work could recover the catalysts activity, but after every treatment, there is a decrease in overall performance of catalyst. Sometimes, some deactivated catalysts do not respond to any of the above mentioned treatments, due to unknown matters and therefore the whole catalyst must be changed [47].

2.8. Light Source

The reactivity of a PCO depends on the amount of irradiance from a light source with greater band-gap energy of the catalyst. The amount of irradiance is defined as radiant flux, Φ, which determines the number of generated electrons-holes on the catalyst. It should be noted, the number of produced electrons is much higher than photo-induced holes for n-type semiconductors catalysts such as TiO_2 [14].

In a moderate radiant flux, the reaction rate is equivalent to Φ, which is mainly controlled by the number of available holes as the limiting active species. In higher radiant flux, this ratio of electron-holes formation becomes higher than the reaction rates, where the photocatalytic rate becomes proportional to $\Phi^{1/2}$ [14].

Titanium dioxide has a band-gap of 3 to 3.23 eV, which is equal to short wavelength band or at least equivalent to UVA wavelength (according to *Planck'*s equation). The effective wavelength range usually is less than 400nm, which falls to the ultraviolet region of electromagnetic spectrum. There is a direct relationship between illumination type and

irritation intensity on the conversion efficiency of photocatalyst reactions. There are several types of lamps that are commonly used in the experiments: UV lamps (fluorescent, black-light, black-light blue and germicidal) which are divided into three subcategory under UV spectrum: UVC, UVB and UVA. Table 2-2 describes the detailed classification of irradiance in the UV range.

Table 2-2. Definition of UV irradiances (ISO 21348:2007)

Spectral Category	Wavelength range (nm)	Energy per photon (eV)
UV	$100 \leq \lambda \leq 400$	3.1 - 12.4
VUV	$10 \leq \lambda \leq 200$	6.2 - 124
UVC (Germicidal)	$100 \leq \lambda \leq 280$	4.43 - 12.4
UVB	$280 \leq \lambda \leq 315$	3.94 - 4.43
UVA (Black light)	$315 \leq \lambda \leq 400$	3.1 - 3.94

As mentioned earlier, the performance of PCO reactions strongly depends on the light irritation level at the surface of photocatalyst. Moreover, the irritation intensity of a UV lamp decreases over the time. After a continuous usage period, fluorescent lamps (hot cathode or cold cathode), tungsten filaments gradually start to thinning at the ends, and after a long time, it leads to a complete decay [48]. In cases of low UV intensity, it is not possible to employ the whole efficiency of catalyst's surface. In such scenario, it is believed that a large fraction of photons could not create enough electron-hole pairs in the catalyst or many of electron-hole pairs recombine before participating in any reaction and this could eventually lead to a significant reduction of reaction rate in the reactor. Therefore, there should be an uniform distribution of UV intensity on the catalyst surface [49].

The amount of irradiation and its efficient use, is one of the challenges for a high performance and economical PCO device. Many studies suggest that light-rich reactors are more efficient than the catalyst-rich ones [48]. Selecting a proper ratio number of light sources to catalyst mass is the key to reach to an optimal design. The challenge should be emphasized on the design of a reactor with low air flow pressure drop and uniform and sufficient light illumination. Thus, it should look for innovative ideas for getting light into catalyst properly.

Singh et al. investigated the effect of design parameters for cylindrical UV lamps (geometry aspect ratio of catalyst, reflectivity and number of UV lamps) in monolith reactors [50]. They developed a correlation based on photon absorption efficiency, uniformity of radiation distribution and overall photon efficiency to find optimal design parameters for an individual PCO system [50]. They have shown that photon efficiency of monoliths strongly depends on the catalyst reflectivity.

2.8.1. Light Intensity

It has been shown that in photocatalytic reactions, the rate of reaction is proportional to light intensity, I, as I^α with $\alpha = 1$ when the light irradiance is very low, and in high level of intensity, when recombination of electron and holes becomes dominant process, and amount of α would decrease to one half of its value [8]. Therefore, relationship between reaction rate and its dependency on light irradiance can be generally expressed as:

$$k = k_0 \left(\frac{I}{I_0} \right)^\alpha \qquad (2-34)$$

where k_0 is the explicit reaction rate constant, which is unrelated to light intensity; and the value of α, intensity dependency power, is between 0.5 to 1, which can be estimated experimentally [14, 37]. One can also incorporate the above relationship into first order L-H rate equation as following:

$$r = \frac{k_0 KC}{1 + KC} \left(\frac{I}{I_0} \right)^\alpha \qquad (2-35)$$

2.9. Temperature

Since the activation of PCO is photonic, the PCO system can operate at ambient room temperature. On the contrary, according to the *Arrhenius* equation, increasing temperature somehow can promote the reaction rate. Thus, the temperature increase could promote the reaction rate too, but it decreases the adsorption and activation energy (E_a). Similarly, the PCO reactivity decreases at higher temperatures (≥ 70-80ºC) for the majority of PCO reactions. These behaviors can be explained simply by L-H model: The decrease in

temperature helps adsorption phenomena (an exothermic process), and coverage θ approaches to unity, where KC becomes $\gg 1$ [14]:

$$r = k.\underset{\theta \to 1}{\theta} \ \Rightarrow \ \cancel{k} = \cancel{k}\frac{KC}{1+KC} \ \Rightarrow 1+KC = KC \Rightarrow KC \gg 1 \quad (2-36)$$

Moreover, there is desorption process (an endothermic process), where an increase in temperature favors for desorption of the products. This is beneficial especially when desorption process is a rate limiting factor. In contrast, by lowering temperature we have a better adsorption (lower reaction rate and desorption) and generated products would have higher tendency to adsorb and they can become a reaction inhabitant [14].

2.10. Humidity

Water vapor is one of the most important compounds in the photo-oxidation reactions. During the PCO process, water molecules supply hydroxyl radicals and they are also adsorbed on the TiO_2 as molecular state. The adsorbed water molecules are dissociated by transferring their protons to neighbor O species on the TiO_2 surface. This process leads to creation of hydroxyl species where it is affected by numerous factors such as thickness of TiO_2 film [51]. Moreover, the bridged hydroxyl groups can react with adsorbed O_2 where it produces H_2O_2 species. This adsorbed hydrogen peroxide molecules instantly transform into HO_2-TiO_2 by donating a proton to bridging oxygen. These hydroxyl radicals may further participate in different other reactions and they could promote the overall photocatalytic oxidation process [51]. The water vapor effect in complete oxidation of different VOCs depends on the reactants molecules type too [31, 37].

The water vapor molecules can also physically be adsorbed on the adsorbed hydroxyl groups by hydrogen binding. Many VOCs such as toluene, formaldehyde, p-xylene, 1,3-butadiene and many others with similar chemical structures are expected to be adsorbed similarly on the surface hydroxyls thru OH··π electron type interaction [31]. In this case, the relative bonding energy plays an important role in competition behavior with water vapor over active sites. Previous studies showed that too much humidity may inhibit the VOCs destruction rates by competing with the VOCs molecules for available active sites

[8, 30]. It seems that a relative humidity of 40-50% is an optimal range for many VOCs and higher than this specific amount can inhibit the efficiency of PCO reactions.
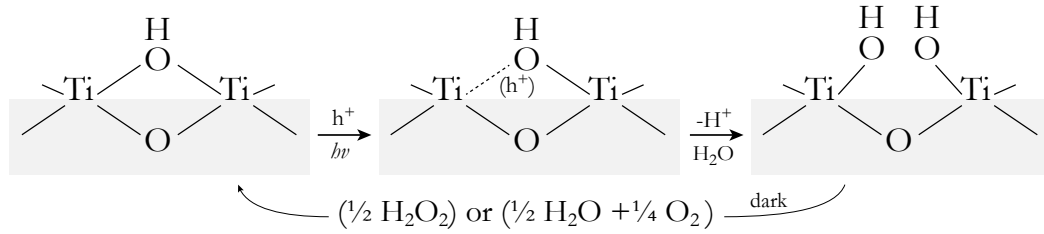
Figure 2-5. OH group formation with bonding to oxygen vacancy on TiO_2 (reproduced from Ref. [52])

The UV light irradiation creates the lattice oxygen vacancies on the catalyst surface. The water vapor attached to these new oxygen vacancies could lead to the formation of hydroxyl groups on the TiO_2 surface. The UV irradiation also intensifies the number of photo generated holes and afterwards these holes could help to the reconstruction of more hydroxyl groups at oxygen defect sites. The reconstruction process of surface hydroxyl is described in figure 2-5 [52]. The majority of photocatalytic characteristics of TiO_2 could be explained with its defect disorder. The oxygen defect sites are one of the most important structure defects that help to have better surface adsorption, and improve charge transport and overall photocatalytic performance of TiO_2 catalyst [53].

In conclusion, the electronic structure of TiO_2 plays an important role in adsorption of water and oxygen molecules on oxygen vacancies. With an increase of OH surface coverage, the diffusion of H_2O and O_2 molecules are enhanced through the oxygen bridges through the TiO_2 structure [51].

2.11. Air Flow

Air flow rate is considered as an important parameter on mass transfer process in terms of concentration gradient and velocity rate; In the laminar flow, the boundary layer, mass transfer coefficients and diffusion may become limiting step for kinetics of surface reactions. It is well known that the quality of surface reactions depends on the diffusion mass transfer from bulk to catalyst surface. At low flow rates, the adsorption rate of VOCs can be increased to a level where the flow rate is not longer a rate limiting step for

the PCO reactions. However, raising the flow rate to further could lead to decrease of reactants PCO rate.

Air flow rate is an important factor in a reactor design because it can change the reaction rate and length of time the contaminants needed to remain through reactor to be completely oxidized to final products. As the air flow rate usually cannot be adjusted too much in HVAC systems, the volume of reactor may be used as a PCO design element to determine the desired residence time. In other words, longer residence time and larger reactor size mean, higher reaction rates. Thus, we need to calculate the reaction rate of desired VOCs to determine the size of reactor.

Residence time is the period that VOCs molecules are within boundaries of the photocatalyst and can be absorbed on the surface of catalyst. Different reactor design and catalyst type affect the residence time. However, the residence time of a particular reactor with fixed flow rate should be constant. Therefore, the only variable parameter in this equation is the flow rate which has a reverse relation with the residence time. Residence time can be defines as:

$$\tau = \frac{A.L}{G} \qquad (2-37)$$

where A is the cross section of catalyst (m^2); L is the depth of catalyst (m) and G is the flow rate (m^3/s or cfm). Above equation can be written in this form: $\tau = V/G$ where V is the volume of the reactor. In distinctive conditions, the residence time can be interpreted as *space time*, where it defines as the required time to process one reactor fluid volume based on entrance conditions. At certain conditions, they could become equivalent: constant density, isothermal and isobaric operation. However, since all of these conditions in indoor ventilation systems may not be valid, they cannot be considered as two equivalent definitions.

In building HVAC systems, the PCO systems cannot be treated as an ideal reactor. In real reactors, non-ideal flow patterns, catalyst types and process conditions result in ineffective adsorption and lower reaction conversions than in the ideal reactors.

Quici et al. studied the effect of different flow rate and residence time on toluene degradation in low concentrations (10-500 ppbv) [54]. The result of their experiments is shown in Figure 2-6. As can be seen from Figure 2-6, the flow rate changed from 0.125 to 4 [lit/min] and residence time from 120 to 1920 ms.

The removal efficiency of toluene for this range of flow rate was not 100% (about 90% in optimal experimental conditions). This behavior could be related to low coverage of catalyst surface and a first-order in conversion of toluene. They observed that there was a significant reaction for toluene without TiO_2 catalyst under dry air [46]. This could be attributed to gas-phase reactions with active oxygen which are created by UV irradiation or even to direct photolysis of toluene [55].
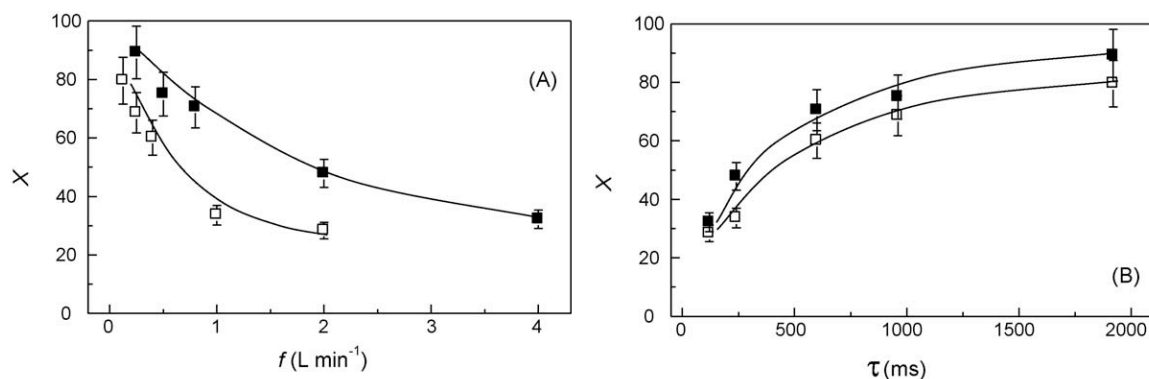
Figure 2-6. Toluene removal (X) for two different reactor lengths L = 5 cm (white squares) and L = 10 cm (black squares), as a function of: (A) flow rate, f; (B) residence time, t. (reproduced from *Quici et al.* [54])

2.13. Volatile Organic Compounds (VOC)

The definition of VOCs for the first time is suggested by WHO [6]. VOC represents a major group of organic chemical compounds with boiling points that vary between 50-250ºC at a standard atmospheric pressure of 101.3 kPa. The boiling point shows that they can be vaporized in different ratio and are released into the air at the normal temperature. VOCs exist in many household products and building materials. They can be released from everyday products and materials into atmosphere. The main concern about indoor air VOCs is the harmful effect of VOCs on the people health. The VOCs are commonly categorized into three groups based on their boiling point (Table 2-3).

Table 2-3. Classification of organic compounds (adopted from WHO [6])

Description	Abbreviation	B.P. (°C)	Example Compounds
Very volatile (gaseous) organic compounds	VVOC	<0 to 50-100	Propane, butane
Volatile organic compounds	VOC	50-100 to 240-260	Formaldehyde, toluene, acetone, ethanol, 2-propanol
Semi volatile organic compounds	SVOC	240-260 to 380-400	Pesticides (DDT, chlordane, plasticizers), fire retardants (PCBs)

US *Environmental Protection Agency* (EPA) defines VOCs as any carbon compound (excluding carbon monoxide, carbon dioxide, carbonic acid, metallic carbides or carbonates, and ammonium carbonate) which participate in atmospheric photochemical reactions [56]. The *Committee for Health related Evaluation of Building Products* (AgBB), defined volatile organic compounds within range of C_6 to C_{16} as individual substances for *total-volatile compounds* (TVOC) and in range of C_{16} to C_{22} as *semi-volatile compounds* (SVOC) [57]. Indoor air defines as the air in non-industrial enclosure areas like residential, office, hospital and public buildings. VOCs may be released from numerous sources, e.g. building materials, consumer products, furniture and personal activities, combustion emission from cooking, biological sources such as plants and molds [58].

Many VOCs are toxic and they can cause many diseases like *sick building syndrome* (SBS) or other respiratory health effects in long term exposure. Availability and concentration of VOCs differ based on the type of building and age of building. Mean concentration of individual VOCs generally is less than 50 μg/m^3 and mostly below 5 μg/m^3 [59]. However, concentration levels in new buildings could be much higher, which commonly arises from new building construction material. The ratio of indoor to outdoor concentrations can be used to categorize most important VOCs in indoor environments. For most of the VOCs, mean concentration in residential were greater (by a factor of two or more) than those in public buildings [59, 60].

Several studies observed a remarkable variation of VOC concentration in different seasons. For example, in summer, concentration of formaldehyde increased from 100 to

above 400 μg/m^3 and TVOCs concentration increased during the autumn season (this can be related to the temperature and natural air ventilation rate changes). This shows that levels of contaminants are generally unpredictable and air cleaners should be able to handle a large range of VOCs concentration [58].

2.13.1. Alkanes

Alkanes are the most common organic compounds that can be found easily in urban and indoor air atmospheres. The *liquefied petroleum gas* (LPG), fossil fuels, and solvent can be considered as the main sources of alkanes. The light alkanes with low vapor pressure mostly are emitted from the building materials as the main source of contamination. The low reactivity of alkanes can be considered as the major problem for the PCO reactions in compare to other class of VOCs.

The reactions of alkanes with hydroxyl radicals were considered as a hydrogen-atom abstraction reaction that forms alkyl radicals and H_2O. The strength of C–H strongly depends on the hydrogen order (primary, secondary or tertiary); C–H band dissociation energy of each one estimated around 98, 94 and 92, respectively. Since these bonds are expected to break during the reaction, we should have fastest reaction for the weaker bonds (tertiary C–H bond), and the slowest for the primary C–H bond. By this way, it is possible to propose an expression as the summation of rate constants for primary, secondary and tertiary C–H bond value:

$$k = n_p k_p + n_s k_s + n_t k_t \qquad (2-38)$$

where k is the overall rate constant for the hydroxyl and alkane reaction; k_p, k_s and k_t are the corresponding rate constants for C–H bonds; n is the number of each C–H bond in a compound molecule. At the ambient air temperature, the kinetic data of alkanes has been suggested as [61]: $k_p = 6.5 \times 10^{-14}$, $k_s = 0.58 \times 10^{-14}$ and $k_t = 0.021 \times 10^{-14}$ [cm^3.mol^{-1} .s^{-1}]. With increasing kinetic values, it shows an inclination toward lower C–H bond energies.

It was found that the low photo activity of light alkanes (C$_5$-C$_{10}$) was similar to each other. The high IP of alkanes made them low reactive compounds in the PCO reactions.

Djeghri et al. (1974) showed that the longer chained alkanes have higher photo reactivity, which directly could be associated to the type of carbon atoms: $C_{tertiary} > C_{quaternary} > C_{secondary} > C_{primary}$. As the reaction pathways influence the oxidation rate of each VOC compound, and it also could determine the type of intermediates and the adsorption competition of main and intermediary compounds. Generally, it was expected that alkanes primarily were degraded into ketones and other aldehydes. *Twesme* (2006) studied the performance of PCO reactions in different temperatures. It was observed that the reactivity of surface reactions could be improved with increasing the temperature from ambient room temperature up to 70ºC, but the higher temperature did not have any significant effect and it had inverse effect on the performance of PCO reactions. Meanwhile, the humidity could change the rate of secondary reaction products and improve the overall photocatalytic activity of alkanes. At low relative humidity level (<30%), the degradation of alkanes were dropped swiftly. It was believed that an adequate humidity is required to create a monolayer of water vapor molecules and it could improve the adsorption of reactants on the bulk TiO_2 surface (*Obee et al.* 1998). Moreover, water vapor could be a source of OH radicals in the system which could promote the surface reactions.

Table 2-4 shows the absolute and relative rate constant of VOCs with OH radical at the ambient room temperature. The absolute relative rate constant can be calculated by temperature rate expressions such as Arrhenius expression ($k = A.e^{-B/T}$) and a three parameter equation has been used for measured rate constant over a temperature range ($k = A.T^n.e^{-B/T}$). The rate constant could be obtained experimentally using different techniques, such as *flash photolysis technique with Resonance Fluorescence detector* (PF-RF) and *relative rate* (RR). The relative rate method uses the experimental data of a reference compound to re-evaluate the rate constants of selected compound [62].

Table 2-4. Rate constants of VOCs with OH radical at indoor air temperature

Class	Compound Name	k ($\times 10^{12}$) [$cm^3.mol^{-1}.s^{-1}$][*]	Relative rate constant, k (27°C)[*]		Absolute rate constant, k[$] [$cm^3\ mol^{-1}\ s^{-1}$]	Temp. Range T (K)
			Behnke et al.	Atkinson et al.		
Alkanes	n-Pentane	3.80	1.63±0.04	1.60±0.04	$2.52\times10^{-17}.T^2.e^{(158\pm40)/T}$	220-760
	n-Hexane	5.20	2.24±0.04	2.21±0.04	$2.29\times10^{-11}.T^2.e^{(422\pm52)/T}$	292-390
	n-Heptane	6.76	2.88±0.06	2.83±0.07	$1.95\times10^{-17}.T^2.e^{406/T}$	290-1090
	n-Octane	8.11	3.46±0.06	3.49±0.07	$2.72\times10^{-17}.T^2.e^{361/T}$	290-1080
	n-Nonane	9.70	4.06±0.11	4.13±0.13	$2.53\times10^{-17}.T^2.e^{(436\pm34)/T}$	290-1100
	n-Decane	11.0	4.88±0.11	4.42±0.22	$3.17\times10^{-17}.T^2.e^{(406\pm56)/T}$	290-1110
Alcohols	Ethanol	3.2			$6.1\times10^{-18}.T^2.e^{-530/T}$	227-599
	1-propanol	5.8			$4.6\times10^{-12}.T^2.e^{-70/T}$	263-372
	2-propanol	5.1			$4.03\times10^{-18}.T^2.e^{-792/T}$	253-587
	1-butanol	8.5			$5.3\times10^{-12}.T^2.e^{-140/T}$	263-372
	2-butanol	8.7				
	1-pentanol	11				

[*]Behnke et. al. (1988); Atkinson et. al. (1982a, b); Atkinson et. al., Chemical Reviews, 2003, Vol. 103, No. 12.
[$]Atkinson, Atmos. Chem. Phys. Discuss., 3, 4183–4358, 2003. | The estimated absolute rate constant uncertainty at 298 K is ~20%.

Chapter III: UV-PCO Experimental Setup and Methodology

3.1. Introduction

As it was discussed in the previous chapter, the main objective of this research was to study the behavior of different classes of VOCs and evaluate the performance of PCO systems in building air conditioning systems. This objective could only be achieved by applying a full-scale experimental setup. On the other hand, there was a need to develop a systematic approach to evaluate the selected chemicals as representative of most important VOCs among the hundreds of identified VOCs, which was identified in the commercial and residential buildings. The wide range of VOCs group could result a complication in the test procedure and assessing the removal efficiency of the PCO system as an acceptable air cleaner device in the building mechanical ventilation systems.

To develop an experimental method for quantitative measurement of VOCs and to compare the removal efficiency of different PCO systems, the experiments were carried out with a special pilot scale system setup in a typical laboratory condition that reassembles to its application in a building. The experimental system setup was composed of four parallel ducts to provide a similar environmental test condition for each individual duct. All ducts had same identical layout; this feature allowed to compare the individual PCO reactors in each duct separately at the same conditions. Moreover, an accurate chemical generation system was used to generate the chemical compounds with very low concentrations. The details of this experiment setup and the generation system detail are explained in the following sections.

A standard experimental procedure was developed to test the different PCO systems with the selected VOC compounds. The setup was specially configured to continuously measure all operational variables such as air flow rate, temperature, relative humidity, UV irradiation throughout the experimental period for each separate duct channel. The collected data were used to accurately evaluate the performance of different PCO reactors in each duct in the course of each experiment. The collected data was used to estimate the kinetic parameter of the tested PCO catalyst.
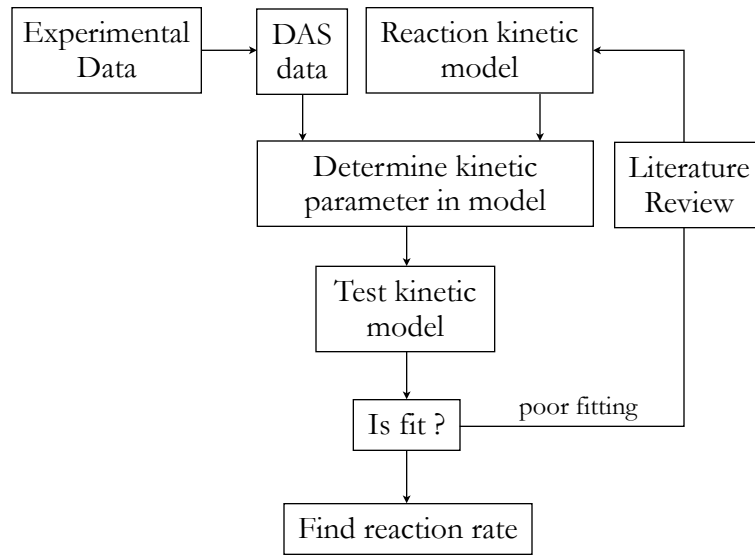
Figure 3-1. Model development procedure diagram for the experimental system setup

3.2. PCO System

3.2.1 Experimental Setup

This section explains the experimental apparatus structure; this section describes the test rig system, sampling and measurement procedure and VOCs sample analysis methods with *automated thermal desorber* (ATD) with *gas chromatography* (GC) and *high-performance liquid chromatography* (HPLC).

A secondary sampling system with *photoacoustic multi-gas monitor* (known as INNOVA) was used to continuously sample and analyze the concentration of TVOC, formaldehyde, CO_2, CO and H_2O during the experiment period. The specification of INNOVA analyzer and system calibration procedure is described in the following sections and Appendix A3.3.

The system has four channels with 0.9 m^2 [1×1 ft.] cross section area and a smooth interior finish to minimize the absorption of VOCs and reduce the deposition of dust particles on interior surface. The system setup was made of aluminum metal as four parallel ducts with a centralized upstream injection system. The system could provide up to 4.25 m^3/min [150 ft^3/m] air flow rate in each duct with a radial fan that is mounted at

the end of each duct. In this study, the air velocity for each duct was set to 100 cfm, which could simulate a similar condition to the real air flow rate in the mechanical HVAC systems. As this pilot system setup was an open-loop system, the condition of the upstream air was completely dependent on indoor lab air conditions (e.g. humidity and temperature). The relative humidity and temperature were not controlled during the experiment period. The flow rate, humidity and temperature sensors (F, H, T) were installed inside each channel for continues measurement. The air flow rate was measured by electronic low flow measurement sensors with 12 [in.] probe size (ELF-1200) that was factory calibrated for flow rates of 0-2.54 m/s (0-500 ft/min) with ±0.25% repeatability. The flow meter probe type was bead-in-glass with high measurement accuracy with *thermal dispersion* (TD) technology.

The power requirement was 24 VAC with maximum consumption of 5 VA. The humidity and temperature sensors (Vaisala, HMT100 series) were able to measure a complete range of air relative humidity (0-100%) and temperature (-40 to +80ºC). Humidity and temperature sensor types were '*Vaisala HUMICAP 180*' and '*Pt1000 IEC 751 1/3 class B*' respectively. The repeatability of the temperature and humidity sensors was ±0.2ºC (@ 20ºC) and ±1.7% (@ 15−25ºC), respectively. The power consumption was 24 VAC. Air flow probes were mounted at the upstream and humidity and temperature probes were installed at the downstream of each duct. All sensors were connected to a *data acquisition system* (DAS) (*Agilent 34970A Data Acquisition*/Switch Unit) and the transmitted data were monitored for all channels by *Agilent VEE Pro* software (Figure 3-2).
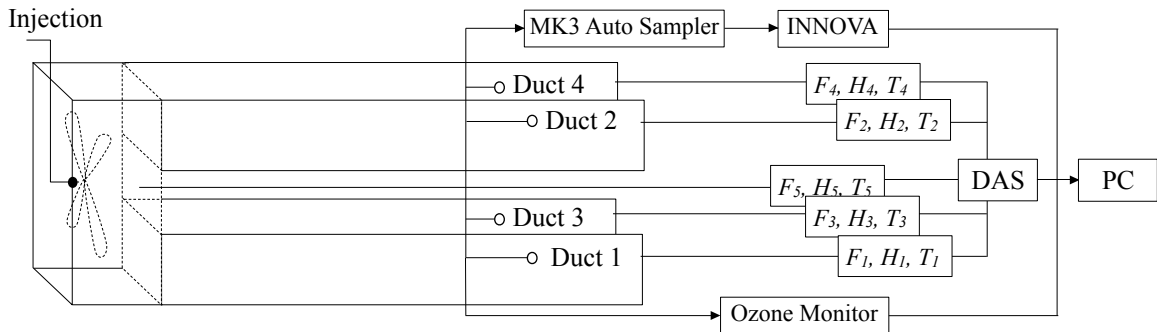
Figure 3-2. Schematic diagram of the data acquisition system

Since the outlet of system was directly connected to the indoor air lab, an adsorbent bed of granular activated-carbon with alumina was installed at the downstream of each duct to remove all the exhaust contamination from the downstream air. Moreover, an ozone scrubber panel was mounted at the end of each duct to capture the produced ozone through the system by the ozone producing UV lamps.

The reactor consisted of different PCO media with several banks of UV lamps arranged in different configurations between the filter media to provide the necessary illumination. The irradiance of UV lamps was monitored continuously with a small radiometer which was installed near the UV lamps. Chemical compounds were injected as a pure vaporized by an appropriate injection system. The vaporized chemicals were transferred with laboratory compressed air as carrier gas to injection port by the PTFE tubing.

The lab air directly passed through a pleated pre-filter before entering to system. The installation of a pre-filter at the upstream was required to remove any possible particulates and dusts from lab air into the system. The details of the system setup are shown in Figures 3-3, 3-4 and 3-5.
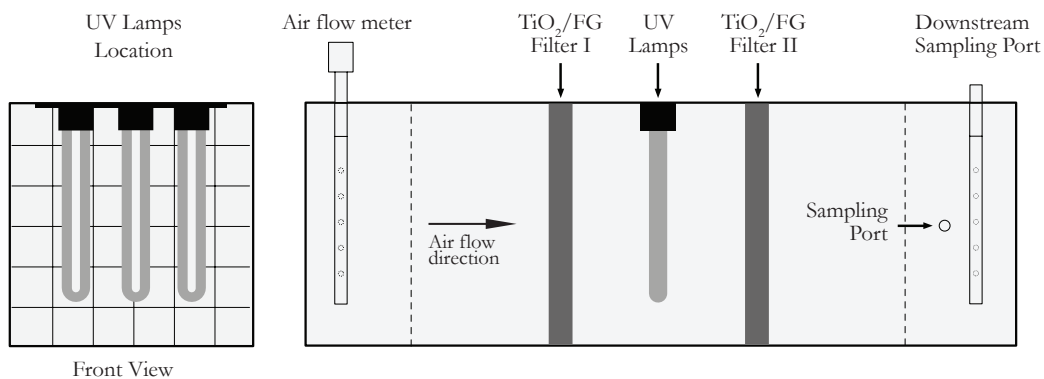
Figure 3-3. Schematic diagram of the reactor (right) and UV lamps location inside the duct (left)
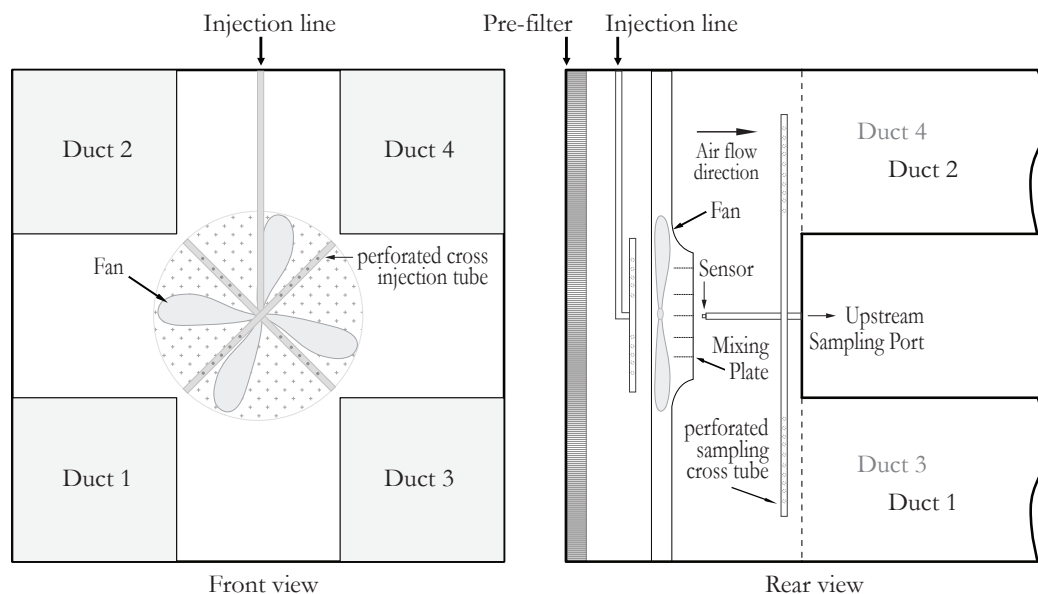
Figure 3-4. Schematic diagram of upstream section and injection port location

The concentration of test compound was selected at different ranges from low ppb to ppm level which could efficiently challenge the performance of TiO$_2$ PCO filters in the worst case scenario. A high inlet concentration could challenge the PCO catalyst much faster where the reactant rapidly adsorbs on the catalyst surface and engages all active sites with reactants and possible intermediate compounds during the experiment period.
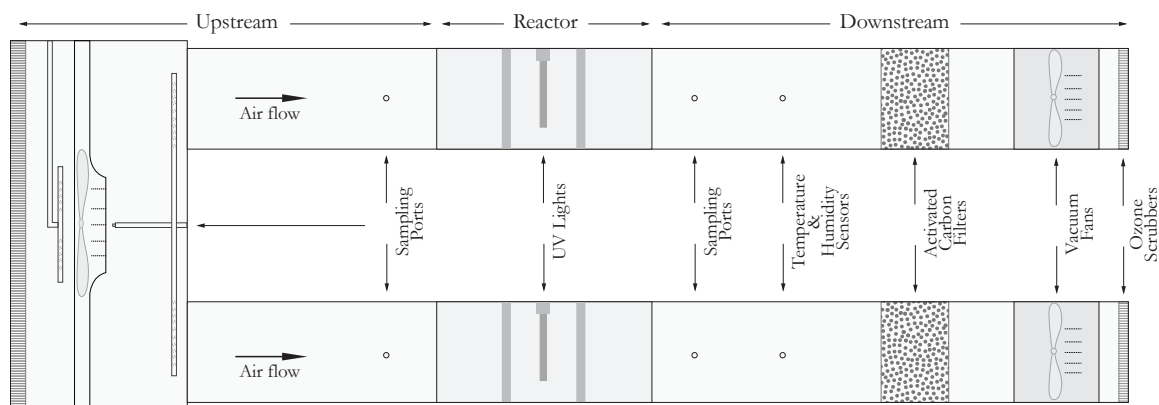
Figure 3-5. Schematic diagram of the experimental apparatus (rear view)

Figure 3-3 shows the location of air flow probe which was located at the upstream and the location of sampling ports that was used to collect the gas flow from each channel. All sensors were mounted at the same distance in all ducts.

3.2.2. Generation System

The challenge chemicals were injected as pure liquid chemical into the injection port at the upstream using two different methods: a *syringe pump* and *bubbling* (pure liquid vaporization) system. These two generation systems were used to vaporize the chemicals by different techniques before introduction into the system.

The syringe injection method was used for the generation of chemicals with low to medium boiling points (with b.p. up to about 140ºC) down to part per billion levels by a *KDScientific* (KDS-210) syringe pumping device and *Hamilton* gas-tight syringes. The accuracy of injection apparatus was limited to the accuracy of motor driven injector and dilution of the infusion liquid [1]. The precision of the motor injector is about 1% RSD, which makes this method much more accurate than bubbling system. The *polytetrafluoroethylene* (PTFE) tubing was used for all the connections in the system.

The bubbling generation system was used for heavier compounds (e.g. Nonane, n-decane and undecane) with high boiling points of >150ºC. In this method a stream of clean dry air (laboratory compressed air) was used as carrier gas. The flow rate of air was controlled by a mass flow controller (Omega FMA 5400/5500). First the carrier gas was passed through a warm liquid chemical bottle, which made the airstream become almost saturated; then this saturated gas passed through an empty bottle to remove any potential droplets from the gas stream. The flow was then introduced to the system at the injection point (Fig. 3-2), and finally it was mixed with the main upstream flow to produce a uniform and stable gas concentration. Inside the system, the injection point was located just after the axial fan that introduced the air through the system (Fig. 3-4). This fan allowed to have a good mixing of chemical vapor with the air before entering each duct channels. Figure 3-6 shows the diagram of bubbling generation system.
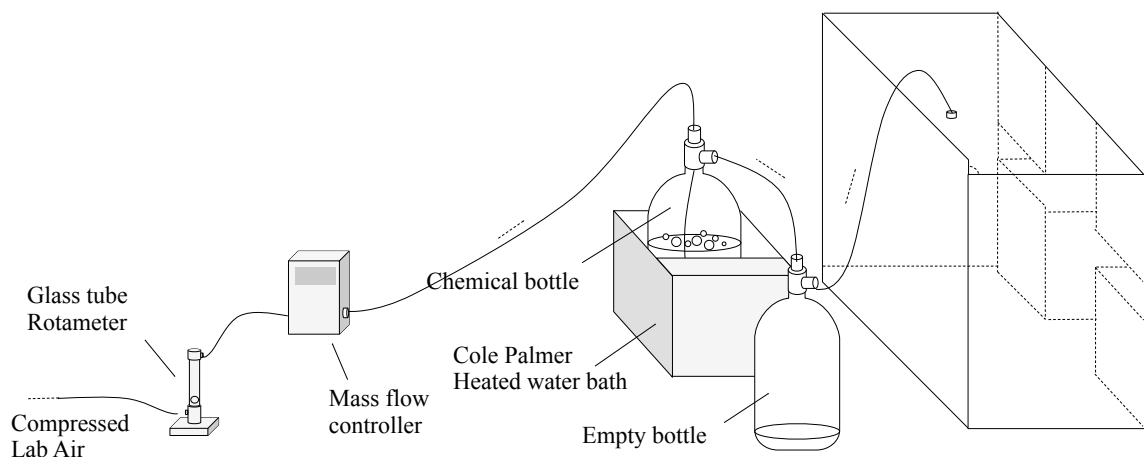
Figure 3-6. Bubbling generation system

A primary air flow meter calibrator (*DryCal®* DC-Lite) was used to set the mass flow meter prior each test. The challenge gas concentration was regulated by adjusting the flow rate of stream gas. Bubbling system method was used with high ppm concentration level tests. For bubbling system, a higher proportion of the total airflow for low level concentrations was needed; this matter caused some instability in the uniformity of concentration in the ppb level concentrations. Hence, it was possible to generate more uniform low level concentrations with a syringe pumping system.

3.3. Chemicals

The chemicals were used with highest purity as followings: Acetone (99.5%, ACS Certificate), 2-Butanone (99.9%, Fisher Certificate ACS), Toluene (99.9%, Fisher HPLC Grade), p-Xylene (99.9%, Fisher Certified), Ethanol (99% Absolute Alcohol, SAQ), n-Propanol (Fisher Certified), 1-Butanol (99.4%, Fisher ACS Grade), sec-Butanol (99.8%, Fisher Certified), 3-Pentanol (98%, ACROS), iso-Pentane (95%, Fisher Certified), n-Pentane (99.7%, Fisher HPLC Grade), n-Hexane (99%, Fisher Optima), n-Octane (95%, Fisher Reagent), n-Nonane (98.5%, ACROS) and Undecane (99%, ACROS).

3.4. Sampling Method

To assess the system performance, the concentration of VOCs at the upstream and downstream were measured in each duct. To have a uniform concentration, the system

was monitored continuously to verify a similar air flow rate in each duct. The flow rate was usually set to a certain amount of 100 (±10%) cfm for each channel. Two sampling ports were installed on each duct; one before and one after the PCO filters zone. Each sampling point had a copper tube fitting union tee that divided into two ports for sampling at each point, one for *Air Toxics®* tubes (to be used for ATD-GC-MS analysis) and another one for *LpDNPH S10* cartridges coupled after one KI or MnO_2 ozone scrubber (to be used for HPLC analysis). As shown in Figure 3-7, each sampling line was connected to an air sampler (*GilAir*, Sensidyne) to create a constant sampling rate of 1-1.5 L/min for DNPH cartridges with 50 ml/min for *Air Toxics®* sampling tubes. Figure 3-7 illustrates the schematic diagram of described manual sampling procedure for one duct.
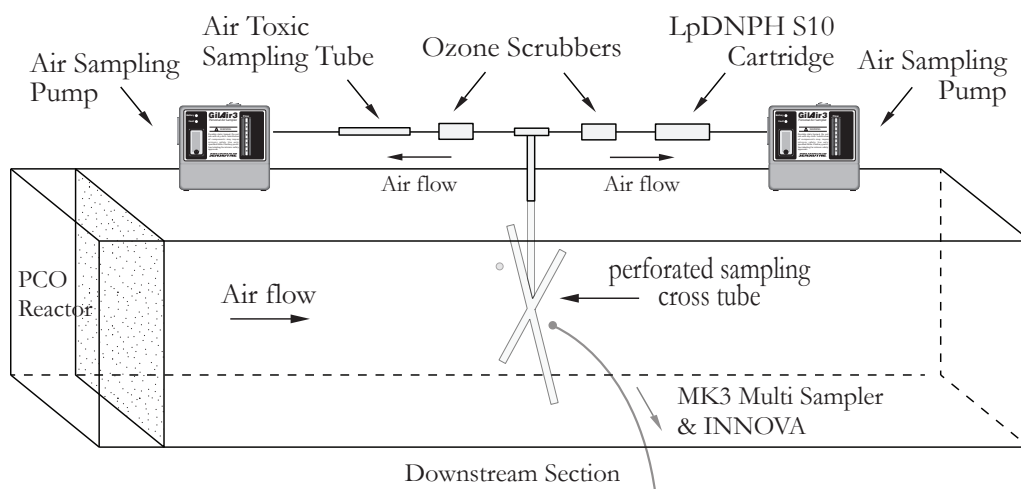
Figure 3-7. Schematic diagram of air sampling system in one duct

Then, ATD/GC-MS was used to analyze the collected air inside *Air Toxics®* tubes. The ATD-GC/MS analysis method procedure is described in details at Appendix 3.

The INNOVA was connected to an automatic multichannel sampler (*CAI*, MK3) to continuously measure TVOC concentration at the upstream and downstream of each duct (Figure 3-7).
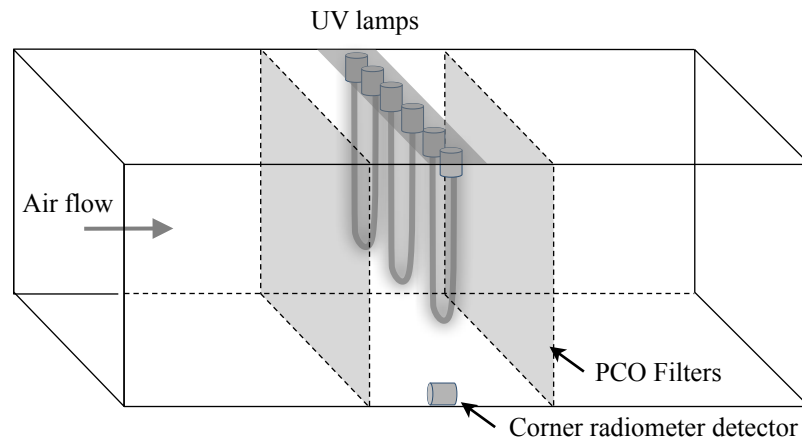
Figure 3-8. UV lamps configuration

In case of using VUV lamps, the ozone level of each channel was measured continuously during the test. The difference of ozone level concentration at the upstream and downstream could determine the extent of ozone interference in the PCO system. It should be noted that the amount of irradiation for each lamp, even same model, was slightly different; for this reason the irradiation level of each lamp was measured and recorded individually. These irradiation tests were repeated periodically to determine the performance of UV lamps for the entire study period. The result is reported in Appendix 2.

3.7. Catalyst Preparation

TiO_2 is known to be an interesting semiconductor material for photocatalytic reactions due to its unique structure and extraordinary properties. The photoactivity of titanium dioxide is mainly related to high UV absorption and its wide energy band gap. The high surface area to the volume ratio of nano TiO_2 makes it possible to undergo surface reactions induced by lower activation energy. It is nontoxic, inexpensive and extremely stable during the photo chemical reactions. These features have drawn many interest to use merely this compound or combine with other nobel metal elements to obtain higher photocatalytic reaction rate. The key characteristics of a catalyst could be described as high surface area, small crystalline size and responsive to UV region to have high photocatalytic activity for a wide range of VOCs. In this work, the activated-carbon and fiberglass was selected as support materials. Fiberglass is a good candidate since it is

economical, corrosion resistance, semitransparent and has a low absorption ratio [63, 64]. Its structure allows more light penetrates through the cloth and this could lead to have higher reaction rate through the catalyst. The loading amount of TiO_2 particles on the substrate could enhance the overall photocatalytic activity of the catalyst. At low irradiation intensity, some limitations about the movement of electrons and holes could happen (and electron hole recombination phenomena), which could be improved by catalyst geometry and material type. The light absorption is usually restricted by active photocatalytic surfaces, electron-hole formation, recombination and transportation to the catalyst surface. Moreover, unwanted surface reactions with absorbed reactants could decrease the number of active sites and limit the desired reaction rates [65]. Among these parameters, the primary step should focus on maintaining the photocatalytic activity of catalyst with a suitable and powerful UV illumination which somehow can be interpreted as stabilizing surface reactions on a catalyst. This goal could be achieved with modification of a series of operative variables during the catalyst synthesis. For example, the film thickness on the substrate may not be more than a specific amount. It was observed that a high thickness could block the light penetration through the catalyst particles and as a result the photo-degradation of the adsorbed contaminants could be altered afterwards [63].

The *chemical bath deposition* (Dip-coating) and *sol-gel* (SG) were used to deposit nano TiO_2 particles on the substrate. The details of both techniques are described in the following sections. The preparation method could determine the chemical structure and physical properties of the deposited TiO_2 particles on the substrate. Different TiO_2 structure transforms the surface reactions and affects the removal efficiency of the PCO system. The best and suitable catalyst preparation method was taken from other methods in peer reviewed literature.

The tested catalyst that was used in this study, was capable to be emerged with the mechanical building ventilation systems. Several design factors were considered such as high flow rate, relative humidity and UV lamps efficiency decay at the indoor

temperature. The catalyst aging and fouling effects were among the few factors that should be studied further with longer duration experiments.

3.7.1. Dip-Coating

Dip coating method is a simple solution for film depositing purposes. It can be applied fast and generally gives satisfactorily results in laboratory research experiments under ambient environmental conditions. In dip coating method, the substrate is dipped into a coating solution and after a specific time it is removed from the solution with a controlled speed. The moving substrate creates a fluid boundary layer that is divided into two layers, which the outer layer separates and returns to solution. The film thickness was determined with the solution concentration and pullout speed. The speed of the pullout is a key factor to obtain a uniform and smooth coating layer. This process can be divided into five steps: immersion, soaking, pullout, drainage, evaporation period and conventional heat treatment. The whole treatment may be repeated several times to achieve the desired film thickness. This method can be applied successfully to obtain uniform films on the flat surfaces, but it cannot be applied for complex surfaces with non flat surfaces namely fiber cloths. To find out why it is not easy to obtain uniform film for fibrous surfaces, it is better to look at the underlying physics and interaction of the driving forces in this process. The thickness and uniformity of the produced film were controlled with several physical forces between the solution and the film substrate [66]:

i) Viscous drag upward on the solution by the moving substrate; ii) Gravity force; iii) surface tension force of meniscus; iv) inertial force of liquid's boundary condition at the deposition area; v) disjoining and conjoining pressure (especially for coating thickness less than 1 μm).

In a standard dip-coating procedure, a flat substrate is removed with constant speed from the solution bath in vertical or horizontal position. A thin liquid film is created on the moving substate, and during the solvent evaporation, the fluid film profile looks like a wedging shape. This non uniform shape can produce a non consistent dried film of nano-titanium dioxides on the substrate. This non uniformity can be extended with more

complex surfaces with concave shapes like fibrous woven material with different angle of fibers. The produced liquid film profile for the fiber is expected to be a parabolic shape where it can cause more titanium dioxide particles be deposited on the non vertical parts during the evaporation period. Figure 3-9A (left) shows the parabolic shape of dried TiO_2 film on a glass fiber.

To solve the problem, a series of experiments was carried out with a binary solution (1:10) of ethanol as the primary solution. The difference in the surface tension and evaporation rate could change the shape of produced film profile. The volatile phase was contributed to faster evaporation and the difference in surface tension decreased the parabolic features that produced more uniform drying process. To control the size and shape of nano-crystalline colloidal of metal oxide film, this method also was combined with sol-gel method to produce more uniform and finer film which could not be achieved by traditional dip-coating methods [67]. The immobilization of titanium dioxide film was one of the key considerations that was considered in the synthesis development procedure. Moreover, the development of a suitable method to efficiently immobilize the particles and meanwhile maintaining the PCO reactivity of catalyst to degrade the indoor air VOCs was one of the main challenges.

3.7.2. Sol-Gel (SG)

Due to broad application of sol-gel in different industries specially in catalysis, polymer and coating industry, there have been extensive research efforts to improve the photocatalytic activity of the titanium dioxide and an effort to optimize the properties of a film for particular applications. The TiO_2 catalysts with SG technique have been used successfully in different applications such as dye-sensitized solar cell [68], self-cleaning glasses and degradation of indoor air pollutants [69]. In many cases, the sol-gel technique is the only possible choice to employ TiO_2 as photocatalyst, since it could be used to produce many different forms of TiO_2, such as powder, coating film or composites. A metal alkoxide (-RO) solution is generally used as the primary solution. The selection of solvent depends on the titanium source and desired type of nanostructure product. It is possible to use water or alcohols with some proactive compounds such as inorganic acids

or specific polymers. The diversity of SG technique enables to obtain the desired structure with specific characteristics [70].

In the SG process, a metal oxide as primary precursor may undergoes several hydrolysis, polycondensation and dehydration processes in an acidic medium with following steps [71]:

Hydrolysis: $$Ti(OR)_n + nH_2O \rightarrow Ti(OR)_{n-1}(OH) + nROH \qquad \text{(3-1)}$$

Condensation: $$Ti(OR)_n + Ti(OR)_{n-1}(OH) \rightarrow Ti_2O(OR)_{2n-2} + nROH \qquad \text{(3-2)}$$

Dealcoholation: $$2Ti(OR)_{n-1}(OH) \rightarrow Ti_2O(OR)_{2n-2} + nH_2O \qquad \text{(3-3)}$$

Overall Reaction: $$Ti(OR)_n + \tfrac{n}{2}H_2O \rightarrow Ti(OR)_{n/2} + nROH \qquad \text{(3-4)}$$
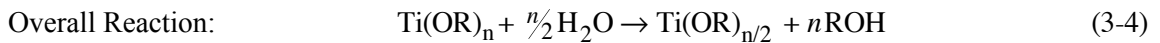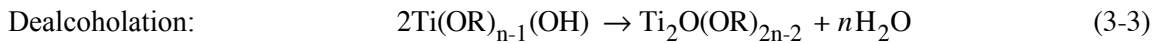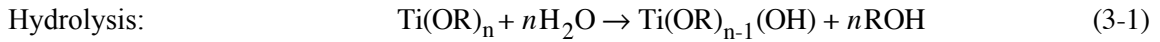
where, R can be ethyl, i-propyl, n-butyl, etc. In the above reactions, titanium alkoxides hydrolysis could happen in presence of water and subsequently the polymerization leads to creation of a metal oxide network. To control the speed of hydrolysis reaction, alcohols may be added into the solution. Alcohol acts as liaison between titanium alkoxide and water. The polarity of alcohols can produce a bond between non polar titanium alkoxide and polar water. To achieve a good homogeneity, it is also necessary to control both temperature and pressure of the synthesis process at a certain level. The stability and morphology of the produced sol is strongly related to the molar ratio of titanium alkoxide, water and the pH of the solution. Generally, a variation of these parameters could be used to achieve various geometries, e.g. nano-crystals, thin films or bulk powders. The required structure could be obtained by manipulating solvent supersaturation, chemical concentration and kinetic control. The ability of controlling size and shape of particle makes the SG technique an attractive, flexible and facile solution for different industrial applications[6].

---

[6] Sigma-Aldrich technical paper

Sol-gel Process Steps Summary

Starting Precursor
(Metal Alkoxide)
+
(Solvent + Stabilizer
+ Chelating Agent)

Hydrolysis ——————→ ⊙ Dip/Spin coating

+ Polymerization ——————→ ♨ Drying/Calcination
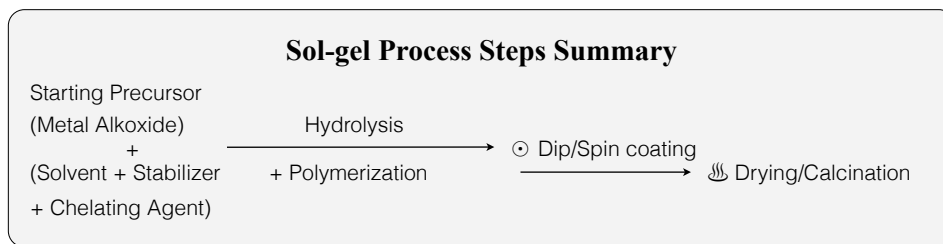
In the photocatalytic oxidation process, it is needed to reduce the size of nano particle of metal oxide with more photoactive crystallographic orientation, such as TiO_2 anatase form which has been shown a better photocatalytic activity in compare to other two structures; brookite and rutile [18]. An effective technique such as SG method could be used to achieve very uniform and thin layers of TiO_2 with specific crystalline structure.

In the catalyst development tests, the properties and reactivity of synthesized catalyst were compared with a commercial P25 TiO_2 catalyst. The commercial P25 titania powder was bought from *Sigma-Aldrich Co.* where it generally synthesized by industrial processes from titanium tetrachloride ($TiCl_4$) or sulfate vapor by flame process technique. The reported values for TiO_2 (P25) for phase composition ratio and crystallite size values are slightly different. These inconsistency are generally related to the quality of produced TiO_2 within and between each batch production line. To avoid this problem, the same batch of commercial TiO_2 (P25) was used throughout the experiment. The anatase phase percentage for P25 was between 0.7-0.8, with 21nm particle size, 50 (±15) m^2/g BET surface area and pH value of 3.5-4.5.
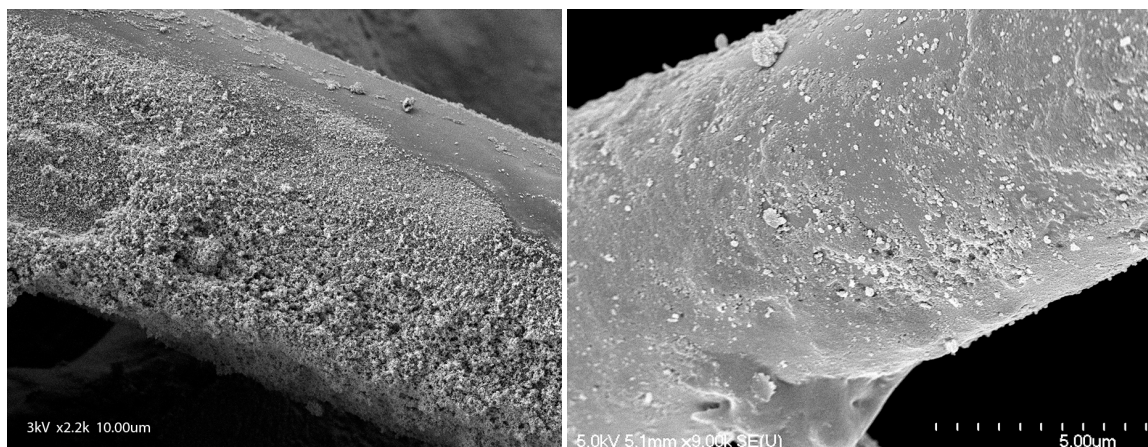
Figure 3-9A. SEM image of dip-coated nano TiO_2 film on two different fiberglass: (right) FG-I, (left) FG-II

The powder morphology of prepared TiO_2 catalysts was determined by SEM. Figure 3-9A shows the SEM micrograph of TiO_2-FG type I and II which were prepared with dip-coating method. The SEM images were taken from TiO_2 coated fiberglass by a high resolution field emission scanning electron microscope (Jeol JSM-7400F).
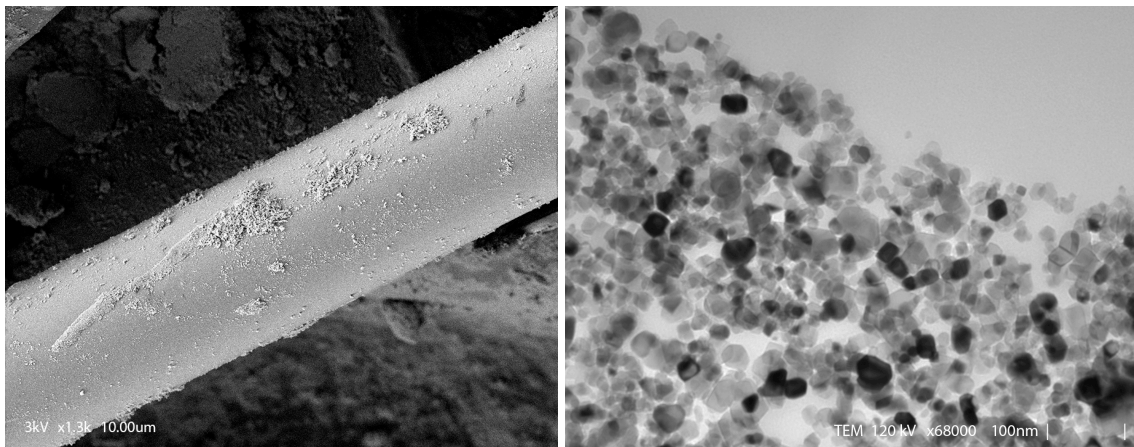
Figure 3-9B. (right) TEM image from commercial TiO_2, (left) SEM image of SG-FG-III

Figure 3-9A (right) shows that how the gravity force changed the shape of drying film to a parabolic shape with TiO_2 particle agglomeration on the fiber surface. This indicates that the weak interface between TiO_2 particle and fiber glass could lead to the particle debonding during the drying period. The possibility of TiO_2 particle detachment is one of the drawbacks of dip coating method for smooth and elastic substrates such as glass fiber and carbon fiber cloths (Figure 3-9A, left).

Figure 3-9B (left) shows the coated TiO_2 film prepared by the described SG method. The TiO_2 film has a uniform and complete coating with small agglomeration of TiO_2 on the fiber glass fiber. Figure 3-9B (right) shows the TEM image from a commercial TiO_2 nano particles that was used to prepare FG-I catalyst.

The specific surface area and porosity of the catalysts were calculated by *Density Function Theory* (DFT) method from BET measurement analysis (Appendix 4). The meso-porosity of fiber glass with smaller pore size distribution (~5nm) less than average nano TiO_2 particle size (~20nm) could increase the coverage of catalyst with lower amount of TiO_2 compare to other substrate with higher pore size in macro range. By

comparing the BET surface area of two fiber glass catalysts, the specific surface area of fiber glass type B (10 m^2/g) is less than type A (99 m^2/g) and small pore size of all catalysts decreased the adsorption rate and transport of reactants to coated TiO$_2$ film. The low adsorption rate of TiO$_2$-FG catalysts could help to reduce the effect of adsorption on the overall PCO reaction rates. It also reduced the possibility of pore blockage and loss of activity of active size, which could result from unwanted secondary reactions. The physical characteristics of tested TiO$_2$/FG catalysts are presented in Table 3-1.

Table 3-1. Physical characteristics of TiO$_2$/FG catalysts

	BET surface area (m^2/g)	Fiber diameter (µm)	Film thickness (µm)	Porosity ε	Avg. pore size (nm)	Avg. TiO$_2$ loading (g/m^2)
FG-I	98.89	90	5	0.6	4.5	34.1
FG-II	8.98	80	19	0.5	3	28.4
FG-III	10.73	80	10	0.45	3	25.1

3.7.3. Preparation Method Description

The first catalyst series (FG-I) was obtained from a commercial manufacturer. It has been prepared with a proprietary TiO$_2$ solution and dip-coating method. The substrate material for FG-II, III was obtained from a commercial supplier, where TiO$_2$ was coated on fiber glass fibers. The media was immersed into the prepared solution for 5 min (FG-I), 30 and 60 min (FG-II, III) with a uniform pulling rate of average 10, 5 mm.s^{-1} respectively. Then, the wet catalysts were dried in an oven up to 100ºC (FG-I) and 150~325ºC (FG-II, III) for two hours (5~10ºC/min). A pre-thermal treatment was employed to stabilize the thermal resistibility of catalysts. The post-thermal treatment was a necessary step that could increase the stability and adhesion of film structure. A high temperature helps to remove the excess residue moisture from deposited TiO$_2$ layer. The film volume starts to shrink with thermal expansion of substrate at the same time. It was observed that the film structure gradually densifies during the heating time. A slow heating and cooling ramp reduce the temperature difference stresses and meanwhile maintains the mechanical structures between film and substrate [72]. On the other hand, the maximum allowable

temperature was limited to the glass fiber material could withstand. The maximum temperature for FG-I and FG-II, III were 110ºC and 350ºC respectively.
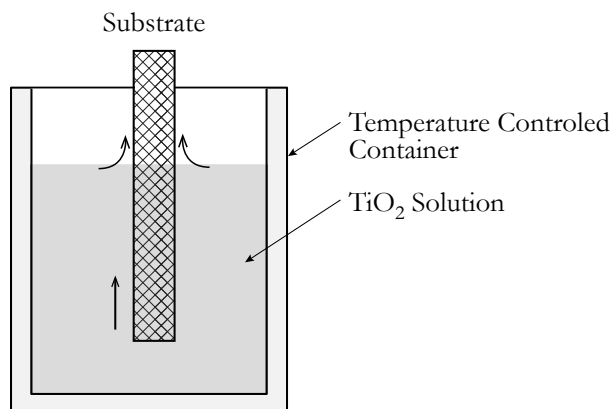
Figure 3-10. Technique used for the dip-coating and sol-gel coating of substrate

The second catalyst series (TiO$_2$-FG-II) were prepared with an optimized dip-coating method. In the optimized procedure, several parameters such as TiO$_2$ solution concentration, temperature of solution, withdrawal rate were optimized accordingly (Figure 3-10). A different type of glass fiber with low surface area was used as the substrate. The selected fiberglass cloth with one inch thickness fabricated with open weave pattern, the open pattern could alter the airflow direction in different directions which could create a better surface contact between air and titanium dioxide particles.

To evaluate the effect of catalyst thickness on efficiency of UV-PCO system, a series of experiments were carried out with increased PCO catalyst thickness from 0.95 cm to 1.9 cm. The increased filter thickness could extend the residence time of the VOCs, which improved the overall removal efficiency of system up to 0.10%. The experiments were performed with ethanol at 0.5 ppm and 15-30 %RH.

An aqueous solution of titanium powder (Aeroxide® P25 titanium dioxide nano-powder) with high purity of 99.5% was selected as a primary dip-coating solution. The new fiberglass cloth was dip-coated for 1~2 hours, and then the wetted cloth was dried in normal lab temperature conditions for two days. It was observed that this duration was enough to have a natural drying process. At this point, any bending in the catalyst fibers could lead to the coating fracture and film separation from the substrate [73]. The

catalysts were directly transferred into an oven, then it was heated up to 150°C for 2 hr (5°C/min).

The third catalyst batch were prepared with SG method, a synthesized titanium dioxide solution was used as the dipping solution. The media was immersed into the prepared solution for a 60~120 minutes. Then, the wet cloth was dried in an oven at 225~325°C for two hours (10°C/min).

The SG solution was prepared from tetrabutyl titanate $Ti(OC_2H_4)_4$ as primary precursor which usually was used to prepare nano anatase crystalline TiO_2 at room temperature. Tetrabutyl titanate (97%) was dissolved in water, ethanol and hydrochloric acid solution as the starting alkoxide solution with molar ratio of $Ti(OC_2H_4)_4:H_2O:C_2H_5OH:HCL = 1:1:15:0.2$. The solution was vigorously stirred and then held at 0°C temperature for 2 hrs before it was left to rest for 24 hrs at 20°C. The fiber glass substrate was dip coated into TiO_2 sol solution with the described method.

The reactivity of metal oxides with water is strongly dependent on pH and temperature. The effect of pH on hydrolysis and condensation rate of SG solution is shown in figure 3-12. The hydrolysis rate was stabilized by several controlling variables: pH, temperature and the ratio of water/alkoxide in the solution.

Table 3-2. Experimental design composition of TiO₂-FG catalysts

Symbol	Substrate Type	Thickness (μm)	TiO$_2$ (g.m^{-2})	Method
FG-I	FG-A	5	34.1	DC
FG-II	FG-B	19	28.4	DC+
FG-III	FG-B	10	25.5	SG

FG: fiber glass; DC: dip-coating; DC+: optimized dip-coating; SG: sol-gel

The film thickness of coated TiO_2 was controlled by two parameters for each catalyst in dip-coating procedure: the ratio of solution concentration and withdrawal rate of coating substrate. The TiO_2 solution concentration of TiO_2-FG-I was unknown, since it was obtained from a commercial supplier. The solution concentration of TiO_2-FG-II was 1:12 in molar ratio.

The best solution concentration was determined by several preliminary experiments to determine the best thickness of each catalyst. The film thickness of prepared catalysts were determined from SEM analysis. The lowest film thickness could be obtained by sol-gel method with 2 μm thickness with once dip-coating. The TiO_2-FG-III was prepared by sol-gel method with four times dip-coating in the TiO_2 gel solution.
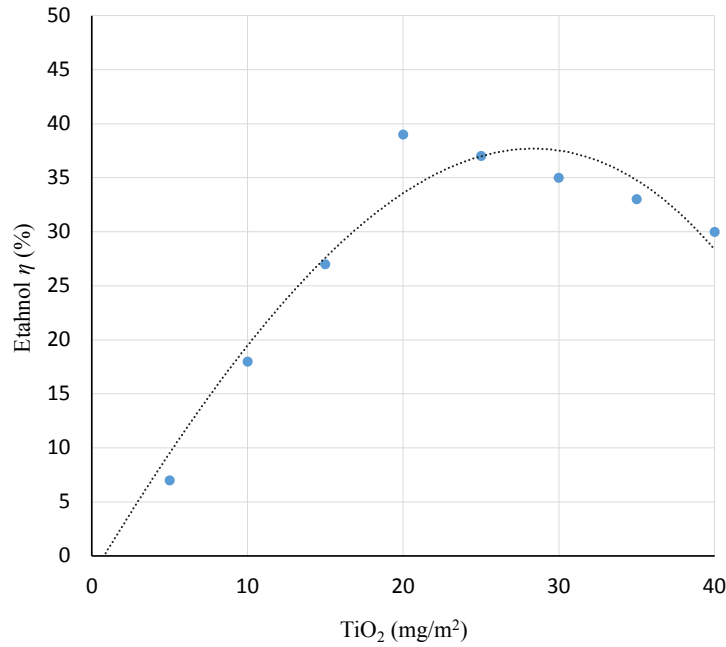
Figure 3-11. Effect of TiO_2 loading on removal efficiency of ethanol with TiO_2-FG-III
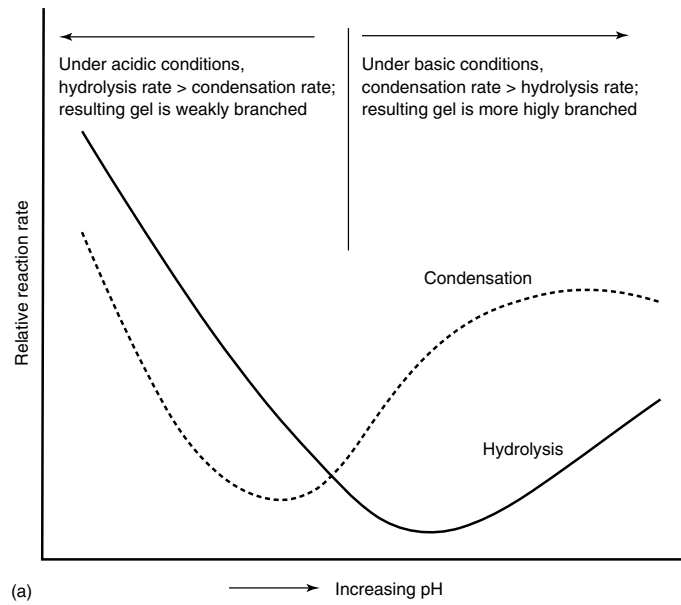
Figure 3-12. Effect of pH on hydrolysis and condensation rate in SG method [74]

Figure 3-11 shows the effect TiO_2 loading per unit surface area on removal efficiency of ethanol, where the different loading of catalyst was obtained with the number of dip-coating with SG solution at steady state test conditions (20ºC, 35% RH).

3.7.3. Ozone Interference

For ozone producing UV lamps, an ozone scrubber was installed before the sampling tubes to prevent any ozone reaction interference with the *Air Toxics*® sampling tubes. Potassium iodide, KI, scrubbers (S10L Ozone Scrubber, SUPELCO) were used for the manual sampling procedures (Figure 3-7). The preliminary test data revealed that KI type scrubber capacity is not enough to completely remove 100% ozone for high concentration ozone and long term experiments. The capacity of the ozone scrubber may be calculated from measured ozone concentration during each experiment. The KI scrubber had capacity of 100 ppm/h at 200 ppb ozone level, 25°C and 50% RH. Each ozone scrubber contains 1.5g crystalline *potassium iodide* (KI) that can trap ozone to prevent possible negative interferences such as sampling loss and degradation of some reactive VOCs.

In high level ozone concentration, it is better to use manganese dioxide (MnO_2) ozone scrubbers that can efficiently remove up to 95% ozone in the similar experimental conditions [75]. The MnO_2 ozone scrubbers have high capacity for long period tests and it has been shown that they could be used continuously for more than three months. While the KI ozone scrubber capacity may be limited to 1-2 working days with moderate ozone concentration (70~80ppb) [76].
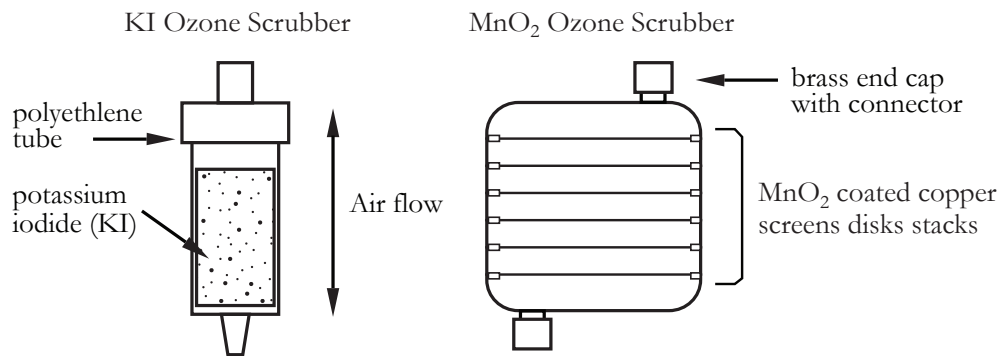
Figure 3-13. Schematic of KI and MnO_2 ozone scrubbers

The used MnO_2 scrubber consisted of several stacks of coated copper screens in one cartridge. Figure 3-13 shows the detailed structure of both described ozone scrubbers (KI and MnO_2).

```
                          ┌─────────┐
                          │   VOC   │
                          └─────────┘
        ┌────────────────────┼────────────────────┐
        ▼                    ▼                    ▼
 ┌──────────────┐    ┌──────────────┐    ┌──────────────┐
 │ Ozone reaction│   │     PCO      │    │      OH      │
 └──────────────┘    └──────────────┘    └──────────────┘
```

Figure 3-14. VOCs reactions, common intermediate classes and products flow chart [77]

Figure 3-14 shows the possible reactions with different classes of intermediates and byproducts in the UV-PCO system. The ozone presence increases the number of hydroxyl radicals and $\bullet O_2^-$ radicals in the system as following reactions:

$$O_{2\,ads} + e^- \rightarrow \bullet O_{2\,ads}^- \xrightarrow{+O_3} \bullet O_{3\,ads}^- + O_2 \xrightarrow{TiO_2} \bullet O^- + O_2 \quad (3-5)$$

$$O_{3\,ads} + e^- \rightarrow \bullet O^- + O_2 \quad (3-6)$$

In the presence of water vapor, the ozone reactions with water molecules could intensify the hydroxyl radical production:

$$\bullet O_{3\,ads}^- + H_2O \xrightarrow{TiO_2} OH\bullet + O_2 + OH^- \quad (3-7)$$

The used MnO_2 scrubber consisted of several stacks of coated copper screens in one cartridge. Figure 3-13 shows the detailed structure of both described ozone scrubbers (KI and MnO_2).

Figure 3-14. VOCs reactions, common intermediate classes and products flow chart [77]

Figure 3-14 shows the possible reactions with different classes of intermediates and byproducts in the UV-PCO system. The ozone presence increases the number of hydroxyl radicals and $\bullet O_2^-$ radicals in the system as following reactions:

$$O_{2\,ads} + e^- \rightarrow \bullet O_{2\,ads}^- \xrightarrow{+O_3} \bullet O_{3\,ads}^- + O_2 \xrightarrow{TiO_2} \bullet O^- + O_2 \quad (3-5)$$

$$O_{3\,ads} + e^- \rightarrow \bullet O^- + O_2 \quad (3-6)$$

In the presence of water vapor, the ozone reactions with water molecules could intensify the hydroxyl radical production:

$$\bullet O_{3\,ads}^- + H_2O \xrightarrow{TiO_2} OH\bullet + O_2 + OH^- \quad (3-7)$$
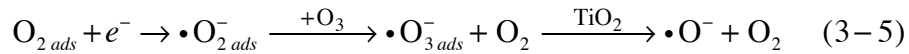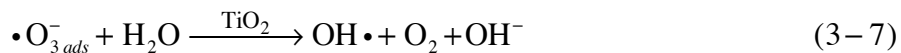
3.8. Preliminary Experiments

The system reliability was measured with a series of pre-qualification tests before the experiments. A series of calibration tests was performed: concentration, flow, leaking, and adsorption tests [78]. The concentration tests were carried out to confirm the uniformity of the injected gas and uniform dispersion of the injected gas through the four channels. The concentration tests were carried out without installation of UV lamps and PCO filters to avoid adsorption. The concentration tests quantitatively verified that the experimental data are reliable and the resulted concentration are comparable for all channels. The pre-qualification tests were carried out at the same conditions as the main experiments. The pre-tests include:

Air velocity uniformity test: Figure 3-15 shows the deviation of measured air flow rate during a test period. The experiments were carried out at flow rate of 110 cfm with accuracy of (±10%). The air flow rate was assumed as a uniform velocity, which was a prerequisite factor to ensure a uniform concentration distribution in each duct.

Concentration uniformity test: The concentration uniformity of all four channels were confirmed using the photoacoustic multi-gas analyzer (INNOVA 1312) [79].
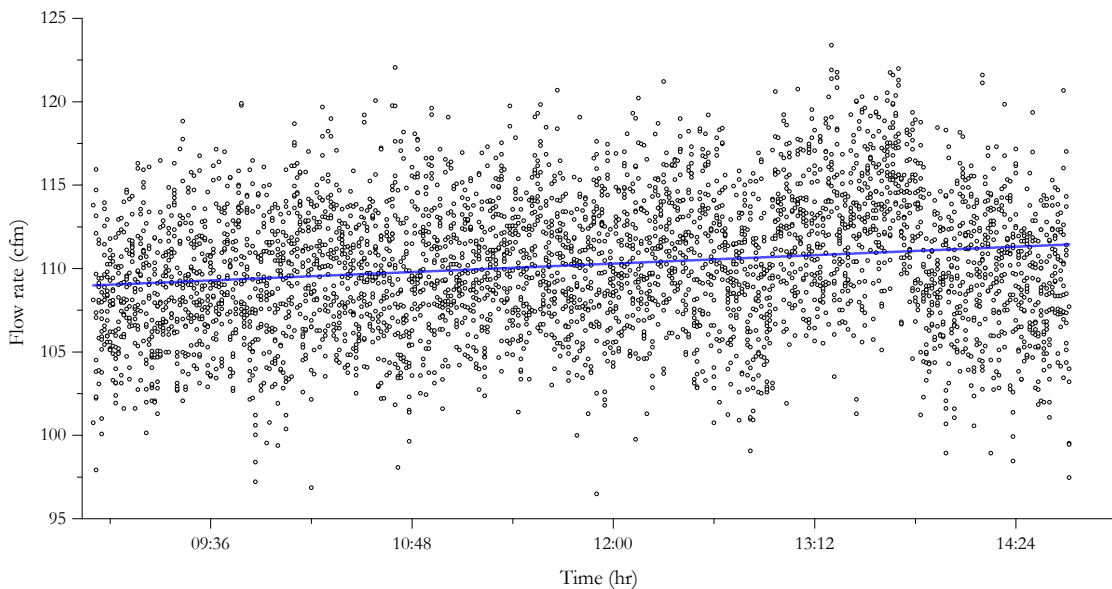
Figure 3-15. Measured air flow rate versus time inside one channel
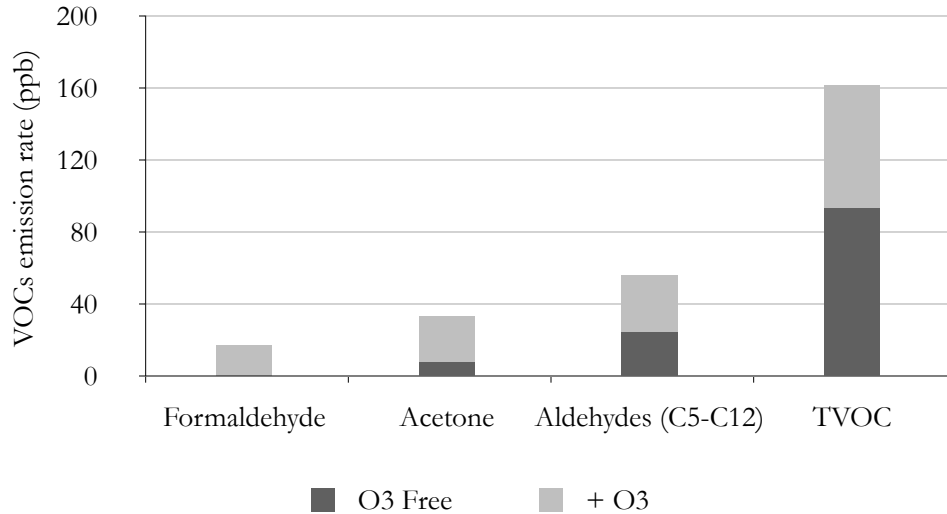
Figure 3-16. VOCs emission rates from an empty duct after 1 hour ozone exposure

Gasket interference test: The system was sealed with neoprene gasket. The sealant material was similar to the materials typically used as duct liner in mechanical ventilation systems. In case of zone generating UV lamps, it was observed that the emission rate of VOCs was higher than ozone free UV lamps. The identified compounds in the gas-phase at downstream were listed in figure 3-16.

UV lamps irradiation test: The intensity of UV lamps were measured for each ducts and the measurement results are shown in Figure A2-3 (Appendix 2). The performance of UV light intensity was continuously monitored throughout the experiments.

3.9. Experimental Test Procedure

• The PCO catalysts were installed inside the system with described locations in section 3.2.1. The old catalysts (except TiO_2-FG-I) were changed with new catalysts after each VOC test to eliminate the possible catalyst fouling or loss of active sites in the catalysts.

• The sampling pumps were calibrated with each *Air Toxic*® sampling tube as described flow rate for each experiment. Since the pressure drop of all *Air Toxic*® tubes were not identical, the tubes were calibrated separately for each channel. The calibration procedure was the same as described in section 3.4.

- After the system fans were turned on, the air flow rate for each separate channels were adjusted manually to 2.83~3.11 m^3/min (100~110 cfm). The flow rate was continuously monitored with the DAS system which offers online monitoring of all sensors for each separate channel. The system was let to run for 15-20 minutes until the flow rate became stabilized. At the same time, the background humidity and temperature of all channels plus concentration of TVOCs were monitored with INNOVA. In case of ozone UV generation lamps, the ozone concentration was monitored with a multichannel zone monitor (as described in Appendix 5).

- The UV lamps power turned on. The system was allowed to run for 5 minutes until the radiation became stable.

- The injection system was started to introduce the challenge gas at a specified concentration into the system. After starting the injection, it was allowed to operate for 30 minutes until the concentration became stable in the system.

- The manual sampling was collected with conditioned *Air Toxic*® tubes as illustrated in Figure 3.7. (the required sampling time was different for different concentrations. The sampling period for GC analysis was changed in the different tests). The sampling repeated every hour throughout the experiment period.

- The HPLC sampling with the DNPH cartridge (Carbonyls) was carried out in parallel to the GC sampling. Since the amount of carbonyls usually was small in comparison with the injected VOC, a longer sampling time was required to reach a minimum required volume of sample for HPLC analysis. The sampling time for the DNPH cartridges was between 1-2 hours.

- For first catalyst, TiO_2-FG-I, the appearance of catalysts was inspected for any surface discoloration after each experiment. The catalysts were regenerated periodically with UV lights while the system fans were working for 24 hour. In the following experiments, the used catalysts were replaced with new one after each VOC test.

- For other catalysts, TiO_2-FG-II, III, the catalysts were changed after each experiment for any catalyst degradation. Each catalyst was weighed and compared to previous ones to maintain the consistency between each experiment.

A summary of all the test details and corresponding experimental conditions is summarized in Table 3-3.

Table 3-3. Experimental Summary

Group	Name	Concentration (ppm)	T (°C)*	RH (%)	Flow rate (cfm)♀	Catalyst type†	185nm	254nm
Alkanes	iso-Pentane	0.5, 1	21	15, 30	100	FG-II		●
	n-Pentane	0.5, 1	21	15, 30	100	FG-II		●
	n-Hexane	0.25, 0.5, 1.0	25	32	100	FG-I		●
		0.5	25	32	100	FG-I		●
		0.5	22	57	100	FG-I		●
		0.25, 0.5, 1.0	21	57	100	FG-I	●	●
		0.5	22	57	25, 45, 100	FG-I		●
		0.25, 0.5, 1.0	22	15, 27	100	FG-II		●
	n-Heptane	0.5, 1	21	15, 30	100	FG-II		●
	n-Octane	0.25, 0.5, 1.0	25	43	100	FG-I		●
		0.25, 0.5, 1.0	22	15, 30	100	FG-II		●
		0.25, 0.5, 1.0	21	53	100	FG-I	●	●
	n-Nonane	0.5, 1	23	15, 30	100	FG-II		●
	Undecane	0.5, 1	21	15, 30	100	FG-II		●
Alcohols	Ethanol	0.5	22	9, **15**, **30**, 43, 56	100	FG-I		●
		0.5	22	53	25, 45, 100	FG-I		●
		0.25, 0.5, 1.0	25	15	100	FG-I		●
		0.25, 0.5, 1.0	21	35	100	FG-I	●	●
		0.5, 1.0	21	**15**, 25, **30**	100	FG-II		●
	n-Propanol	0.5, 1.0	22	20, 30	100	FG-II		●
	1-Butanol	0.25, 0.5, 0.8	25	**20**	100	FG-I		●
		0.25, 0.5, 0.8	21	56	100	FG-I	●	●
		0.25, 0.5, 1.0	22	**20**, 30	100	FG-II		●
	sec-Butanol	0.5, 1.0	22	15, 30	100	FG-II		●
	3-Pentanol	1.0	23	30	100	FG-II		●

* The temperature is average value of all four channels. The temperature fluctuation through the test is between ±2°C. | † The catalysts prepared by SG method (TiO₂-FG-III) is not included in this table.
♀ The flow rate deviation through the test is between 10% of reported average value.

3.10. Langmuir Adsorption Isotherm

The adsorption efficiency of the catalysts was measured with Langmuir adsorption isotherm with the VOCs of interest in this study. The adsorption tests were carried out with a concentration range corresponding to the main experiments from 0.5 to 5 ppm at 21°C and 25±5 %RH.

The experiments were performed at the same system conditions as described in Appendix 3. The details of experimental system setup are described in ASHRAE Standard 145.1. The pure liquid VOC was injected into the system, where the PCO filter chamber was located after the injection point. INNOVA was used to measure the upstream and downstream VOC concentration of the system. After about one hour from starting injection time, the concentration was reached a steady condition.

The adsorption coefficient for each individual compound was determined with the described L-H model fitting procedure in section 2.5.1. It should be noted that the assumption of unimolecular Langmuir model applies to the adsorption tests too. The low concentration range of 0.5-1ppm was low enough to have a monolayer coverage assumption for the tested TiO_2-FG catalysts. The adsorbed VOC concentration (C_{ads}) was determined with the following relationship [78]:

$$C_{ads} = \frac{C_{max} K C_{eq}}{1 + K C_{eq}} \xrightarrow{K.C_{eq} \ll 1} \frac{C_{ads}}{C_{max}} = K C_{eq} \qquad (3-8)$$

where, C_{max} is the maximum surface concentration and the adsorbed concentration (C_{ads}) is calculated by subtracting the initial concentration (C_i) from the steady state concentration (C_{eq}). The difference of initial and equilibrium concentration would be negligible at low concentration levels ($KC_{eq} \ll 1$). As a result, the equation could be written as simple form of $C_{ads} = C_{max}.KC_{eq}$, where $C_{max}.K$ is dependent to the maximum monolayer surface coverage of the adsorbing species. This term can be replaced with the mass ratio of the adsorbed VOCs to the catalyst ($m_{VOC}/m_{catalyst}$):

$$\frac{m_{VOC}}{m_{catalyst}} = K C_{eq} \qquad (3-9)$$

The adsorption coefficient (K) was different for tested TiO_2 catalyst, where it could be influenced by both the physical and chemical characteristics of VOC of interest and the physical characteristics of TiO_2 catalyst. Figure 3-17 shows the adsorption isotherm of the tested VOCs for different TiO_2-FG catalysts.
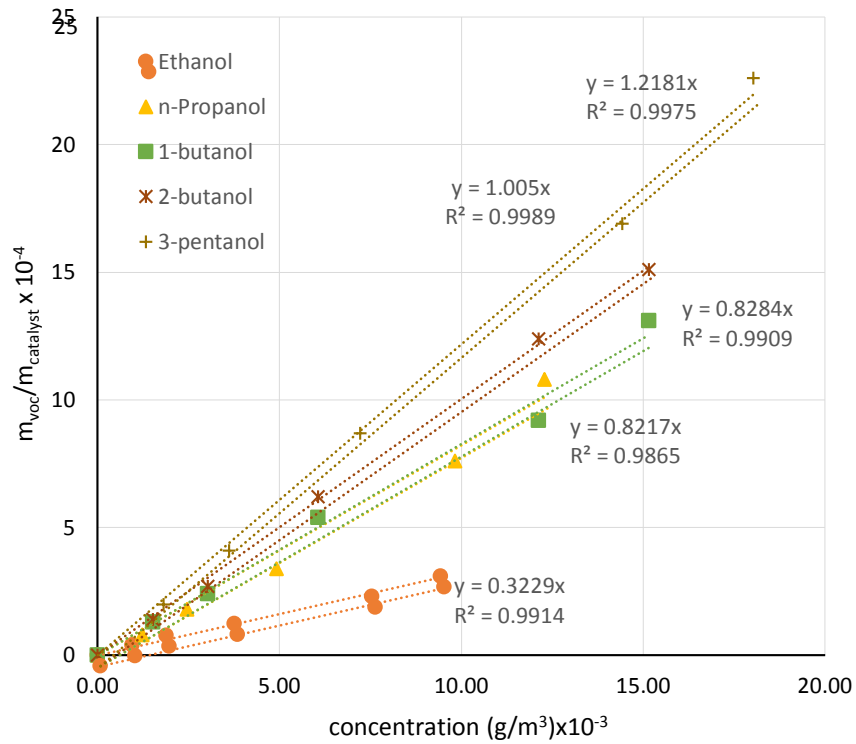
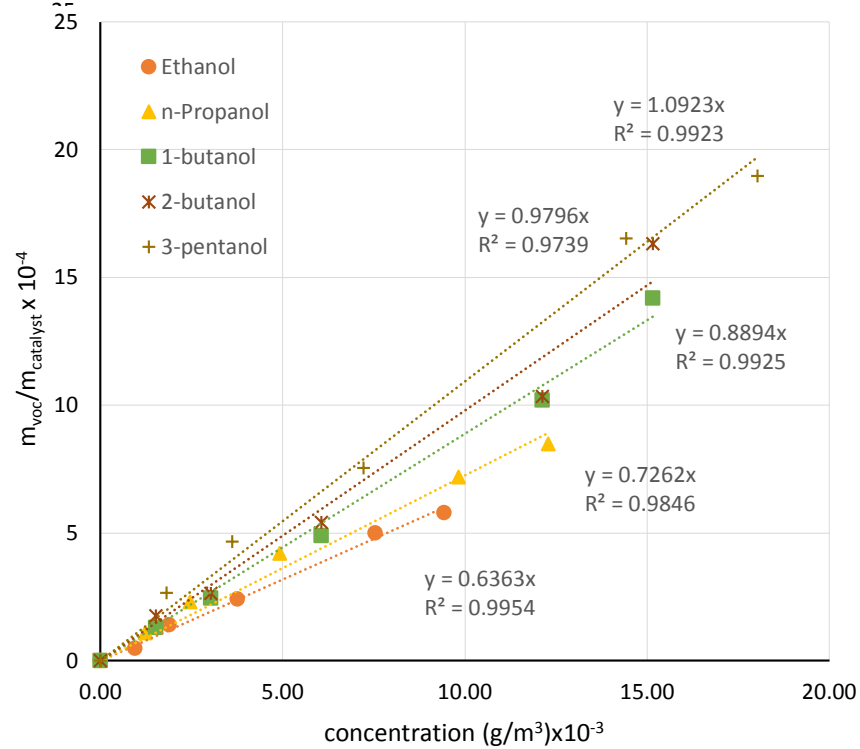Figure 3-17a. Adsorption isotherm of alcohols with TiO_2-FG-I (21°C and 25±5 %RH)

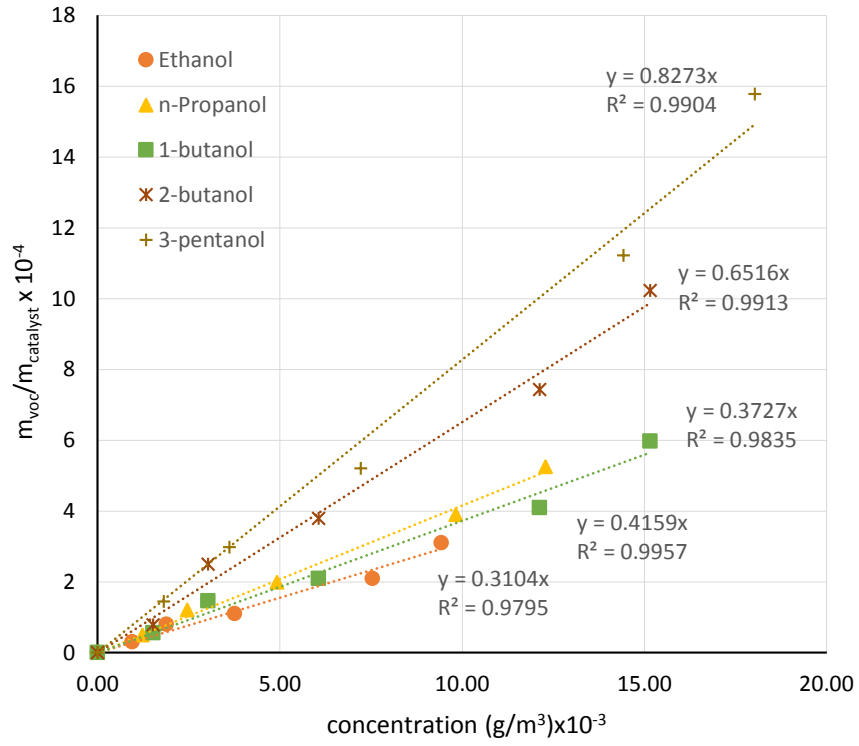Figure 3-17b. Adsorption isotherm of alcohols with TiO_2-FG-II (21°C and 22±5 %RH)

Figure 3-17c. Adsorption isotherm of alcohols with TiO_2-FG-III (21°C and 20±5 %RH)

Chapter IV: Experimental Results

This chapter discusses the data analysis obtained from experiments carried out as described in the previous chapter.

As the PCO reactions closely depend on the environmental test conditions, it was better to study the PCO catalysts performance at steady-state conditions. The steady state conditions allowed to have a practical evaluation of the test system in a controlled environment. For this study, the inlet concentration, relative humidity, temperature, airflow velocity, light irradiance ratio and catalyst weights were assumed to be constant throughout each experiment. Humidity was one of the uncontrollable parameters where it was directly related to outdoor temperature and humidity. The experiments were performed on different days through the year. The average relative humidity percentage in indoor was 45% ($\pm$10) in the summer and 25% ($\pm$10) in the wintertime. Figure 4-1a, b shows the variation of relative humidity and temperature in indoor air during the test. The following sections report the photocatalytic removal efficiency, photochemical reaction mechanisms and related byproducts of alcohols with tested TiO_2 catalysts.

4.1. VOCs Kinetic and Intermediates

4.1.1. Ethanol (C_2H_6O)

Ethanol is the lightest and most common VOC after methanol from alcohol class where it easily emitted from many indoor air sources such as alcoholic drinks, fragrances, household consumable products, food additives and fuels. It is also a pollutant from many urban businesses such as breweries, bakeries and food stores. The simple molecular structure permits to study the kinetic and intermediary surface PCO reactions and its possible byproducts in a simple manner.

Figure 4-2 compares the degradation rate of ethanol as a test VOC and the evolution of acetaldehyde as main gas byproduct compared for different PCO catalysts. The reaction rate constants were determined by fitting the empirical data with different available models such as power low equation, uni or bi-molecular L-H. From the PCO reaction rates, it was possible to estimate the necessary amount of UV light and flow rate for

complete oxidation of different concentrations of VOCs. The PCO reaction rates generally follow a linear relationship with UV irradiance ($r \propto I^{1/2}$) [31] and air flow rate could be used to change the residence time of reactants in the system. For example, the experiments showed the decrease of flow rate from 170 m³/hr to 85 m³/hr could improve the removal efficiency of ethanol up to 5% at 15% relative humidity level.

The generation rate of byproducts for ethanol with different types of TiO_2 catalysts is compared in Figure 4-3. The experiments with 0.25 to 1-ppm ethanol inlet concentrations showed that the oxidation rate of ethanol as the representative of other VOC of interest is not directly related to the catalyst weight, where TiO_2-FG-III had the lowest loading of TiO_2 particles per unit surface area. The TiO_2 loading for each fiber glass (FG) catalyst was as following order: FG-III < FG-II < FG-I (Table 3.2). However, the increase of ethanol oxidation rate was stepped up the production of acetaldehyde and formaldehyde as the main gas-phase byproducts too. There was also very low concentrations of propanal and acetone with HPLC analysis.
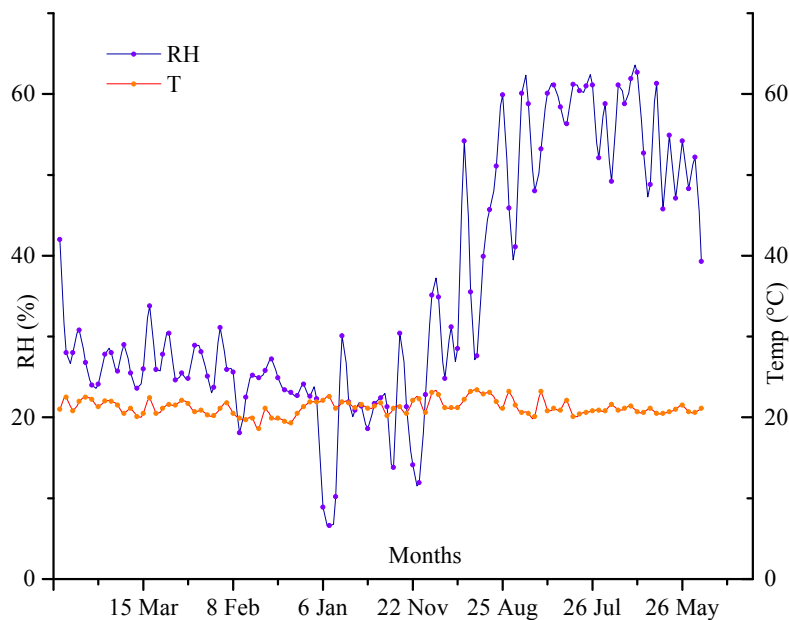

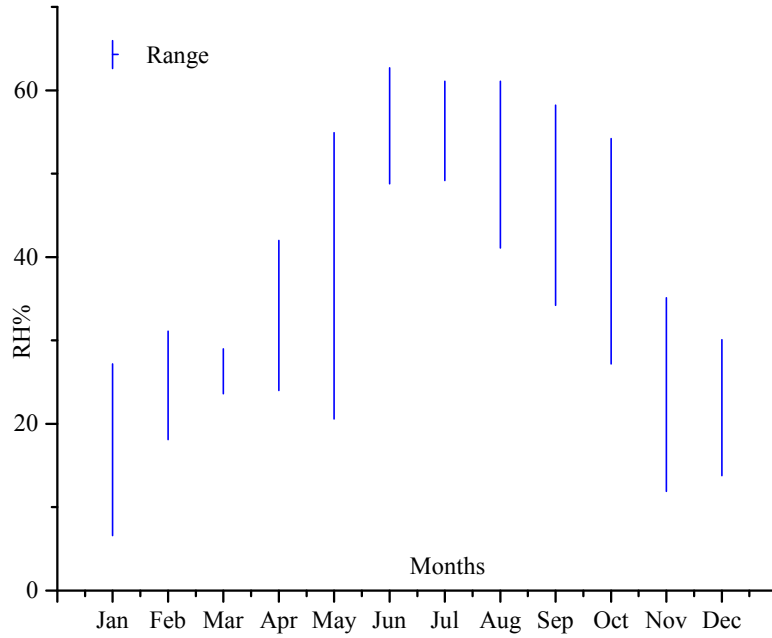Figure 4-1a. Indoor air humidity and temperature changes during the year

Figure 4-1b. Indoor air humidity changes during the year
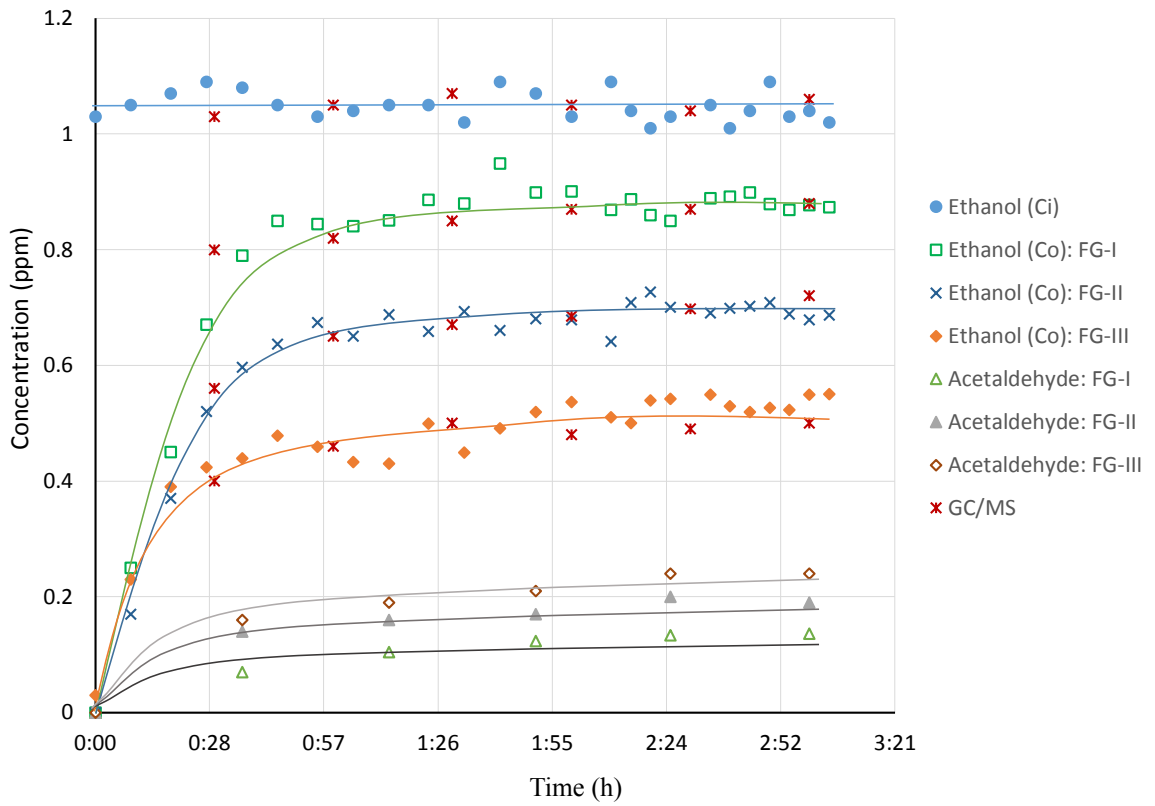
Figure 4-2. Comparison of ethanol conversion rate with different PCO catalysts (20-27% RH, 21ºC, 30 W/m^2)

64
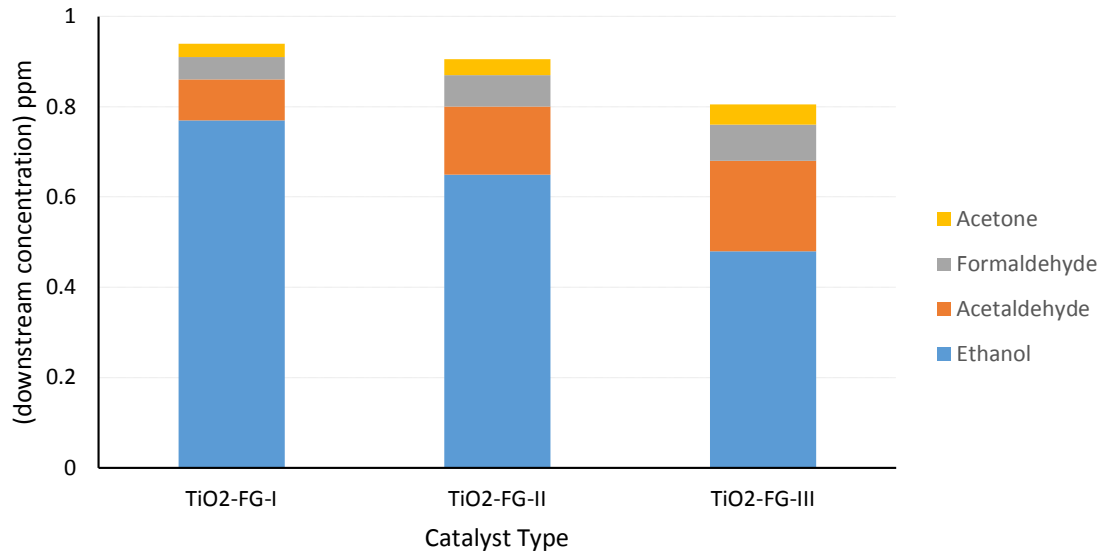
Figure 4-3. Comparison of byproduct concentration between tested PCO systems (35-40%RH, 25W/m^2)

In case of VUV lamps, the complete and partial oxidation rate of ethanol were increased for all tests. It seems that the increase of hydroxyl radicals (which was due to the ozone presence) promoted the intermediates and byproducts formations. Besides, the tested catalysts with low surface area of about 10 m^2/g or even 90 m^2/g did not have enough adsorption capacity and sufficient active sites to handle the complete oxidation reaction of ppm level concentration. Therefore, the reaction rate of the above byproducts were directly related to the particular intermediary reactions with slower reaction rate, which needed more time to have a complete mineralization. This means that it needs more surface area to supply the required active sites to maintain the oxidation rates without a buildup of reaction intermediates.

The increase of water vapor, higher humidity, limited the access of ethanol to active sites on the catalyst surface. This behavior could be explained with the photo-induced hydrophilicity of titanium dioxide nature [80]. Figure 4-4 shows the adsorption behavior of ethanol with water vapor molecules on the catalyst surface. The increase of water vapor molecules decreases the adsorption of ethanol molecules and consequently the ethanol's PCO reaction rate.
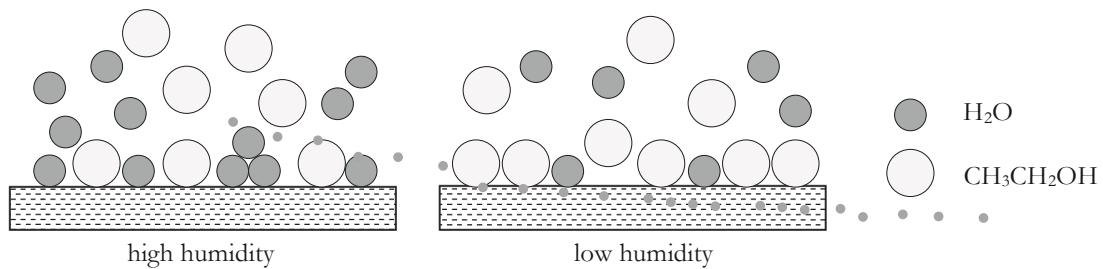
Figure 4-4. Adsorption behavior of ethanol and water vapor on TiO_2 surface
at different humidity levels

The size of ethanol molecule plays an important role on the adsorption rate of molecule. Ethanol molecule size is much larger than H_2O, where the H_2O molecule size is equivalent to OH group in ethanol. The competition of water molecules may not merely be limited to ethanol, as the adsorption of acetaldehyde could happen on the same active surface sites (*Piera et al.*, 2002). Figure 4-5 shows the conversion rate of ethanol at different humidity levels.
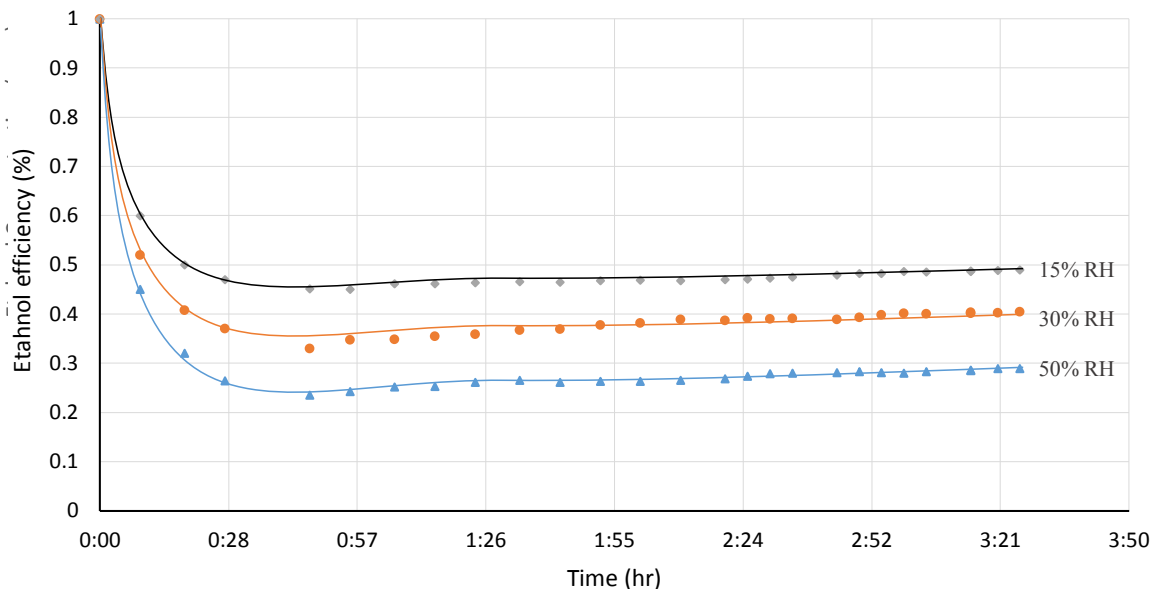
Figure 4-5. Conversion rate of 1-ppm ethanol at different humidity levels (15,30,50%RH), FG-III

It was observed that the efficiency of all catalysts were decreased at higher humidity levels throughout the experiment period. The adsorption of water and competition of water with ethanol molecules over the same active sites were become greater in higher humidity levels. This phenomenon also could be interpreted as the reaction of water

molecules with intermediate species on the TiO_2 surface structure [47]. It was believed that the creation of a strong bond with these secondary compounds could reduce the number of available active sites on the catalyst surface. In parallel, the affinity of photo generated holes to adsorb water molecules may also act as an inhibitor for the complete photocatalytic degradation of ethanol [81].

The results showed that the ozone could improve the removal efficiency of UV-PCO for ethanol. However, the generation of more intermediates such as acetic acid and formic acid was observed in all the ozone tests. An increase of gas-phase acetaldehyde and formaldehyde formation was found in lower humidity levels. Figure 4-6 compares the production rate of ethanol byproduct at different concentration levels. The formic acid and acetic acid were obtained from different sampling methods, where the catalyst was washed and filtered with pure methanol and then 0.1-µL sample was analyzed with GC/MS*. *Hwang et. al.* (1999) found the similar intermediate reactions with the *13C cross-polarization with magic angle spinning* (CP/MAS-NMR) experiments[7]. The CP/MAS experiment commonly has been used to study the photocatalytic reactivity of surface-bound species.
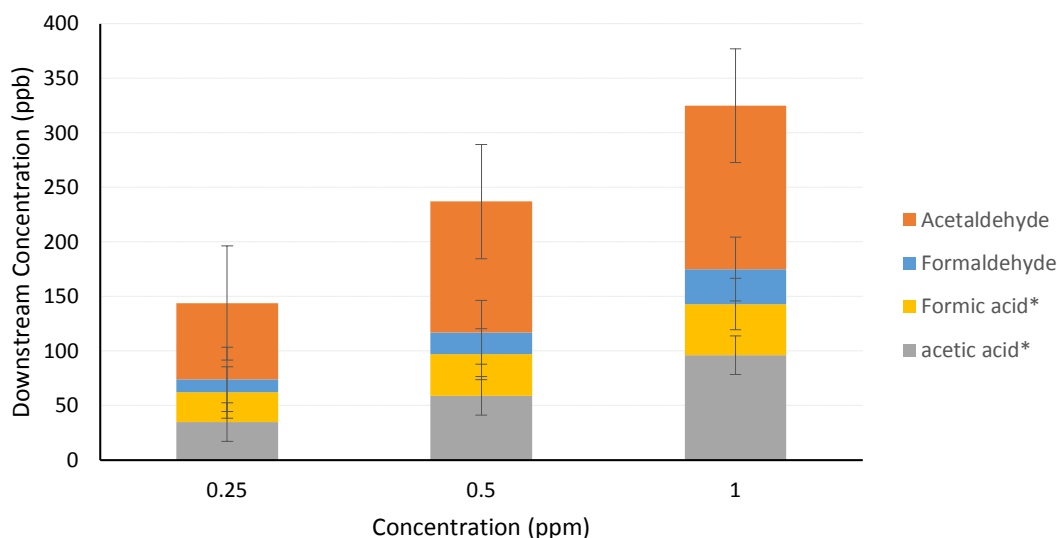
Figure 4-6. Comparison of byproduct generation rate by ethanol at different concentrations (TiO₂-FG-III)

[7] *S.-J. Hwang and D. Raftery*, "In situ solid-state NMR studies of ethanol photocatalysis: characterization of surface sites and their reactivities," Catalysis Today, vol. 49, pp. 353-361, 1999.
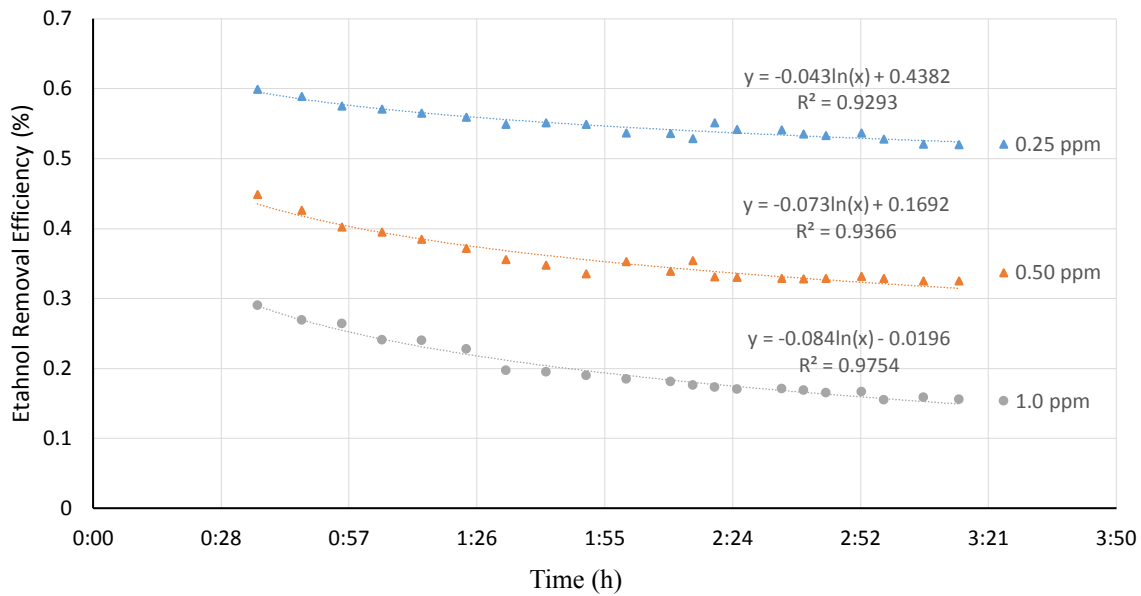
Fig 4-7. Comparison of ethanol removal efficiency at three different concentrations (TiO$_2$-FG-II)

Figure 4-7 shows the removal efficiency of ethanol at different concentrations at 40% ($\pm$10) RH. It was assumed that the adsorption of ethanol follows a monolayer adsorption on the catalyst surface. It was also assumed that all the adsorption sites are equivalent, which means all competing adsorbents have equal access to all adsorption sites. The rate expressions were determined for each individual VOC with adsorption tests with different initial concentrations.

The correlation between $k_{PCO}.K$ vs. IP and k_{PCO} vs. IP is presented in Figures 4-8 to 4-13. The PCO reaction rates were determined from curve fitting of experimental data with L-H kinetic model (section 2.5.1). It was found that the unimolecular L-H model well describes the destruction rate of ethanol under tested relative humidity concentration. The linear results suggest that the majority of surface PCO reactions follow the L-H model and the amount of gas-phase reaction is negligible. The adsorption constant (K) was obtained from isotherm experiments for each catalyst as described in section 3-10. The IP values is available in Appendix 1. The presented model provided a good approximation for the PCO reaction kinetics. The rate constants were reported for tested concentration between 0.25-1.0 ppm. All the results in Tables 4-2, 4-3 and 4-4 were at similar relative humidity of 20~25% ($\pm$5) and temperature of 21ºC ($\pm$0.5).

Table 4-2. L-H rate constant for tested alcohol group, TiO$_2$-FG-I (21°C, 25±5 %RH)

VOC	Concentration (ppm)	k_{PCO} (mg/m^3.s^{-1})	$K \times 10^{-4}$ (m^3/mg)	$k_{PCO}.K \times 10^{-4}$ (s^{-1})	R^2
Ethanol	0.25-1.0	2.94	0.32	0.94 (±1.36)	0.999
n-propanol	0.25-1.0	3.43	0.82	2.81 (±1.12)	0.991
1-butanol	0.25-1.0	2.73	0.83	2.27 (±1.54)	0.995
2-butanol	0.25-1.0	3.96	1.01	3.99 (±1.03)	0.991
3-pentanol	0.25-1.0	4.58	1.22	5.59 (±1.55)	0.994
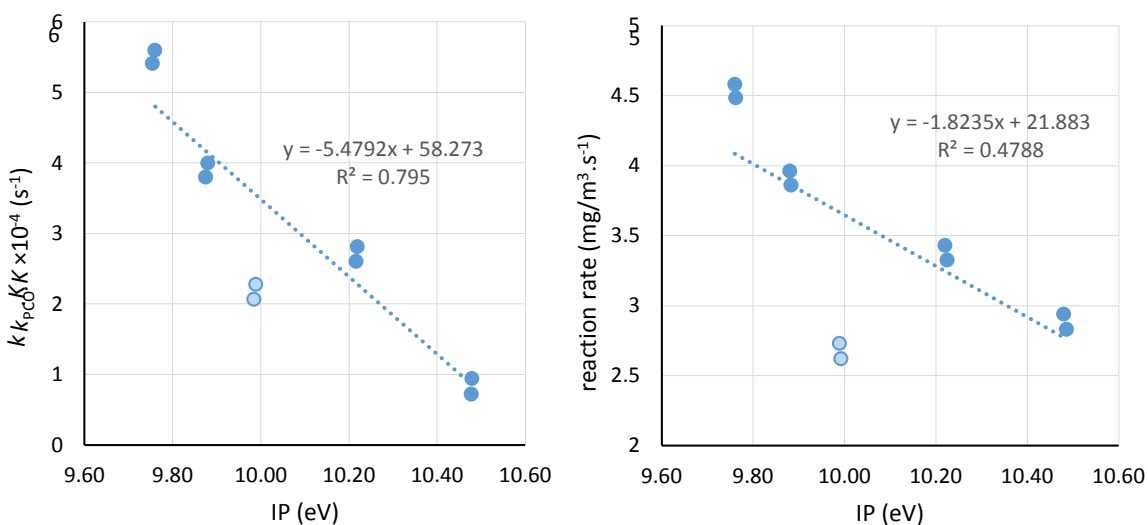
Figure 4-8. Rate constant of light alcohols vs. IP for alcohols (TiO$_2$-FG-I)
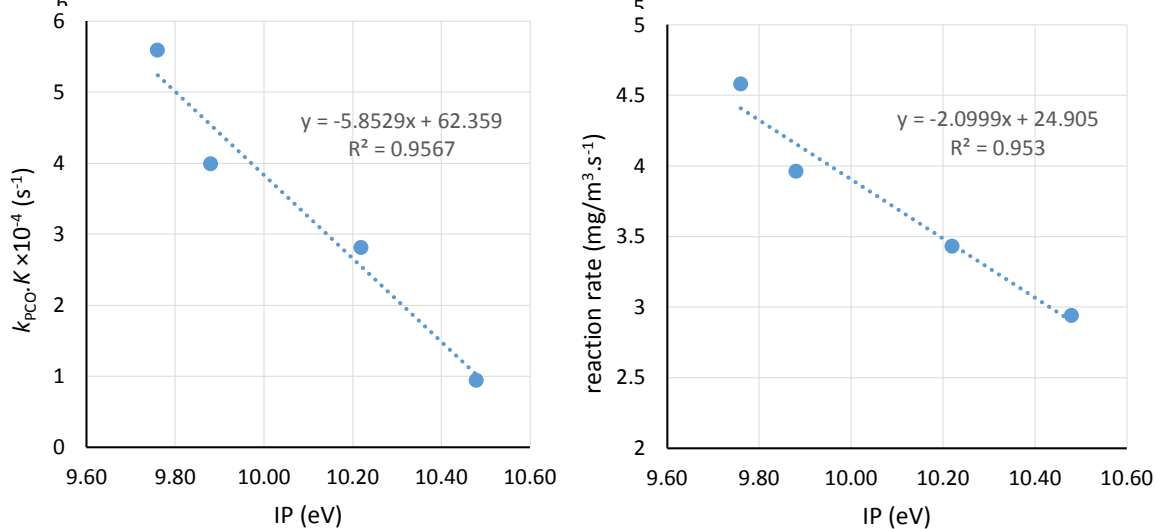
Figure 4-9. Rate constant of light alcohols vs. IP for alcohols, w/o 1-butanol (TiO$_2$-FG-I)

Table 4-3. L-H rate constant for tested alcohol group, TiO₂-FG-II (21°C, 22±5% RH)

VOC	Concentration (ppm)	k_{PCO} (mg/m³.s⁻¹)	$K \times 10^{-4}$ (m³/mg)	$k_{PCO}K \times 10^{-4}$ (s⁻¹)	R^2
Ethanol	0.25-1.0	2.38	0.64	1.52 (±1.01)	0.976
n-propanol	0.25-1.0	2.75	0.73	2.01 (±0.82)	0.979
1-butanol	0.25-1.0	2.68	0.89	2.39 (±0.79)	0.991
2-butanol	0.25-1.0	4.03	0.97	3.91 (±0.91)	0.981
3-pentanol	0.25-1.0	4.87	1.09	5.31 (±0.45)	0.992

Figure 4-10. Rate constant of light alcohols vs. IP for alcohols (TiO₂-FG-II)
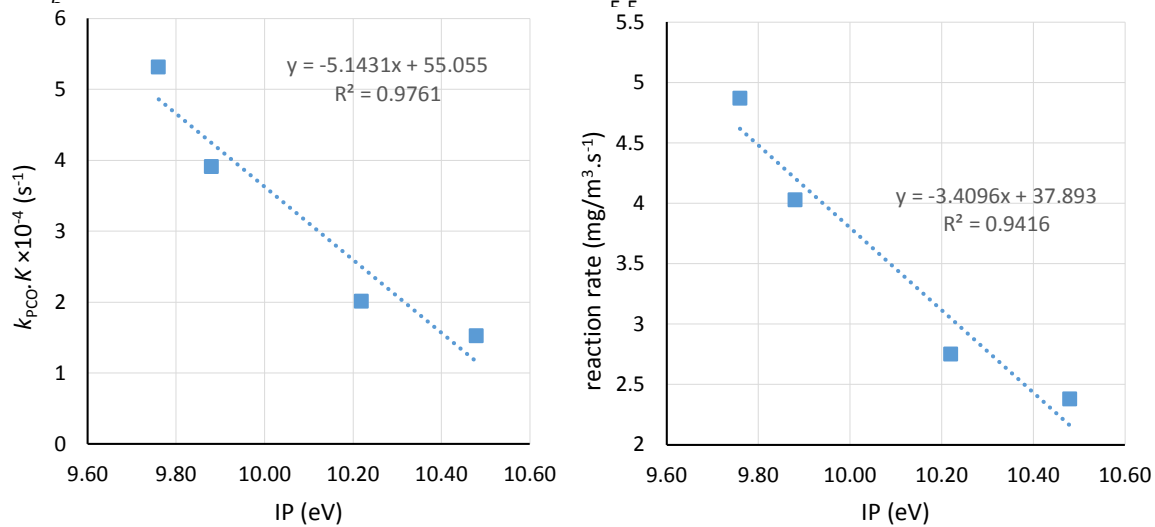
Figure 4-11. Rate constant of light alcohols vs. IP for alcohols, w/o 1-butanol (TiO₂-FG-II)

Table 4-4. L-H rate constant for tested alcohol group, TiO₂-FG-III (21°C, 20±5% RH)

| VOC	Concentration (ppm)	k_{PCO} (mg/m³.s⁻¹)	$K \times 10^{-4}$ (m³/mg)	$k_{PCO}.K \times 10^{-4}$ (s⁻¹)	R^2
ethanol	0.25-1.0	1.89	0.31	0.59 (±0.92)	0.993
n-propanol	0.25-1.0	2.25	0.42	0.95 (±0.68)	0.968
1-butanol	0.25-1.0	1.97	0.37	0.73 (±1.04)	0.979
2-butanol	0.25-1.0	2.92	0.65	1.90 (±0.98)	0.929
3-pentanol	0.25-1.0	3.15	0.83	2.61 (±0.91)	0.989

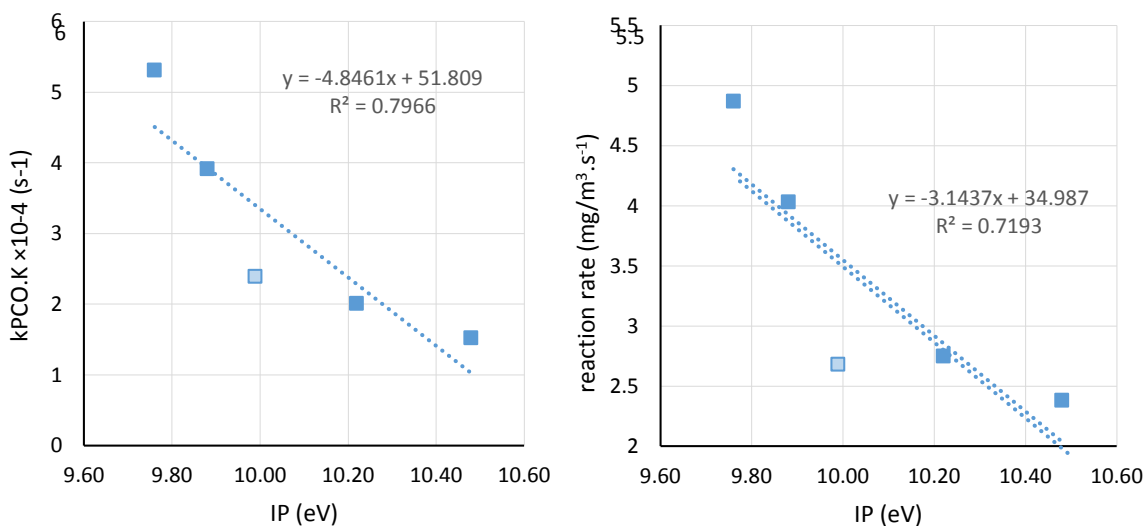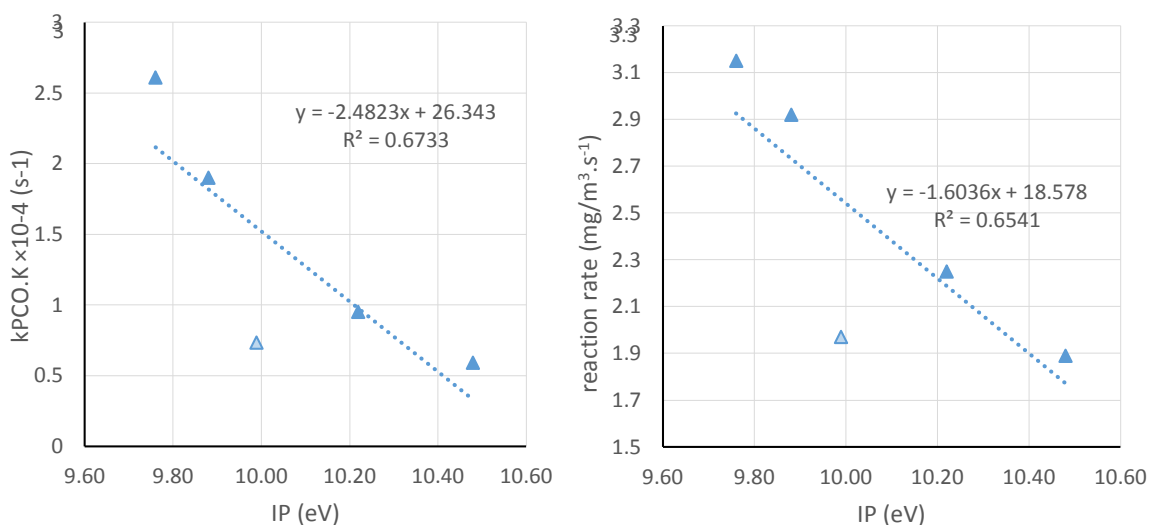Figure 4-12. Rate constant of light alcohols vs. IP for alcohols (TiO₂-FG-III)
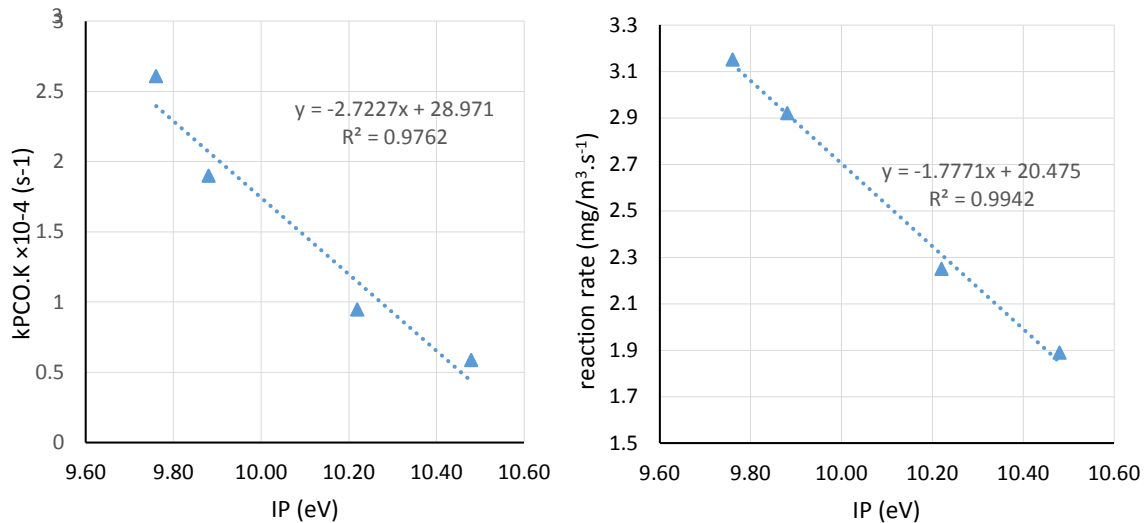
Figure 4-13. Rate constant of light alcohols vs. IP for alcohols, w/o 1-butanol (TiO₂-FG-III)

The relatively slow PCO reaction rate of 1-butanol compare to 2-butanol created a deviation from linear correlation between $k.K$ and IP (Figure 4-8, 10, 12). This behavior of 1-butanol could be considered as a partial oxidation of 1-butanol to acids and further occupation of active sites with generated acidic intermediates. This reaction process commonly associated to the primary alcohols photocatalytic oxidation mechanism. The suggested mechanisms of ethanol is described in Figure 4-14.

At higher humidity levels, the adsorption constant (K) was decreased as the competition rate between water and ethanol molecules increased. A decline in ethanol adsorption resulted and consequently the ethanol reaction rates were decreased on the catalyst surface. *Miyauchi et al.* (2000) investigated the relationship of hydrophilicity of TiO_2 and the number of OH groups with FTIR spectrometry experiments. They observed that the amount of chemisorbed OH groups is associated with both dissociated water and physically adsorbed water molecules on the catalyst surface [82]. The formation of metastable OH groups at higher humidity levels gradually decreases the number of available active sites on the catalyst surface [80].

The results with VUV lamps showed that the generation of significant amount of ozone in range of 700 to 2000 ppb concentration would increase the oxidation rate of ethanol by 5-10%. Meanwhile, the concentration of some byproducts such as acetaldehyde was increased at the same time. The relative humidity had direct effect on the deposition of ozone concentration inside the system. It seems that the hydrophobic surfaces such as titanium dioxide have higher ozone adsorption rate at higher humidity levels (*Weschler*, 2000). However, the reaction rate of ozone with adsorbed VOCs is very slow and it has negligible effect on the surface reactions.

The experiments with ethanol showed that acetaldehyde and formaldehyde are the primary concerning byproducts of the PCO. The key reactions can be described as following:

1. The absorption of ethanol on the catalyst surface follows monolayer L-H rate form. In higher concentrations, the rate of competition with produced intermediates decreases the absorption, where they completely cover the catalyst surface afterwards.

2. The photocatalytic oxidation of the absorbed ethanol undergoes to the production of acetaldehyde as primary intermediate where the quality of the secondary reactions completely depends on the irradiation intensity, loading of TiO_2 and type of substrate. Afterwards, it has been shown that the acetaldehyde PCO reaction pathways could be divided into three parallel reactions where they lead to secondary intermediates such as: formaldehyde, acetic acid, formic acid and carbon dioxide [81]. The degradation of acetic and formic acid usually happens instantly and it could not be an inhibiting stage for incomplete reactions. However, the accumulation of acids production in shaded regions through the catalyst (dark spots) could be problematic in low illuminated catalysts [83]. The surface reactions between intermediates could be relatively timely under low intense UV illumination. For example, formaldehyde reaction produces formic acid where it could finally yield carbon dioxide. Furthermore, acetaldehyde reaction with formaldehyde and carbon dioxide could produce acetic acid which eventually ends to carbon dioxide. It seems that the rapid formation and accumulation of acetaldehyde as primary surface intermediate is the main reason that leads to fast release of acetaldehyde to the gas phase [84]. This problem could be improved by using suitable substrate with high adsorption affinity to adsorb such intermediates like acetaldehyde and formaldehyde.

3. The detailed reaction pathway of the ethanol is summarized in Figure 4-14:
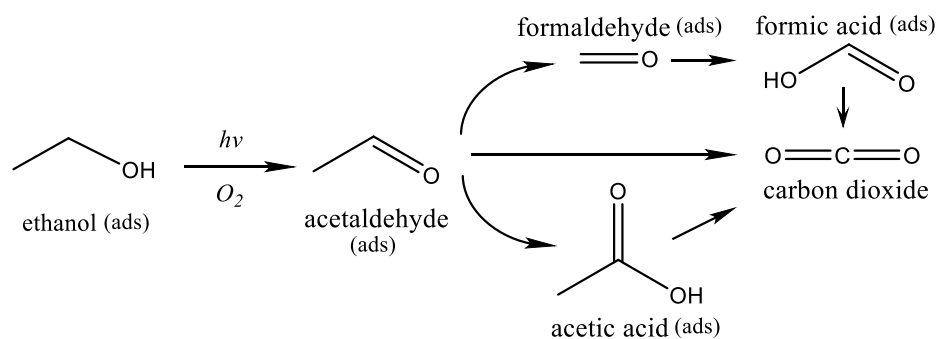
Figure 4-14. Ethanol photocatalytic reaction pathway on the titanium dioxide catalyst

4. The selectivity of formaldehyde PCO reactions into formic acid (HCOOH) was 20 percent of the total concentration of formaldehyde. It has been shown that the oxidation rate of formaldehyde is dependent on the availability of water vapor molecules and photo generated holes ($h+$) on the catalyst surface [85]. The reported byproduct conversion ratio of formaldehyde by other work (*Noguchi et al.* 1998) was divided into 80% CO_2 and 20% HCOOH, which was similar to the byproducts generation ratio for ethanol.

5. It has been shown that the water displaces the weakly absorbed ethanol molecules at higher humidity levels. The occupation of water molecules along adsorption decreases the active surface sites and adsorption of ethanol molecules. The strong adsorption of water molecules and slow desorption along some intermediates such as formaldehyde could be an inhibiting factor to complete photocatalytic reactions [84].

6. The GC/MS analysis of ethanol with TiO_2 showed only acetaldehyde as main byproduct. Moreover, The HPLC results suggested that the generated intermediates such as formic and acetic acid create strong bond with titanium dioxide structure and they could not easily desorb from catalyst surface. The quantitative analysis also showed that a small amount of formaldehyde was observed as byproduct. This behavior suggested that the strong attachment of acidic intermediates on the catalyst surface was the secondary reason for relatively fast deactivation of catalyst with ethanol and other tested alcohols experiments.

Earlier work showed that the reaction rate of ethanol could follow a general single layer L-H rate, similar to following equation in humid conditions [10]:

$$r_{\text{ethanol}} = -\frac{dC_e}{dt} = \frac{k_e K_e C_e}{1 + K_e C_e + K_a C_a + K_f C_f} \qquad (4-1)$$

where r_{ethanol} is the reaction rate of ethanol; k is the reaction rate constant; K is the absorption equilibrium constant; C is the concentration and e, a and f subscripts denotes to ethanol, acetaldehyde and formaldehyde compounds respectively.

4.1.2. 2-propanol (C_3H_8O)

2-propanol is selected as a second representative of VOCs from alcohol class. It is the one of the most common alcohol that can be found in residential and industrial indoor environment. 2-propanol is usually used as solvent ingredient in the household cleaning and personal care product. It is relatively non toxic and usually used in disinfecting and hand sanitizer products. The exposure limit for this alcohol is 400 ppm TWA (*Québec OH&S*). This section examined the photocatalytic removal efficiency, photochemical reaction mechanisms and produced byproducts of 2-propanol.

The experiments with 2-propanol have shown that acetone was the primary byproduct of the PCO reactions. The PCO reactions could be described as following steps:

(1) The absorption of 2-propanol on the TiO_2 could take place in two forms of hydrogen bounded physical and chemical absorption. The absorption of 2-propanol may reach to a constant amount after reaching a monolayer coverage, because the chemical absorption is a function of the available surface area. With increasing the concentration, the rate of physisorption absorption is increased afterwards. It has been shown that the different behavior in absorption of the primary and secondary alcohols on the surface of the catalyst is due to the *steric effect* which depends on the size of absorbent molecule [86].

(2) The PCO reactions of the absorbed 2-propanol undergoes to the production of gas-phase acetone and CO_2 where they could be absorbed strongly on the surface. The *solid state NMR* (SSNMR) studies showed that the complete reaction of the weakly absorbed acetone needed a longer time due to the weak bonds [86].

(3) By increasing the UV irradiation, the concentration of the acetone would increase afterwards. It was observed that it was due to the relation of light intensity and presence of the dark spots on the catalyst surface. The absorbed 2-propanol species could have effective reactions in dark areas. Hence, the acetone formation was not observed in dark regions.

(4) The primary reaction pathway of 2-propanol is summarized here:
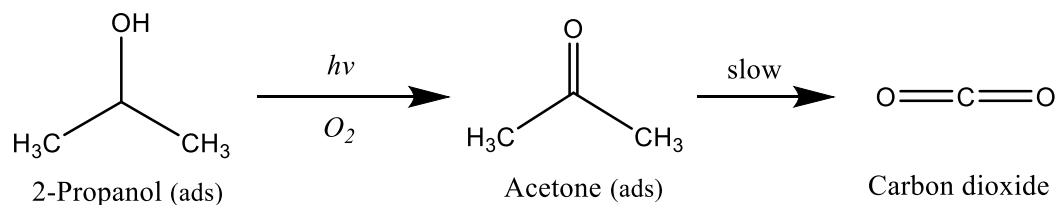
The GC-MS analysis of 2-propanol with TiO$_2$ confirmed the above proposed photooxidation mechanism which shows the absorbed 2-propanol could rapidly be degraded into acetone under UV illumination as primary partial intermediate. The produced acetone occupies the surface sites and it also may compete with other 2-propanol molecules which may inhibit further absorptions on the catalyst surface.
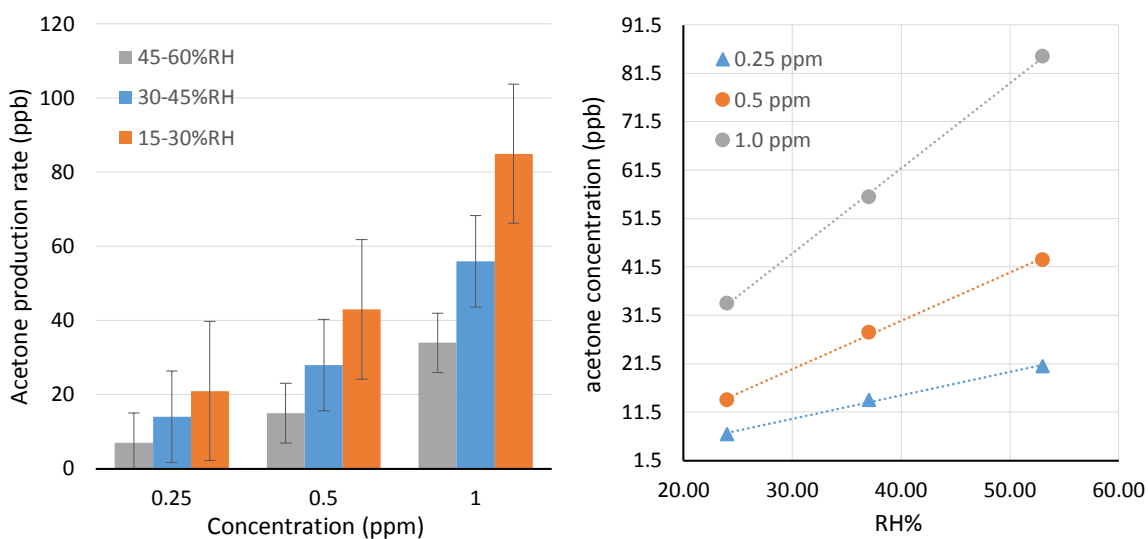
Figure 4-15. Acetone as byproduct of 2-propanol at different concentrations

Xu et al. [86] described the conversion rate of acetone into carbon dioxide as a very slow reaction which was not comparable with production rate of acetone. The secondary reaction mechanism suggests that the absorbed 2-propanol transform to 2-propoxide and under UV irradiation could degrade to carbon dioxide with higher rate in comparison to 2-propanol reaction rate.

2-Propanol (ads)   2-Propoxide (ads)   Carbon dioxide
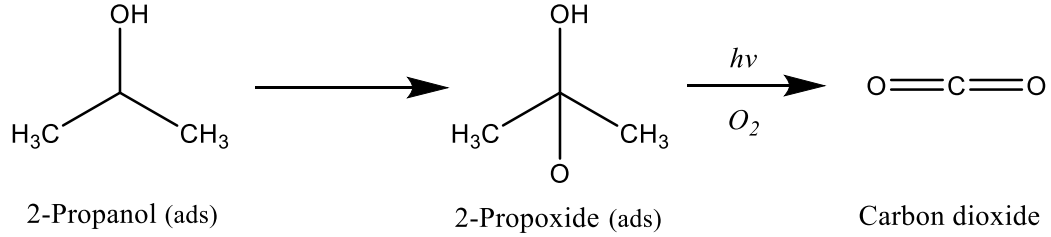
The reaction rate of 2-propanol generally follows the general single layer Langmuir-Hinshelwood rate (eq. 4-2). This kinetic model also was mentioned by others at different experimental conditions [87]:

$$r_{2\text{-propanol}} = -\frac{dC_p}{dt} = \frac{k_p K_P C_p}{1 + K_P C_p + K_a C_a} \qquad (4-2)$$

where $r_{2\text{-propanol}}$ is the reaction rate of 2-propanol; k is the reaction rate constant; K is the absorption equilibrium constant; C is the concentration and p and a subscripts respectively denotes 2-propanol and acetone compounds. For the acetone, the similar competitive L-H expression could be obtained as the following rate equation:

$$r_{acetone} = \frac{dC_a}{dt} = \frac{k_p K_P C_p - k_a K_a C_a}{1 + K_P C_p + K_a C_a} \qquad (4-3)$$

A plot of initial reaction rate versus initial concentration of 2-propanol could represent the reaction rate and absorption equilibrium values. Furthermore, Langmuir isotherm may be used to determine the surface coverage of 2-propanol:

$$\Theta = \frac{C_{ads}}{C_{max}} = \frac{KC_{eq}}{1 + KC_{eq}} \qquad (4-4)$$

where Θ is the surface coverage of 2-propanol; C_{ads} is the surface concentration; C_{max} is the maximum surface concentration; C_{eq} is the equilibrium concentration in gas phase and K is the adsorption constant.

An higher humidity level, it is necessary to account for the presence of water vapor as another challenging compound for surface sites. They could easily be displaced by weakly absorbed acetone and then they become a tough competitor with 2-propanol

species over the remaining surface sites [88]. The competitive behavior of 2-propanol reaction could be established by a similar L-H model.

The GC analysis showed that acetone was the exclusive byproduct of 2-propanol under UV illumination. This suggested that the slow reaction rate of acetone is the limiting step for 2-propanol photocatalytic reactions. Due to the fast formation of acetone and low conversion rate to carbon dioxide, the condition could be improved by increasing the number of UV lamps. Because of high mobility of chemisorbed 2-propanol, the reactants could migrate from dark areas to unoccupied active sites [86]. This matter may increase the photoactivity of 2-propanol and therefore the intensity of UV light becomes more effective in formation of acetone.
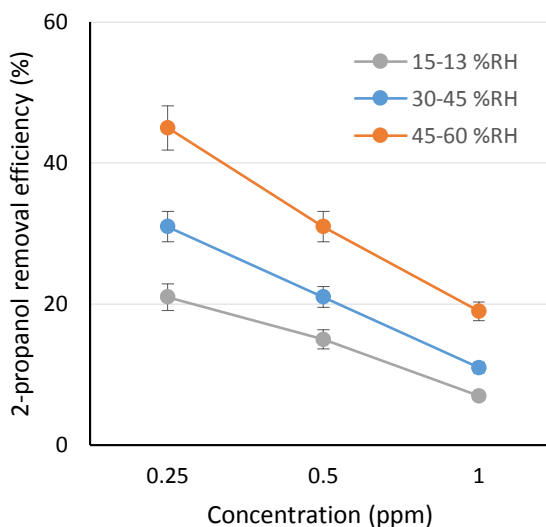
Figure 4-16. Removal efficiency% of 2-propanol at different humidity levels

Figure 4-16 shows the linear variation of 2-propanol removal efficiency as a function of different concentration and different humidity levels. The experiments for 2-propanol were selectively performed with TiO_2-FG-III catalyst. The reported percentage of acetone production rate was the median value of different experiments at the stated relative humidity range. The oxidation of 2-propanol to acetone as only gas-phase byproduct was confirmed by other works too [40]. It was found that the production rate of acetone has linear relationship with the relative humidity. It can be seen from Figure 4-16 that the changes of upstream concentration on oxidation of 2-propanol have a linear relationship

Table 4. Experimental design composition of fiber glass TiO$_2$ catalysts

Symbol	Substrate	Thickness um	TiO$_2$ (g.m^{-2})	Method
FG-I	FG-A	5	39.1	DC
FG-II	FG-B	10	26.2	DC+
FG-III	FG-B	2	12.5	SG

with humidity. These results suggest that oxidation rate of 2-propanol at low ppb level is not limited to the number of active sites under low humidity levels. Other experimental works using a *response surface methodology* (RSM) confirmed that the competition between byproducts adsorption and 2-propanol is not significant in low ppb level concentration [40]. They also confirmed that the effect of humidity from 0 to 60% could considerably decrease the oxidation rate of 2-propanol, where the generation rate of acetone similarly could be affected by presence of excess water vapor in the system.

In conclusion, it is believed that the presence of humidity was the main limiting factor for the oxidation of 2-propnaol to CO_2 as a favorable byproduct.

4.1.3. Butanol (C_3H_8O)

1-butanol and 2-butanol are two different isomers from VOCs alcohol class which have been selected for this study. Their different molecular structures permit to study the kinetic and intermediary surface photocatalytic oxidation reactions of two isomers beside each other. Butanol like other light alcohols (e.g. methanol and ethanol) usually used in fuels, perfumes and cosmetics and it is often used in textiles, paints and resins as solvent. The presence of this VOC is suspected in many indoor air environments. The exposure limit for this alcohol is 50 and 100 ppm for n-butanol and sec-butanol, respectively (NOISH). The odor threshold is between 0.2-30 ppm. In spite of that, the emitted byproducts from indoor air PCO systems like many other VOCs can be more problematic. This section examined the photocatalytic removal efficiency, photochemical reaction mechanisms and related possible byproducts of this VOC with nano TiO_2 catalyst.

The experiments with 1-butanol and sec-butanol have been shown that butanal and 2-butanone (MEK), respectively were the primary concerning byproducts of the PCO. These aldehyde intermediates were also identified by others [8, 89]. Considering the qualitative analysis, the kinetic pathways were described as following sequences:

1. The adsorption of 1-butanol on the catalyst surface could instantly be oxidized with available superoxide and hydroxyl radicals, which leads to the formation of butanal as an intermediate with the following pathway:
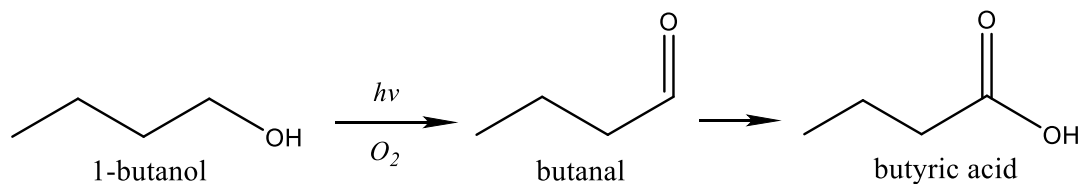
Figure 4-17. Photocatalytic reaction pathway of 1-butanol

2. The fast formation of butanal may lead to the accumulation on the catalyst surface and then evolution to gas phase. Thereafter, the partial mineralization of adsorbed butanal to butyric acid, which could result to several secondary intermediates reactions such as acetaldehyde, acetic acid, formaldehyde and formic acid. Depending on the adsorption affinity of these intermediately compounds, they may remain on the catalyst surface and degrade slowly to carbon dioxide and water. The details of these reaction pathways are described in [89, 90].

The GC-MS results for 1-butanol suggested that the fast formation of butanal should be considered as the key species that its photocatalytic reactions should be studied furthermore. The main issue with complete oxidation of butanal similarly could be associated to the slow PCO reaction rates of secondary reactions that usually happen on the catalyst surface. It means that these aldehyde intermediates need more contact time to have a complete degradation.

In summary, the primary reactions that start the PCO reactions are produced electron-holes and O_2 molecules. The absorbed oxygen reacts with generated electrons that results in superoxide anion (eq. 2-11, 2-15). The oxidation of absorbed VOCs on the catalyst surface could be started by reaction with the generated holes (h^+) produces protons (H^+). These protons (H^+) can react with superoxides, which produces perhydroxyl radicals, $HO_2 \bullet$ (eq. 2-13).

On the other hand, the adsorbed water vapor also oxidized by holes (h^+) which produce hydroxyl radicals ($OH^{\bullet}$) (eq. 2-8). The oxidation of primary alcohols such as 1-butanol with these radical species leads to ketone intermediate formation:
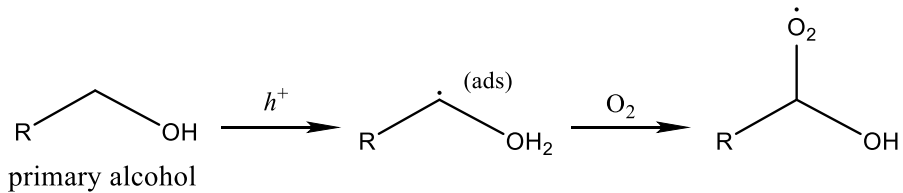
Figure 4-18. Initial reaction pathway of primary alcohol

In case of 1-butanol, the above intermediate reacts with perhydroxyl radicals which transforms to butanal. The presence of sufficient water vapor plays an important role to generation of the required hydroxyl radicals in the above described reactions.

2-butanol as a secondary alcohol follows different reaction pattern. The primary adsorption of oxygen molecules and water vapor on the catalyst surface are similar to the other alcohols. The adsorption of 2-butanol with central carbon can react with other adsorbed O_2^- and bulk O_2 gas in the air.

The dehydrogenation of adsorbed 2-butanol leads to the formation of weakly adsorbed surface complexes where they finally degraded into ketones such as 2-butanone (MEK) as primary byproduct. Less acetaldehyde was also identified as secondary product. The same pathway has been reported by previous work for 2-propanol as secondary alcohol [91].

The surface adsorption of butanol required higher energy that inhibits the water vapor displacement. Hence, the water vapor adsorption competition at the higher relative humidity level is not considerable [8].

Langmuir-Hinshelwood model can be applied for butanol reaction rate as:

$$r_{butanol} = -\frac{dC_b}{dt} = \frac{k_b K_b C_b}{1 + K_b C_b} \qquad (4-5)$$

where $r_{butanol}$ is the reaction rate of butanol; k is the reaction rate constant; K is the absorption equilibrium constant; C is the concentration and b subscripts denotes to butanol compound.

4.1.4. 3-Pentanol ($C_5H_{12}O$)

3-pentanol was selected as a model VOC for secondary alcohols class. It has similar molecular structure to 2-butanol. 3-pentanol commonly used in paints, adhesives and degreasers. The toxic effect of this compound is not clearly known, the maximum allowable exposure concentration was considered 20 ppm and it has been classified as *central nervous system* (CNS) solvent syndrome agent[8]. This section examined the photocatalytic removal efficiency, photochemical reaction mechanisms and produced byproducts of 3-pentanol PCO reaction.

The GC/MS quantification analysis showed that 3-pentanone, acetaldehyde and propanal (with order of highest to the lowest concentration ratio) are the primary byproducts of 3-pentanol reactions. The kinetic pathways could be described as following sequences:

1. The adsorption of 3-pentanol was somehow similar to 2-butanol. The localization of produced holes (h^+) with adsorbed 3-pentanol could promote its oxidation rate under UV irradiation as following pathway:
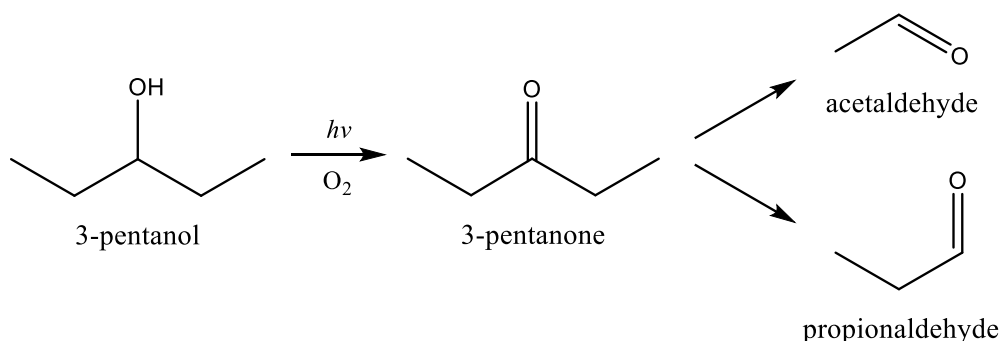
Figure 4-19. The reaction mechanism of 3-pentanol with TiO_2 catalyst

2. The rapid formation of 3-pentanone on the catalyst surface promotes the evolution of accumulated adsorbed molecules into gas phase as byproduct. The remained adsorbed 3-pentanone may degrade into secondary intermediates such as: acetaldehyde and propionaldehyde. The propionaldehyde is structurally an isomer of acetone and similarly it could slowly degrade into carbon dioxide. The acetaldehyde could break down into formaldehyde, acetic acid and carbon dioxide. The weak adsorption bonds

---

[8] Haz-Map database, National Library of Medicine

of the aldehyde intermediary compounds along slow reaction rates promote further partial desorption into the gas phase.

3. The decrease of removal efficiency for 3-pentanol at higher concentration suggested that the dehydration of 3-pentanol after surface adsorption and its rapid accumulation on the catalyst surface could reach to a saturated level at near ppm level concentration.

4. The reaction rate of 3-pentanol follows the general single layer Langmuir-Hinshelwood rate:

$$r_{3\text{-pentanol}} = -\frac{dC_p}{dt} = \frac{k_1 K_1 C_1}{1 + K_1 C_1 + K_2 C_2} \qquad (4-6)$$

where $r_{3\text{-pentanol}}$ is the reaction rate of 3-pentanol; k is the reaction rate constant; K is the absorption equilibrium constant; C is the concentration and 1 and 2 subscripts denotes to 3-pentanol and 3-pentanone compounds respectively.

4.1.5. Alkanes

In this section, the photocatalysis of selected light alkanes group was investigated with different PCO systems. The light alkanes with a stable and inert molecular structure could be good candidate to be challenged with new developed TiO_2 catalysts. The primary challenge for complete oxidation of light alkanes goes back to the difficulty to breakdown of C−C and C−H bonds in current heterogeneous PCO air cleaners [92]. The low absorptivity was the second reason that inhibited the oxidation rate of alkane compounds.
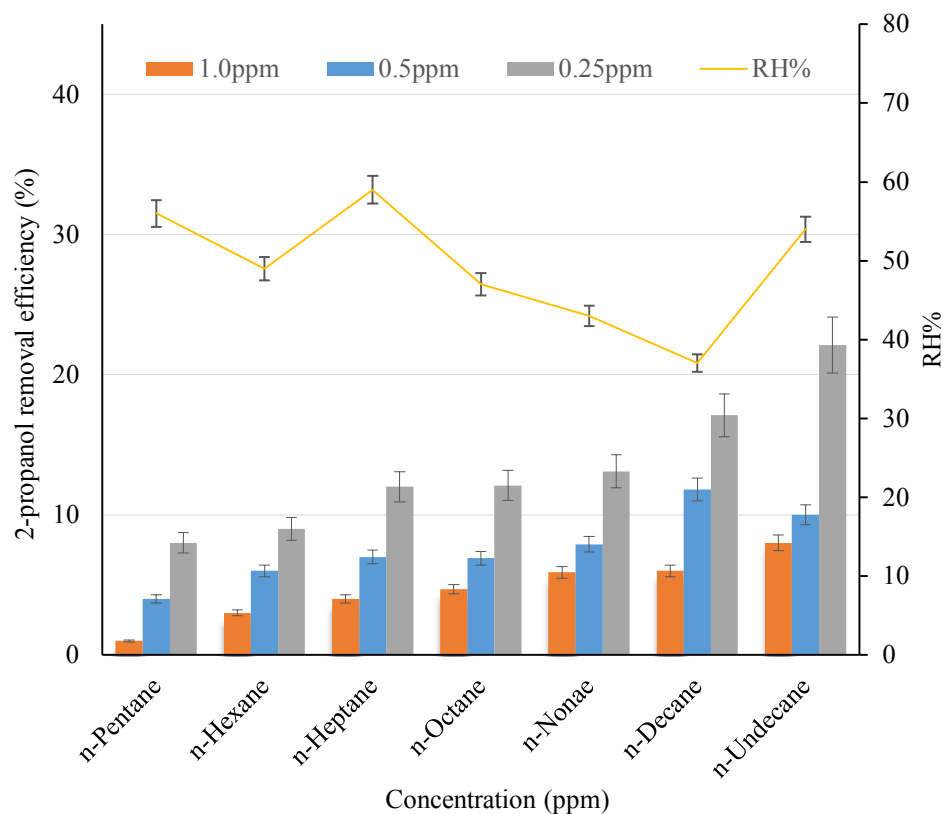
Figure 4-20. Effect of concentration on efficiency of alkanes class (21(±1)ºC, 35~60% RH), TiO$_2$-FG-III

The efficiency of the newly developed TiO$_2$ catalyst was evaluated with light alkane compounds. The synthesized TiO$_2$-FG-III catalyst with sol-gel method had a mesoporous TiO$_2$ film with higher specific area (compare to TiO$_2$-FG-II), which was showed higher efficiency compare to commercial P25 TiO$_2$ catalyst with dip-coated procedure in average humidity levels. The effect of photolysis on the conversion rate of tested VOCs was evaluated by several blank tests. The blank experiments were carried out with only UV illumination and no photocatalyst was observed inside the system. There were no changes at the upstream and downstream concentration of all tested gases without any measurable gas-phase byproducts in the system.

Chapter V: Conclusions and Future Work

5.1. Summary

The evaluation of different UV-PCO air cleaner systems with the custom made pilot experimental system setup with four parallel ducts helped to compare the efficiency of several PCO catalysts at the same time with similar operational conditions to the real life application. The effect of different VOCs concentrations on the performance of UV-PCO systems were investigated under the most worst scenarios in indoor air environment. The experiments carried out under different relative humidity levels corresponding to different seasons throughout the year. The main conclusions may be summarized as follows:

(i) As an objective of this research, developed nano TiO_2 catalysts could improve the performance of UV-PCO systems with the tested VOCs compounds. The general removal efficiency comparison of tested catalysts was as following order: TiO_2-FG-I < TiO_2-FG-II < TiO_2-FG-III. The prepared catalyst by SG method (TiO_2-FG-III), demonstrated a higher oxidization efficiency compare to commercial TiO_2 catalysts under similar test condition. The suggested preparation technique for second catalysts (TiO_2-FG-II) could improve the immobilization of TiO_2 particle to fibrous substrate material, which showed a higher performance compare to TiO_2-FG-I.

(ii) It was found that the effect of ozone on oxidation of VOCs was insignificant at low ozone concentration levels (<700ppb). At higher level ozone concentration (1500-2000ppb), the ozone oxidation along PCO reactions could increase the overall performance of the tested PCO air cleaners. However, the removal efficiency of selected alcohols with unsaturated carbon-carbon bonds was higher than other stable VOCs such as alkanes. Meanwhile, it was observed that the concentration and the number of byproducts such as acetaldehyde and formaldehyde were increased at higher humidity levels. The reaction between ozone and VOCs could be explained by generation of more hydroxyl radicals in more humid conditions. The increase of more intermediates with particular groups such as hydroxyl (-OH), carbonyl (-C=O) and

carboxylate (-COOH), was observed in ozone UV-PCO systems. The most identified byproducts were more irritating compounds, such as formaldehyde, acetaldehyde and C_5-C_{10} aldehydes. In summary, the presence of ozone increased the concentration and number of byproducts in the systems while it could improve the oxidation rate of most tested VOCs under indoor air conditions.

(iii) The obtained results showed that the effect of water vapor on photocatalysis was completely depended on the molecular structure of VOC and adsorption rate of TiO_2 catalyst. At higher humidity levels, the adsorption of water molecules significantly reduced the PCO reactions rate of tested alcohols. The competition of water vapor on same active sites and strong adsorption affinity of generated byproducts, were limited to the PCO reactivity of alcohols. It seems that the hydroxyl group (−OH) in the alcohol molecules is the most important physical characteristic feature that makes the alcohols reactions differ from other tested VOCs. It has been shown that the acidity of alcohols in the gas phase is in the following order[9]: ethanol < n-propanol < n-butanol <n-pentanol [93]. The gas-phase acidity or proton affinity may be used to explain the alcohol behavior at different relative humidities. At high humidity, the affinity of alcohols to water molecules decrease the adsorption rate of alcohols on the catalyst surface, which also can be interpreted as the competition of water vapor with alcohols at the same active sites. The results showed that alcohols were oxidized into aldehydes and carboxylic acids, where the oxidation rate of secondary alcohols were higher than primary alcohols.

(iv) The effect of humidity on alkanes was different from alcohols with similar test conditions. The humidity on alkanes could slightly promote the oxidation rate and meanwhile it more increased the production rate of byproducts.

From this work, it also demonstrated that there is a direct relationship between physical and chemical properties of VOCs (such as IP) with PCO reaction rate. The proposed correlations for alcohols can be used to estimate the removal efficiency of tested PCO

---

[9] The reported acidity of alcohols was directly measured with *ion cyclotron resonance* (ICR) spectroscopy and *pulsed double-resonance* techniques [86].

catalysts for other smilier VOCs under comparable test conditions. However, a good relationship between isomers such as 1-butanol and 2-butanol could not be established with other tested alcohols. Because of the higher ionization energy value of 1-butanol compare to 2-butanol, (9.99 and 9.88 respectively), reduced the reaction rate (k_{PCO}) of 1-butanol. On the other hand, higher polarity of 1-butanol compare to 1-propanol, helped to have higher tendency to remain on the catalyst surface.

5.2. Future work

To optimize the photocatalytic reactions for indoor air application, it is necessary to decrease the possible byproduct generation from UV-PCO systems. This objective could be achieved by designing a suitable UV-PCO system with optimal catalyst. The reaction rate of VOCs strongly dependent on the adsorption rate and performance of catalysts to yield complete oxidation at different indoor air conditions. The versatility of nano titanium dioxide catalysts and theirs capacity to work under extreme experimental conditions has been proved by many previous studies. However, the photocatalyst properties could be improved to yield better oxidation rate for challenging VOCs compounds such as alkanes, which usually do not have satisfactory removal efficiency with available catalysts.

The improvement of intermediate reaction rate and byproduct reaction pathways needs to be focused in the future studies. The catalysts characteristics should be altered to control the reaction selectivity of reactions to more acids and less aldehydes. A suggested workaround for this matter could be employment of transition metals like *Ni*, *Ag*, *Cu*, *Au* or *Pt* with titanium dioxide. It has been shown that this metals could improve the photocatalytic reactivity of TiO_2 and alter the oxidation reaction with many VOCs to desired byproduct [18]. The transition metal ions could change the oxidation state of TiO_2 which helps to reduce the electron-hole recombination by forming a bond between reactant molecules and atoms of the surface catalyst. This effect leads to extending reactant concentration on the catalyst surface and decreasing the activation energy of reactants molecules.

The nano particle TiO_2 catalyst should be designed to work with light aldehydes and ketones which are the common byproducts of VOCs. At this time, the efficiency of TiO_2 catalyst to degrade the light aldehyde and ketones is not significant for indoor air applications.

The future experiments need to be extended to study the effect of irradiation, surface area and humidity. The performance of PCO catalyst in long period experiments is not clearly known at this time. Moreover, the effect of different individual or mixture of VOCs at different low concentration needs to be further studied too.

Bibliography

[1]   "Residential Air Cleaners: A Summery of Available Information," United States Environmental Protection Agency (EPA)August 2009.

[2]   A. Hodgson and H. Levin, "Volatile organic compounds in indoor air: a review of concentrations measured in North America since 1990," 2003.

[3]   The National Air Pollution Surveillance (NAPS) program, Environment Canada [Online]. Available: http://www.ec.gc.ca/indicateurs-indicators/default.asp?lang=en&n=95E56B3E-1

[4]   National Pollutant Release Inventory: Air Pollutant Emissions Summaries and Trends. Environment Canada. [Online]. Available: http://www.ec.gc.ca/indicateurs-indicators/default.asp?lang=en&n=64B9E95D-1

[5]   L. Zhong, F. Haghighat, P. Blondeau, and J. Kozinski, "Modeling and physical interpretation of photocatalytic oxidation efficiency in indoor air applications," *Building and Environment,* vol. 45, pp. 2689-2697, 2010.

[6]   "Indoor air quality: organic pollutants. WHO Regional Office for Europe (EURO Reports and Studies No. 111)," World Health Organisation (WHO), Copenhagen1989.

[7]   J. Peral and D. F. Ollis, "TiO2 photocatalyst deactivation by gas-phase oxidation of heteroatom organics," *Journal of Molecular Catalysis a-Chemical,* vol. 115, pp. 347-354, Jan 29 1997.

[8]   J. Peral and D. F. Ollis, "Heterogeneous Photocatalytic Oxidation of Gas-Phase Organics for Air Purification - Acetone, 1-Butanol, Butyraldehyde, Formaldehyde, and Meta-Xylene Oxidation," *Journal of Catalysis,* vol. 136, pp. 554-565, Aug 1992.

[9]   O. d'Hennezel, P. Pichat, and D. F. Ollis, "Benzene and toluene gas-phase photocatalytic degradation over H_2O and HCL pretreated TiO_2: by-products and mechanisms," *Journal of Photochemistry and Photobiology a-Chemistry,* vol. 118, pp. 197-204, Nov 13 1998.

[10] M. L. Sauer and D. F. Ollis, "Photocatalyzed oxidation of ethanol and acetaldehyde in humidified air," *Journal of Catalysis,* vol. 158, pp. 570-582, Feb 1996.

[11] P. A. Kolinko and D. V. Kozlov, "Products distribution during the gas phase photocatalytic oxidation of ammonia over the various titania based photocatalysts," *Applied Catalysis B: Environmental,* vol. 90, pp. 126-131, 2009.

[12] I. Sopyan, "Kinetic analysis on photocatalytic degradation of gaseous acetaldehyde, ammonia and hydrogen sulfide on nanosized porous TiO2 films," *Science and Technology of Advanced Materials,* vol. 8, pp. 33-39.

[13] S. Devahasdin, C. Fan, K. Li, and D. H. Chen, "TiO2 photocatalytic oxidation of nitric oxide: transient behavior and reaction kinetics," *Journal of Photochemistry and Photobiology A: Chemistry,* vol. 156, pp. 161-170, 2003.

[14] J.-M. Herrmann, "Photocatalysis," in *Kirk-Othmer Encyclopedia of Chemical Technology*, ed: John Wiley & Sons, Inc., 2000.

[15] R. B. Bird, E. N. Lightfoot, and W. E. Stewart, *Transport phenomena*. New York; Toronto: Wiley, 2007.

[16] N. Serpone and E. Pelizzetti, *Photocatalysis: Fundamental and Applications*. New York: Wiley, 1989.

[17] B. C. Choi, L. H. Xu, H. T. Kim, and D. W. Bahnemann, "Photocatalytic Characteristics on Sintered Glass and Micro Reactor," *Journal of Industrial and Engineering Chemistry,* vol. 12, pp. 663-672, 2006.

[18] G. Ertl, H. Knözinger, and J. Weitkamp, *Handbook of Heterogeneous Catalysis*: Wiley-VCH Verlag GmbH, 2008.

[19] C. G. Vayenas, *Electrochemical activation of catalysis promotion, electrochemical promotion, and metal-support interactions*. New York: Kluwer Academic/Plenum Publishers, 2001.

[20] R. T. R. Krishna, *Multicomponent mass transfer*. New York; Chichester; Brisbane: J. Wiley and sons, 1993.

[21] H. W. Haynes, "The Experimental Evaluation of Catalyst Effective Diffusivity," *Catalysis Reviews,* vol. 30, pp. 563-627, 1988/12/01 1988.

[22] R. H. Perry and D. W. Green, *Perry's chemical engineers' handbook*. New York: McGraw-Hill, 2008.

[23] D. W. Chen, F. M. Li, and A. K. Ray, "Effect of mass transfer and catalyst layer thickness on photocatalytic reaction," *Aiche Journal,* vol. 46, pp. 1034-1045, May 2000.

[24] M. R. Hoffmann, S. T. Martin, W. Choi, and D. W. Bahnemann, "Environmental Applications of Semiconductor Photocatalysis," *Chemical Reviews,* vol. 95, pp. 69-96, 1995.

[25] J. S. Gaffney and S. Z. Levine, "Predicting Gas-Phase Organic-Molecule Reaction-Rates Using Linear Free-Energy Correlations .1. O(P-3) and Oh Addition and Abstraction Reactions," *International Journal of Chemical Kinetics,* vol. 11, pp. 1197-1209, 1979.

[26] D. Grosjean, "Atmospheric Chemistry of Toxic Contaminants .1. Reaction-Rates and Atmospheric Persistence," *Journal of the Air & Waste Management Association,* vol. 40, pp. 1397-1402, Oct 1990.

[27] M. L. Sattler and H. M. Liljestrand, "Method for predicting photocatalytic oxidation rates of organic compounds," *Journal of the Air & Waste Management Association,* vol. 53, pp. 3-12, Jan 2003.

[28] R. Atkinson, "Kinetics and mechanisms of the gas-phase reactions of the hydroxyl radical with organic compounds under atmospheric conditions," *Chemical Reviews,* vol. 86, pp. 69-201, 1986.

[29] K.-P. Yu, G. W. M. Lee, W.-M. Huang, C. Wu, and S. Yang, "The correlation between photocatalytic oxidation performance and chemical/physical properties of indoor volatile organic compounds," *Atmospheric Environment,* vol. 40, pp. 375-385, 2006.

[30] X. Fu, W. A. Zeltner, and M. A. Anderson, "Applications in photocatalytic purification of air," in *Studies in Surface Science and Catalysis*. vol. Volume 103, V. K. Prashant and M. Dan, Eds., ed: Elsevier, 1997, pp. 445-461.

[31] T. N. Obee and R. T. Brown, "TiO$_2$ Photocatalysis for Indoor Air Applications - Effects of Humidity and Trace Contaminant Levels on the Oxidation Rates of Formaldehyde, Toluene, and 1,3-Butadiene," *Environmental Science & Technology,* vol. 29, pp. 1223-1231, May 1995.

[32] R. Atkinson and W. P. L. Carter, "Kinetics and mechanisms of the gas-phase reactions of ozone with organic compounds under atmospheric conditions," *Chemical Reviews,* vol. 84, pp. 437-470, 1984.

[33] M. Lazzeri, A. Vittadini, and A. Selloni, "Structure and energetics of stoichiometric TiO2 anatase surfaces," *Physical Review B,* vol. 63, 2001.

[34] C. B. Almquist and P. Biswas, "Role of Synthesis Method and Particle Size of Nanostructured TiO2 on Its Photoactivity," *Journal of Catalysis,* vol. 212, pp. 145-156, 2002.

[35] J. Kehres, J. W. Andreasen, F. C. Krebs, A. M. Molenbroek, I. Chorkendorff, and T. Vegge, "Combined in situ small- and wide-angle X-ray scattering studies of TiO2 nanoparticle annealing to 1023 K," *Journal of Applied Crystallography,* vol. 43, pp. 1400-1408, 2010.

[36] A. Bhattacharyya, S. Kawi, and M. B. Ray, "Photocatalytic degradation of orange II by TiO_2 catalysts supported on adsorbents," *Catalysis Today,* vol. 98, pp. 431-439, 2004.

[37] D. T. Tompkins, B. J. Lawnicki, W. A. Zeltner, and M. A. Anderson, "Evaluation of photocatalysis for gas-phase air cleaning - Part 2: Economics and utilization," in *ASHRAE Transactions 2005, Vol 111, Pt 2.* vol. 111, M. Geshwiler, Ed., ed Atlanta: Amer Soc Heating, Refrigerating and Air-Conditioning Engs, 2005, pp. 85-95.

[38] J. Mo, Y. Zhang, and R. Yang, "Novel insight into VOC removal performance of photocatalytic oxidation reactors," *Indoor Air,* vol. 15, pp. 291-300, Aug 2005.

[39] M. M. Hossain, G. B. Raupp, S. O. Hay, and T. N. Obee, "Three-dimensional developing flow model for photocatalytic monolith reactors," *Aiche Journal,* vol. 45, pp. 1309-1321, 1999.

[40] D. Vildozo, C. Ferronato, M. Sleiman, and J.-M. Chovelon, "Photocatalytic treatment of indoor air: Optimization of 2-propanol removal using a response surface methodology (RSM)," *Applied Catalysis B: Environmental,* vol. 94, pp. 303-310, 2010.

[41] F. Shiraishi, Y. Ohbuchi, S. Yamaguchi, K. Yamada, H. Yamauchi, and H. Okano, "A Rapid Treatment of Indoor Formaldehyde at a Very Low Concentration in a Photocatalytic Reactor System Combined with a Continuous Adsorption and Desorption Technique," *Chemie Ingenieur Technik,* vol. 73, pp. 601-602, 2001.

[42] J. Zhao and X. Yang, "Photocatalytic oxidation for indoor air purification: a literature review," *Building and Environment,* vol. 38, pp. 645-654, 2003.

[43] J. S. Kim, K. Itoh, and M. Murabayashi, "Effects of pretreatment of TiO_2 thin films on the gas-phase photocatalytic reaction of trichloroethylene," *Denki Kagaku,* vol. 64, pp. 1200-1202, Nov 1996.

[44] M. E. Zorn, D. T. Tompkins, W. A. Zeltner, and M. A. Anderson, "Photocatalytic oxidation of acetone vapor on TiO_2/ZrO_2 thin films (vol 23, pg 1, 1999)," *Applied Catalysis B-Environmental,* vol. 25, pp. 69-69, Feb 21 2000.

[45] K. K. Takeuchi, S., "Removal of Chemical Substances from the Atmosphere by Photocatalysis," *Shigento Kankyo,* vol. 5, pp. 43-50, 1996.

[46] J. Mo, Y. Zhang, Q. Xu, J. J. Lamson, and R. Zhao, "Photocatalytic purification of volatile organic compounds in indoor air: A literature review," *Atmospheric Environment,* vol. 43, pp. 2229-2246, 2009.

[47] E. Piera, J. A. Ayllon, X. Domenech, and J. Peral, "TiO2 deactivation during gas-phase photocatalytic oxidation of ethanol," *Catalysis Today,* vol. 76, pp. 259-270, Nov 15 2002.

[48] ASHRAE, "Evaluation of Photo-catalytic Air Cleaning Capability," in *ASHRAE Research Project 1134-RP:,* ed: American Society of heating, Refrigrating and Air-Conditioning Engineers, Inc., 2001, p. 93.

[49] H. E. Khalifa, "Effect of nonuniform UV irradiation on photocatalytic air purifier performance," *ASHRAE Transactions 2005, Vol 111, Pt 2,* vol. 111, pp. 535-542, 2005.

[50] M. Singh, I. Salvadó-Estivill, and G. Li Puma, "Radiation field optimization in photocatalytic monolith reactors for air treatment," *Aiche Journal,* vol. 53, pp. 678-686, 2007.

[51] L.-M. Liu, P. Crawford, and P. Hu, "The interaction between adsorbed OH and O2 on TiO2 surfaces," *Progress in Surface Science,* vol. 84, pp. 155-176, 2009.

[52] N. Sakai, A. Fujishima, T. Watanabe, and K. Hashimoto, "Quantitative Evaluation of the Photoinduced Hydrophilic Conversion Properties of TiO_2 Thin Film Surfaces by the Reciprocal of Contact Angle," *The Journal of Physical Chemistry B,* vol. 107, pp. 1028-1035, 2003.

[53] X. Pan, M. Q. Yang, X. Fu, N. Zhang, and Y. J. Xu, "Defective TiO2 with oxygen vacancies: synthesis, properties and photocatalytic applications," *Nanoscale,* vol. 5, pp. 3601-14, May 7 2013.

[54] N. Quici, M. L. Vera, H. Choi, G. L. Puma, D. D. Dionysiou, M. I. Litter*, et al.*, "Effect of key parameters on the photocatalytic oxidation of toluene at low concentrations in air under 254+185 nm UV irradiation," *Applied Catalysis B-Environmental,* vol. 95, pp. 312-319, Apr 6 2010.

[55] H. Hippler, J. Troe, and H. J. Wendelken, "Uv Absorption-Spectra of Vibrationally Highly Excited Toluene Molecules," *Journal of Chemical Physics,* vol. 78, pp. 5351-5357, 1983.

[56] "U.S. Environmental Protection Agency, Code of Federal Regulations," 2010.

[57] "Health-related Evaluation Procedure for Volatile Organic Compounds Emissions (VOC and SVOC) from Building Products," *Committee for Health-related Evaluation of Building Products, AgBB,* May 2010.

[58] P. Wolkoff, P. A. Clausen, P. A. Nielsen, and L. Mølhave, "The Danish Twin Apartment Study; Part I: Formaldehyde and Long-Term VOC Measurements," *Indoor Air,* vol. 1, pp. 478-490, 1991.

[59] S. K. Brown, M. R. Sim, M. J. Abramson, and C. N. Gray, "Concentrations of Volatile Organic Compounds in Indoor Air - A Review," *Indoor Air,* vol. 4, pp. 123-134, 1994.

[60] V. M. Brown, D. R. Crump, and D. Gardiner, "Measurement of Volatile Organic-Compounds in Indoor Air by a Passive Technique," *Environmental Technology,* vol. 13, pp. 367-375, Apr 1992.

[61] K. R. Darnall, R. Atkinson, and J. N. Pitts, "Rate constants for the reaction of the hydroxyl radical with selected alkanes at 300 K," *The Journal of Physical Chemistry,* vol. 82, pp. 1581-1584, 1978.

[62] R. Atkinson and J. Arey, "Atmospheric degradation of volatile organic compounds," *Chem Rev,* vol. 103, pp. 4605-38, Dec 2003.

[63] S. Horikoshi, N. Watanabe, H. Onishi, H. Hidaka, and N. Serpone, "Photodecomposition of a nonylphenol polyethoxylate surfactant in a cylindrical photoreactor with TiO2 immobilized fiberglass cloth," *Applied Catalysis B: Environmental,* vol. 37, pp. 117-129, 2002.

[64] L. L. P. Lim, R. J. Lynch, and S. I. In, "Comparison of simple and economical photocatalyst immobilisation procedures," *Applied Catalysis A: General,* vol. 365, pp. 214-221, 8/31/ 2009.

[65] X. Chen and S. S. Mao, "Titanium dioxide nanomaterials: synthesis, properties, modifications, and applications," *Chem Rev,* vol. 107, pp. 2891-959, Jul 2007.

[66] C. J. Brinker and G. W. Scherer, *Sol-Gel Science: The Physics and Chemistry of Sol-Gel Processing*, 1 ed.: Academic Press, 1990.

[67] C. P. Sibu, "Sol-Gel Nanocrystalline Catalytic Titania Powders and Functional Coatings," Ph.D., Chemistry, 2004.

[68] B. Chiou, R.-Y. Yang, H.-J. Chuang, and C.-J. Chu, "Characterization of Nano-porous TiO2 Film Prepared by Sol-gel Process and Its Application to Dye-sensitized Solar Cell," *Journal of the Chinese Chemical Society,* vol. 60, pp. 81-84, 2013.

[69] G. Krylova, A. Brioude, S. Ababou-Girard, J. Mrazek, and L. Spanhel, "Natural superhydrophilicity and photocatalytic properties of sol-gel derived ZnTiO3-ilmenite/r-TiO2 films," *Physical Chemistry Chemical Physics,* vol. 12, pp. 15101-15110, 2010.

[70] I. S. N. N. H. Saim, "Structural and Electrical Properties of TiO2 Thin Film Derived from Sol-gel Method using Titanium (IV) Butoxide," *International Journal of Integrated Engineering,* vol. 3, pp. 1-35, 2010.

[71] C. Su, B. Y. Hong, and C. M. Tseng, "Sol–gel preparation and photocatalysis of titanium dioxide," *Catalysis Today,* vol. 96, pp. 119-126, 10/5/ 2004.

[72] P. Avila, M. Montes, and E. E. Miró, "Monolithic reactors for environmental applications," *Chemical Engineering Journal,* vol. 109, pp. 11-36, 2005.

[73] P. J. Walsh, "Aspects of environmental degradation and fracture in polymer films and fibers," Ph.D. 3289223, University of Massachusetts Amherst, United States -- Massachusetts, 2007.

[74] G. Ertl, H. Knözinger, and J. Weitkamp, *Preparation of Solid Catalysts*: WILEY-VCH Verlag GmbH, 2008.

[75] R. R. Arnts, "Reduction of Biogenic VOC Sampling Losses from Ozone via trans-2-Butene Addition," *Environmental Science & Technology,* vol. 42, pp. 7663-7669, 2008.

[76] J. Fick, L. Pommer, B. Andersson, and C. Nilsson, "Ozone Removal in the Sampling of Parts per Billion Levels of Terpenoid Compounds: An Evaluation of Different Scrubber Materials," *Environmental Science & Technology,* vol. 35, pp. 1458-1462, 2001.

[77] S. M. Saunders, M. E. Jenkin, R. G. Derwent, and M. J. Pilling, "Protocol for the development of the Master Chemical Mechanism, MCM v3 (Part A): tropospheric degradation of non-aromatic volatile organic compounds," *Atmospheric Chemistry and Physics,* vol. 3, pp. 161-180, 2003.

[78] L. Zhong, "Experimental Evaluation and Modeling of Photocatalytic Oxidation Air Cleaners," Ph.D., Building, Civil and Environmental Engineering, Concordia University, 2013.

[79] C.-S. Lee, L. Zhong, and F. Haghighat, "Development of a Parallel Test System for the Evaluation of UV-PCO Systems," in *7th International Cold Climate HVAC Conference*, Calgary, Alberta, Canada, 2012.

[80] K. Hashimoto, H. Irie, and A. Fujishima, "TiO2 Photocatalysis: A Historical Overview and Future Prospects," *Japanese Journal of Applied Physics,* vol. 44, pp. 8269-8285, 2005.

[81] D. S. Muggli, J. T. McCue, and J. L. Falconer, "Mechanism of the Photocatalytic Oxidation of Ethanol on TiO2," *Journal of Catalysis,* vol. 173, pp. 470-483, 1998.

[82] M. Miyauchi, A. Nakajima, A. Fujishima, K. Hashimoto, and T. Watanabe, "Photoinduced Surface Reactions on TiO2and SrTiO3Films: Photocatalytic Oxidation and Photoinduced Hydrophilicity," *Chemistry of Materials,* vol. 12, pp. 3-5, 2000.

[83] M. Sauer, "Photocatalyzed Oxidation of Ethanol and Acetaldehyde in Humidified Air," *Journal of Catalysis,* vol. 158, pp. 570-582, 1996.

[84] D. Muggli, "Mechanism of the Photocatalytic Oxidation of Ethanol on TiO2," *Journal of Catalysis,* vol. 173, pp. 470-483, 1998.

[85] D. T. Tompkins, B. J. Lawnicki, W. A. Zeltner, and M. A. Anderson, "Evaluation of photocatalysis for gas-phase air cleaning - Part 1: Process, technical, and sizing considerations," *Ashrae Transactions 2005, Vol 111, Pt 2,* vol. 111, pp. 60-84, 2005.

[86] W. Xu and D. Raftery, "Photocatalytic Oxidation of 2-Propanol on TiO2 Powder and TiO2 Monolayer Catalysts Studied by Solid-State NMR," *The Journal of Physical Chemistry B,* vol. 105, pp. 4343-4349, 2001.

[87] C.-P. Chang, J.-N. Chen, and M.-C. Lu, "Characteristics of photocatalytic oxidation of gaseous 2-propanol using thin-film TiO2 photocatalyst," *Journal of Chemical Technology & Biotechnology,* vol. 79, pp. 1293-1300, 2004.

[88] S. Larson, "Transient Studies of 2-Propanol Photocatalytic Oxidation on Titania," *Journal of Catalysis,* vol. 157, pp. 611-625, 1995.

[89] F. Benoit-Marquié, U. Wilkenhöner, V. Simon, A. M. Braun, E. Oliveros, and M.-T. Maurette, "VOC photodegradation at the gas–solid interface of a TiO2 photocatalyst," *Journal of Photochemistry and Photobiology A: Chemistry,* vol. 132, pp. 225-232, 2000.

[90] X. Ye, D. Chen, J. Gossage, and K. Li, "Photocatalytic oxidation of aldehydes: Byproduct identification and reaction pathway," *Journal of Photochemistry and Photobiology A: Chemistry,* vol. 183, pp. 35-40, 2006.

[91] J. Cunningham and B. K. Hodnett, "Kinetic studies of secondary alcohol photo-oxidation on ZnO and TiO2 at 348 K studied by gas-chromatographic analysis," *Journal of the Chemical Society, Faraday Transactions 1,* vol. 77, p. 2777, 1981.

[92] T. M. Twesme, "Oxidation of Light Alkanes Using Photocatalytic Thin Films," Civil & Environmental Engineering, University of Wisconsin-Madison, 2006.

[93] J. I. Brauman and L. K. Blair, "Gas-phase acidities of alcohols. Effects of alkyl groups," *Journal of the American Chemical Society,* vol. 90, pp. 6561-6562, 1968.

[94] "MDHS 80: Volatile Organic Compounds in Air - Laboratory method using diffusive solid sorbent tubes, thermal desorption and gas chromatography. ," in *Method for the Determination of Hazardous Substances*, ed: Health and Safety Laboratory, 1995.

[95] J. M. Winterbottom and M. B. King, *Reactor design for chemical engineers*. Cheltenham, U.K.: Stanley Thornes, 1999.

Appendix 1: Physical Property Tables

Table A1-1. Physicochemical Properties of VOCs

Class	Name	Formula	CAS#	MW	Assay[♀]	Density (g/cm^3)	VP (kPa)	B.P.	IP[*] (eV)	Dielectric constant[†]
Alkanes	iso-Pentane	C_5H_{12}	78-78-4	72.15	95 %	0.616	76.99	28	10.32 ± 0.05	1.84
	n-Pentane	C_5H_{12}	109-66-0	72.15	99.7 %	0.626	57.9	36	10.28 ± 0.10	1.84
	n-Hexane	C_6H_{14}	110-54-3	86.18	99 %	0.6548	17.6	68	10.13 ± 0.10	1.88
	n-Heptane	C_7H_{16}	142-82-5	100.2	99.4 %	0.6795	5.33	98	9.93 ± 0.10	1.92
	n-Octane	C_8H_{18}	111-65-9	114.2	95 %	0.703	1.47	125	9.80 ± 0.15	1.95
	n-Nonane	C_9H_{20}	111-84-2	128.3	98.5 %	0.718	1.33	150	9.71 ± 0.10	1.97
	Undecane	$C_{11}H_{24}$	1120-21-4	156.3	99 %	0.74	0.55	195	9.56	1.99
Alcohols	Ethanol	C_2H_6O	64-17-5	46.07	99 %	0.789	5.95	78	10.48 ± 0.07	23.80
	n-Propanol	C_3H_8O	71-23-8	60.1		0.803	1.99	98	10.22 ± 0.06	3.36
	1-Butanol	$C_4H_{10}O$	71-36-3	74.12	99.4 %	0.81	0.74	118	9.99 ± 0.05	17.80
	sec-Butanol	$C_4H_{10}O$	78-92-2	74.12	99.8 %	0.808	1.67	99	9.88 ± 0.03	17.51
	3-Pentanol	$C_5H_{12}O$	584-02-1	88.15	98 %	0.815	1.1	115	9.76 ± 0.02	14.02
	Methanol	CH_4O	67-56-1	32.04	99.9 %	0.7918	13.02	65		32.20
	p-Xylene	C_8H_{10}	106-42-3	106.2	99.9 %	0.861	-	138.4		2.27
	MEK	C_4H_8O	78-93-3	72.11	99.9 %	0.805	-	79.6		18.85
	Toluene	$C_6H_5CH_3$	108-88-3	92.14	99.9 %	0.87	-	111		2.39

* Data Source: NIST Chemistry WebBook Database;
[♀]Chemical manufacturer data sheet; [†]Dielectric constant at 20ºC (Ref. IHS Databases)

Appendix 2: UV Lamps Irritation Test

The U-shaped Ultraviolet (UV) lamps (Ster-L-Ray®, Atlantic Corp.) were used to produce enough irradiation in the system with two different wavelengths of 185 and 254nm. The irradiation of UV lamps with 185nm wavelength (also known as VUV lamps) is strongly adsorbed by oxygen molecules in the air that leads to formation of superoxide radicals in the air.

The different numbers of UV lamps were to generate different levels of irradiation intensity in each duct. However, the lamps configuration were not fixed and they were changed for some specific tests to compare the system performance for different light intensities.
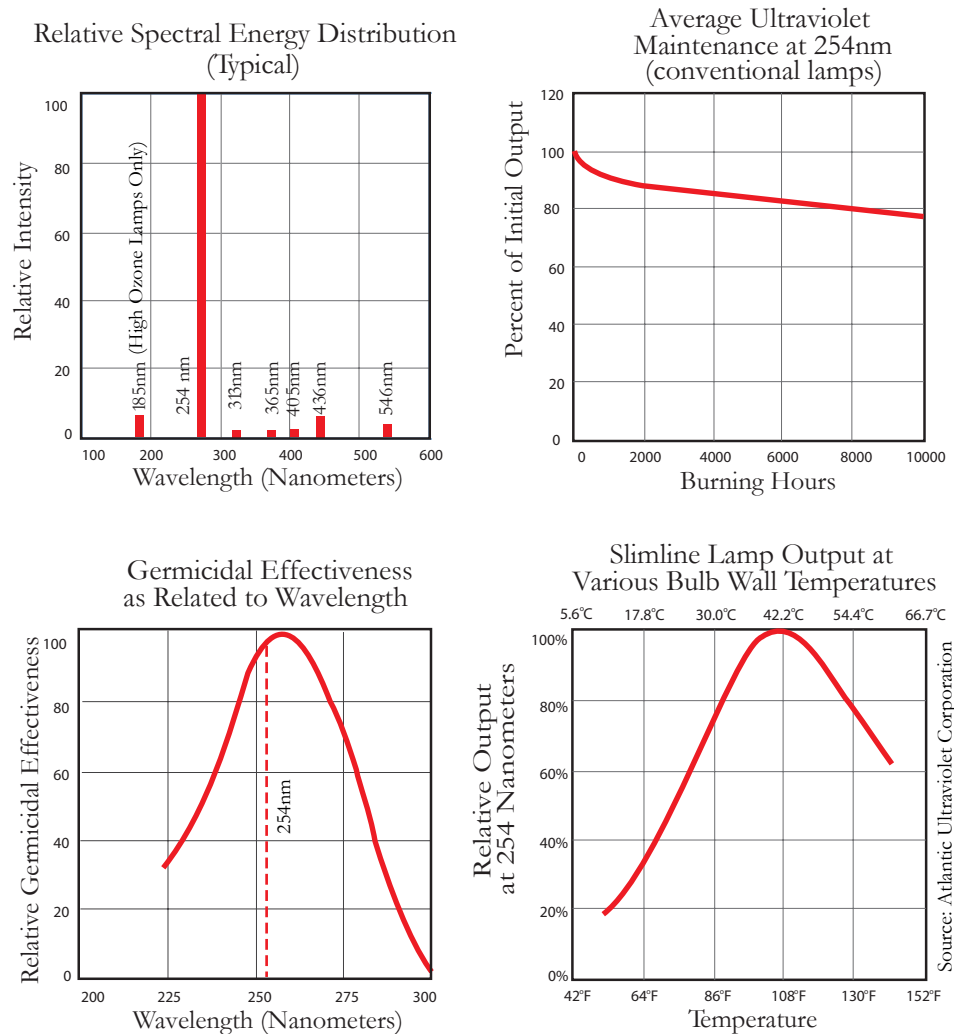
Figure A2-1. UV lamps operating characteristics

The irradiation of UV lamps in each channel was measured individually. An irradiation test procedure was arranged that consisted of a welded wire mesh screen (1×1 ft.). The screen was made of 36 equal grids (2×2 in. each one) to hold the photometer sensors in nine different distances inside the duct. The sensors were attached to certain locations on the screen. The mesh was installed at different distances from UV lamps. It should be noted that the irradiation tests were done in empty ducts without any barrier between the UV lamps and the detector. The detector always installed directly faced at two inch distance from UV lamps.

The radiometer was a handheld radiometer measurement system (ILT1400-A, International Light). The detector (NS185, International Light) was built for low intensity irradiation that can measure ozone producing germicidal lamps at 185nm (peak spectral response) and itself has spectral range of 165-200nm.

For 254nm irradiation measurement test, a separate UV radiometer (Steril-Aire) was used to monitor UV lamps irradiation of each duct. The 254nm sensors have been connected to UV radiometer and then linked to the DAS system to record the measured irradiation during the experiments. The *Agilent VEE Pro* software was modified to record the irradiation test data set in parallel to other data such as flow rate and temperature data.

Table A2-1. UV lamps specifications (adopted from Atlantic Ultraviolet Corp.)

Lamp Description		Lamp Length (mm)	Lamp Watts[1]	Current (mA)	UV Output		Ozone output	Effective Life (hrs)
Ozone Free	Ozone Producing				Total Watts[2]	($\mu W/cm^2$) @ 1 meter		
G18T5L/U	G18T5VH/U	201	18.4	425	5.8	59	1.6	10,000

(1) Wattage is lamp watts only and does not include ballast loss;
(2) Ultraviolet output at 254 nanometers at 100 hours and 80°F (approximate).

To determine the profile of irradiation of UV lamps for each duct, the light intensity was measured at nine different points at 2 inch distance from bulbs cross section area (Figure A2). The irradiation tests could provide a good evaluation of the irradiation intensity on the catalyst surface for each duct and they determined the uniformity of illumination on the catalyst surface. The nine test points distributed evenly on a metal mesh and they represent the location of UV sensors over the entire of duct cross section area.

Figure A2 shows a front view of sensors location on the installed wire mesh that used for the UV irradiation tests.
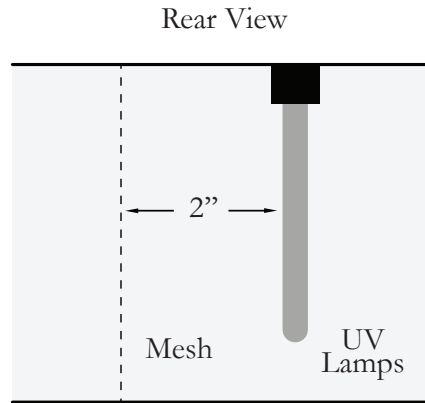
Rear View

Figure A2-2. Wire mesh screen position inside the duct

The irradiation measurements were taken with 5 seconds time interval for three minutes period. The irradiation results of three ducts are presented in Figure A2-3.
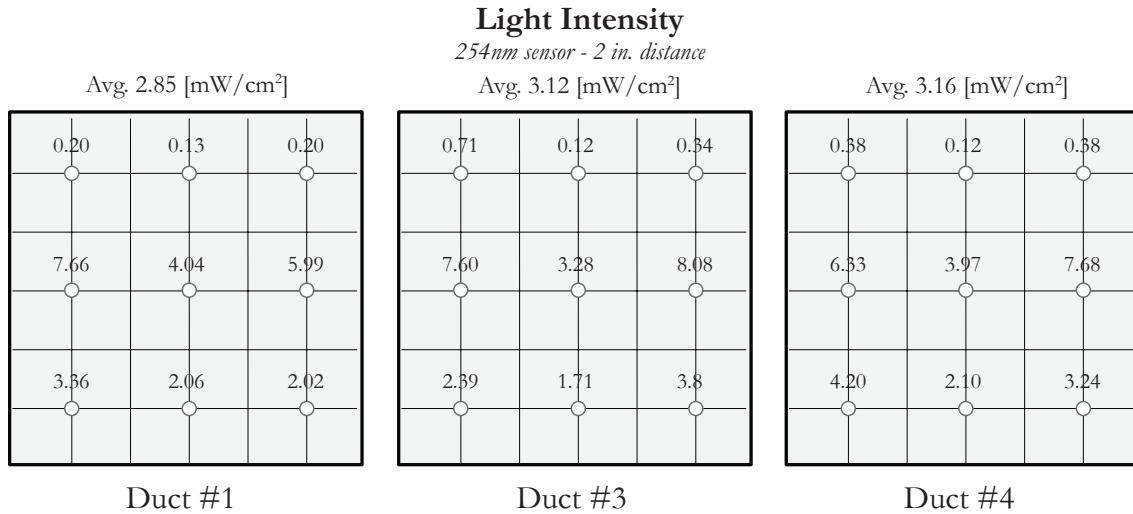
Light Intensity
254nm sensor - 2 in. distance

| Avg. 2.85 [mW/cm²] | Avg. 3.12 [mW/cm²] | Avg. 3.16 [mW/cm²] |

| Duct #1 | Duct #3 | Duct #4 |

Figure A2-3. UV light intensity profile for different test ducts with 254nm sensor

Appendix 3: Experimental Analysis Method

A3.1. ATD-GC/MS

A *PerkinElmer TurboMatrix 650 Automated Thermal Desorber* (ATD) was coupled to a *PerkinElmer Clarus 500 GC/MS* as the analytical instrumental platform to quantify and identify the samples in this experiments. Ultra high quality 99.99% helium gas (Praxair Inc.) was used as the carrier gas.

The system was calibrated with standard prepared sorbent tubes. The tubes are prepared by injecting the aliquots of standard solution onto a clean sorbent tube. The tube is fitted into an injection unit through an inert gas purge (high purity helium gas) at 200 mL/min with different injection concentration (1-5 µL) diluted mixture standard solution [94]. For all analyzed tubes, the concentration variation was less than 5%, representing an error of less than 35 ppb. The system performance was evaluated each day with calibration standard tubes. Figure A3-1 shows a schematic diagram of packaging content and sorbent geometry inside a typical sampling tube. *Air Toxics®* tubes are suitable for wide range of VOCs such as aliphatic hydrocarbons, aromatic, esters, ketones, alcohols with volatility range of n-C3 to n-C12 (EPA TO-14). It should be noted that very volatile compounds should be sampled on higher sample volume. The sorbent material composed of at least four different sorbent material which arranged from weakest to strongest adsorption strength to the inlet tube. The sorbent was fixed with a steel mesh and graphitized carbon black in the tube. The hydrophobic structure of sorbent in the Air Toxics® reduces the water uptake during the sampling.
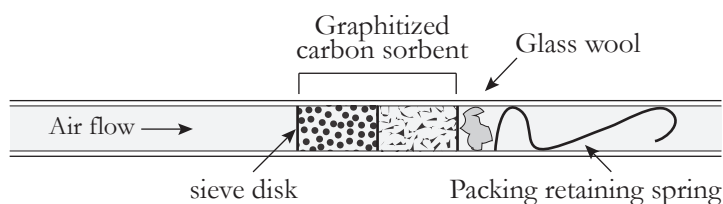

Figure A3-1. Internal geometry of a typical sorbent sampling tube

The upper concentration limit of sampling volume was determined based on capacity of sorbent tube and linear dynamic range of GC's column and detector. The lower limit depends on detector noise and analyte blank.

The GC oven temperature was defined based on the boiling point of the test compounds where it should not be below the boiling point; at below this temperature, the compound would condense through the column and no peaks would be observed in the test results. The maximum temperature was set based on the lower margin of column temperature limits; above the maximum temperature the column could be damaged. The GC column temperature limit was minus 40 to 260ºC. By selecting an appropriate temperature between these two limits would allow the compounds to pass the column at a short time, but it also should allow the compounds spectral peaks correctly become separate and do no overlapped.

The ATD test conditions were as following: The sample tube was desorbed for 4 minutes at 250ºC; The sample was collected into a cold trap. Then, the cold trap desorbed at 300ºC across a heated transfer line onto PerkinElmer Elite-VMS (60 m × 0.32 mm; thickness: 1.80μm). GC oven program had initial temperature of 40ºC with a 1 min hold, the oven was ramped at 12 deg/min to 100ºC with 3 min hold; and finally ramped at 9 deg/min to 200ºC where it was hold for 2 minutes. The mass spectrometer scanned from m/z 50 to 150 with scan time of 0.15 and inter-scan delay of 0.05 seconds.
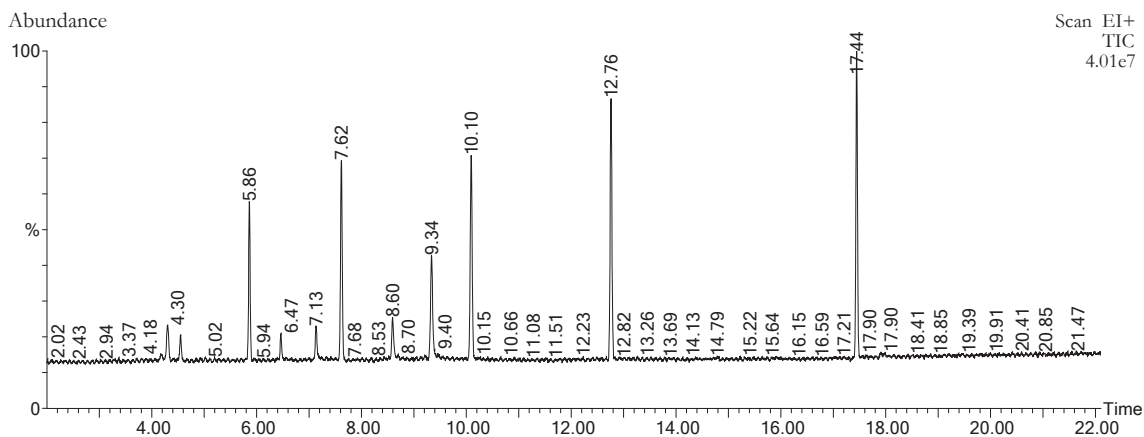

Figure A3-2. GC/MS peak response with 5.0 ng of a reference standard

For calibration calculations, five different concentration standard solutions were prepared by diluting primary VOC standard with ethanol. These five concentrations represent five calibration points in the calibration curves. Figure A3-2 shows an example chromatogram of a 5.0 ng standard injection for the calibration analysis. Individual compounds in the chromatogram were determined by doing a NIST library search of the acquired mass spectral data.

Peak area was used to calculate analyzed amount of VOCs in the sample tube. The peak ratio for each compound in the sample was determined by dividing the peak area of the test VOC by the peak area of the standard. The mass amount of each VOC was calculated from the calibration plot with the following equation:

$$C_{VOC}[ng] = \frac{y\,(peak\,area\,ratio) - b^{\,y=ax+b}}{a}$$

Table below shows the calibration curve equation for all the calibrated compound:

Table A3-1: GC Calibration Curve Equations

Name	Calibration Curve	R^2
Ethanol	M = 35055.2 × (A) + 3453.02	0.994
2-propanol	M = 102139 × (A) + (-4616.05)	0.994
1-butanol	M = 54526.2 × (A) + (-31990.5)	0.986
2-butanol	M = 132969 × (A) + (-25940.4)	0.982
3-pentanol	M = 117244 × (A) + (-18266.4)	0.994
Pentane	M = 16401.0 × (A) + (-2988.13)	0.996
n-hexane	M = 93581.1 × (A) + 319.547	0.990
2-butanone	M = 35097.9 × (A) + (-12960.6)	0.990
n-heptane	M = 56370.3 × (A) + (-15921.1)	0.996
n-octane	M = 64932.1 × (A) + (-19010.6)	0.996
n-decane	M = 118131 × (A) + (-25652.0)	0.995
p-xylene	M = 174870 × (A) + (-40152.4)	0.998
Toluene	M = 195735 × (A) + (-47371.7)	0.992

M: Analyte Mass (ng); A: Peak Area

The recovered mass from samples was determined by reference to calibration standard curves. The concentration of analyte, C_{VOC} (mg m^{-3}) in the samples was calculated as following:

$$C_{VOC} = \frac{(m - m_{blank})10^3}{U \times t}$$

m is the weight of VOC on sample and blank tube; U is the uptake time (ml min^{-1}) and t was sampling time (min).

A3.2. HPLC

The *PerkinElmer Flexar HPLC* with *Flexar UV-Vis* detector with 360nm wavelength. The column was carefully selected to exhibit excellent peak shape for a wide range of compounds, especially with aldehydes and ketones. The detailed analytical conditions for the Flexar LC is summarized in Table A4-1. The developed method was used to determine the DNPH derivatives (aldehyde and ketones) in the sample solution. Sampling procedure was adapted from EPA method TO11-A. The carbonyl compounds were collected onto LpDNPH S10L cartridge. The samples content were extracted with acetonitrile from LpDNPH cartridges.

Table A3-2: Detailed HPLC system conditions

Autosampler:	Flexar FX (without Peltier)		
	200 μL loop and partial loop mode: 45 μL		
	Injection volume: 20 μL Sampling rate: 5 pts/s		
Pump:	**Flexar FX pump**		
	Step	**Time** (min)	**Flow rate** (mL/min)
	Equilibrium	0.1	1
	Run	10.0	1
Mobile phase:	A: acetonitrile; B: water (HPLC grade solvent)		
Detector:	Flexar UV/VIS		
	Analytical wavelength: 360nm		
Column:	Brownlee® Validated C18, 5μm, 4.6 × 150 mm		
	Column Temperature: 40 °C		
Gradient Program:	**Run Time** (min)	**%A**	**%B**
	6	70	30
	3	100	0
	4	70	30

The system was calibrated with a primary standard solution (TO11/IP-6A) that was a Aldehyde/Ketone-DNPH derivative (15 µg/mL each component in acetonitrile). The standards were procured with dilution of stock standard into 2, 5, 20, 50% with acetonitrile. Furthermore, the diluted solutions were injected with two different volume of 10 and 20 µL. These procedure produced eight levels of concentration which represents eight calibration points (3, 6, 7.5, 15, 30, 75, 150 ng).

Table A3-3: HPLC Calibration Equations

Name	RT (min)	Calibration Curve	R^2
Formaldehyde	2.7	M = 2.905(E-5) × (A) - 0.465	1.00
Acetaldehyde	3.2	M = 3.860(E-5) × (A) - 0.580	1.00
Acrolein	4.1	M = 3.413(E-5) × (A) + 1.610	0.99
Acetone	4.3	M = 6.297(E-5) × (A) - 3.321	0.99
Propionaldehyde	4.6	M = 5.299(E-5) × (A) - 2.409	0.99
Crotonaldehyde	5.4	M = 5.62 (E-5) × (A) - 0.50	0.99
Butyraldehyde	6.1	M = 6.06 (E-5) × (A) - 0.681	0.99
Benzaldehyde	6.6	M = 8.08 (E-5) × (A) - 0.501	0.99
Isovaleraldehyde	7.9	M = 6.97 (E-5) × (A) + 0.25	0.99
Valeraldehyde	8.4	M = 7.102 (E-5) × (A) + 0.712	1.00
o-Tolualdehyde	9.02	M = 9.53 (E-5) × (A) + 1.652	0.99
m-Tolualdehyde	9.1	M = 8.98 (E-5) × (A) + 1.06	1.00
p-Tolualdehyde	8.8	M = 1.12 (E-5) × (A) - 3.211	0.99
Hexanal	8.8	M = 4.761 (E-5) × (A) - 0.50	1.00
Dimethylbenzaldehyde	-	M = 4.76 (E-5) × (A) - 0.912	0.99

M: Analyte Mass (ng); A: Peak Area

A3.3. Photoacoustic Multi Gas Analyzer

The photoacoustic multi-gas monitor (INNOVA and B&K, Model 1312 and 1302 respectively) were used to measure the concentration of test compounds in upstream and downstream during the experiment. A certain volume of the pure liquid chemical was injected by a syringe infusion pump. The volumetric flow rate was controlled with a mass flow controller (Matheson Model 8274) and the flow was adjusted regularly with a NIST calibrated flow calibrator (Definer 220). Different injection rate was applied to generate

different concentration of test compounds to calibrate the INNOVA. Figure A3.3 shows the describes the calibration system details.
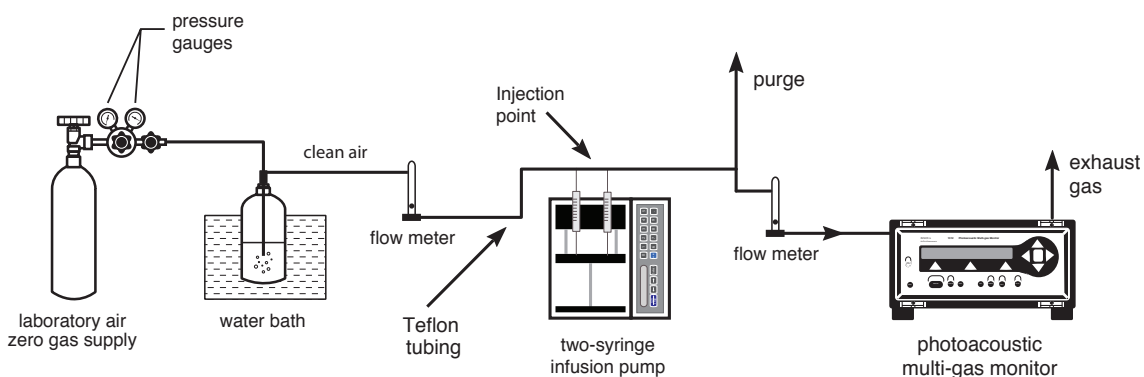

Figure A3.3 – Standard calibration system of photo-acoustic multi-gas monitor (1302 & 1312)

The analyzer measurement principle was based on infrared radiation and acoustic signals. The sample gas sucked into the analyzer by a pump and sealed through an analysis cell chamber. A pulsating Infrared light passed through an optical filter and it transmitted into the analysis cell. The transmitted gas selectively absorbed by the gas molecules and creates steady oscillation in the temperature of the sealed gas (because of light pulsation). This causing a decrease and increase in pressure of sealed gas chamber. These acoustic signals can be measured by two microphones that connected to the analysis cell which is directly proportional to the concentration of sample gas in the cell. It can measure concentration of up to five different components that depends on which type of optical filters installed for the device. The installed standard filters on the analyzer were SF6, TVOC (Calibrated for Toluene), Formaldehyde, CO, CO_2 and water vapor.

The INNOVA was pre-calibrated with toluene gas as standard equivalent compound for the total hydrocarbon (TVOC). The instrument was also monitored the concentration of total formaldehyde, CO, CO_2 and H_2O. Since the sensitivity and response factor of optical filters was different for different compounds, the analyzer was calibrated for each individual compound for the experimental operation conditions. The calibration concentration was in the range of 0.05-1.0ppm 30% RH and 21˚C.

The quantification of individual intermediate species was analyzed from collected samples by ATD/GC-MS and HPLC. The measurement uncertainty for individual analyzes was estimated to be ±10%. The details of GC-MS and HPLC calibration can be found in Appendix 3, 4.

Appendix 4: Characterization Data

A4.1. Surface Area Measurement and Particle Size Analysis

The specific area of catalyst was determined from total surface area of the catalyst per catalyst weight (S_t/w). To determine the total surface area with BET method, it was necessary to find the weight of a adsorbate gas monolayer according to following equation:

$$\frac{1}{W\left[(P_o - P) - 1\right]} = \frac{1}{W_m . C} + \frac{C-1}{W_m . C}\left(\frac{P}{P_o}\right)$$

On the left-hand, the ratio of weight of adsorbed gas (W) at a relative pressure (P_o/P) associated to the weight of adsorbate monolayer on the surface and BET C constant that indicates the ratio of adsorption/desorption of first adsorbate monolater. Next, the total surface area was obtained from:

$$S_t = \frac{W_m N A_{cs}}{MW}$$

Nitrogen gas was used as the typical adsorbate with average C value of 50-250 for most solid catalysts and the Acs value for nitrogen is 16.2 Å2 at 77 K (-196°C).

The BET surface area of two different types of fiberglass PCO catalysts with TiO_2 were determined with nitrogen gas adsorption isotherm, figure A4-1(a). The BET surface area of FG-I and FG-II determined as 98.89 and 10.73 m^2/g (±10%) respectively. The cumulative surface area and cumulative pore volume were determined from desorption isotherm using the DFT (Monte Carlo) model simulations. The DFT model could accurately predict the behavior of fiber glass surface with micropores and mesopores pores.
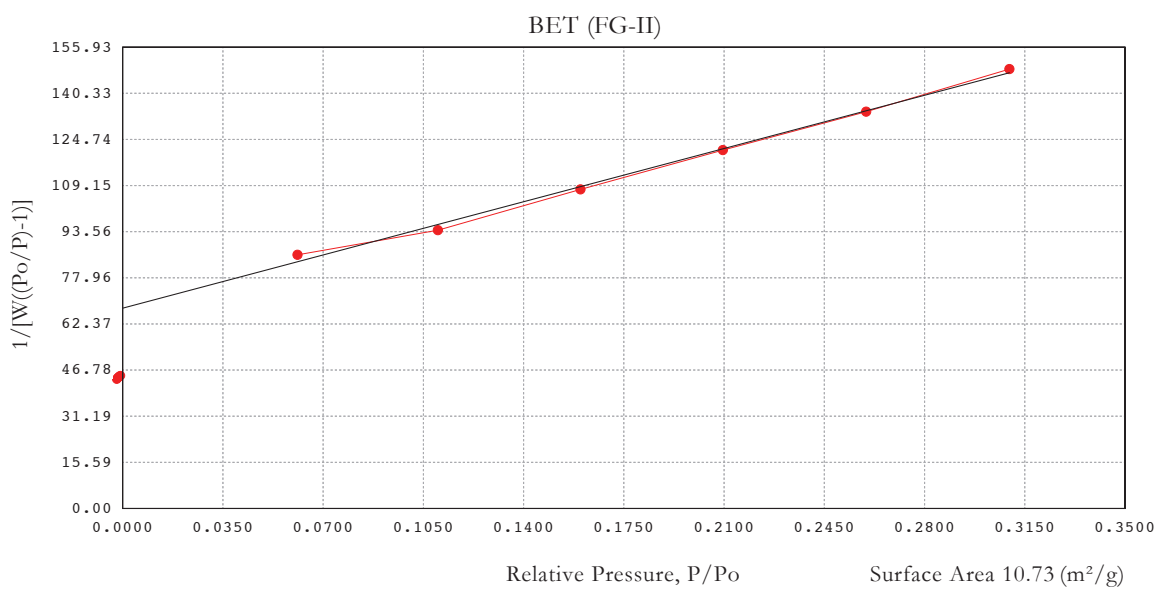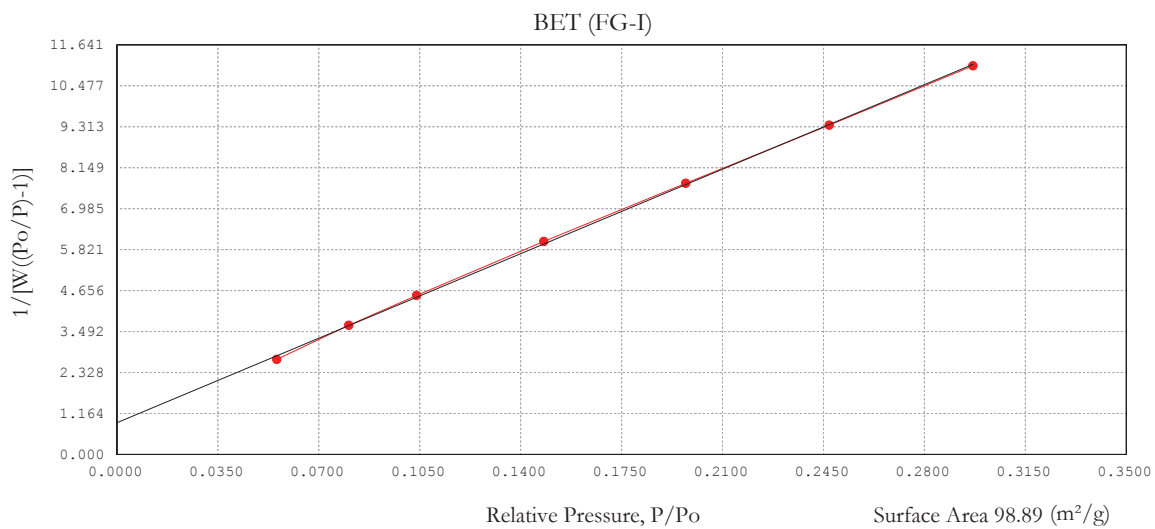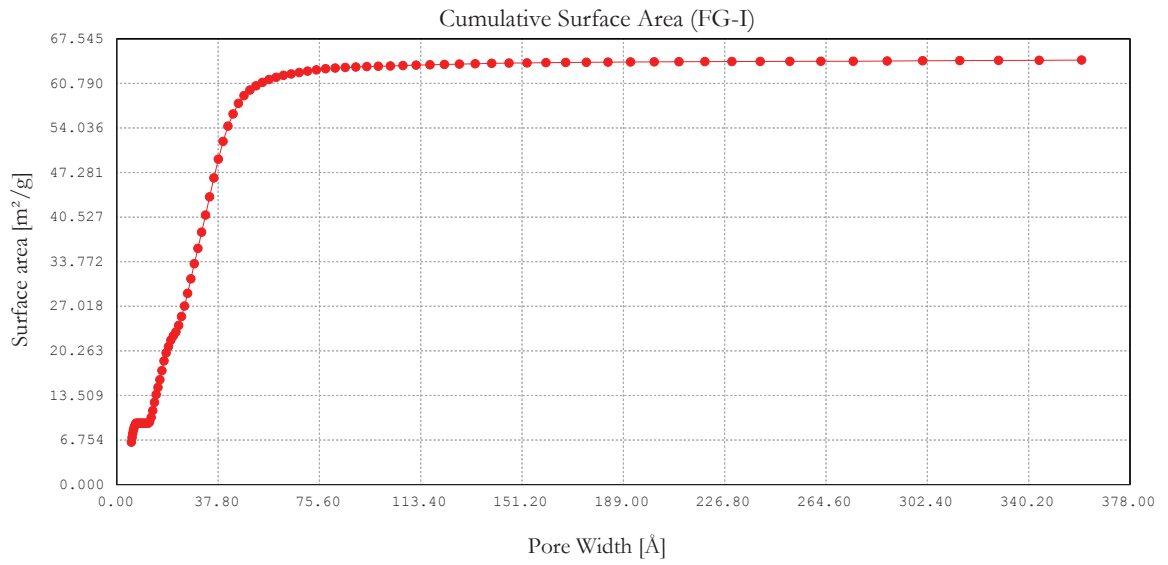
Figure A4-1a: BET Surface area plot for FG PCO catalysts

Cumulative Surface Area (FG-I)

Cumulative Surface Area (FG-II)

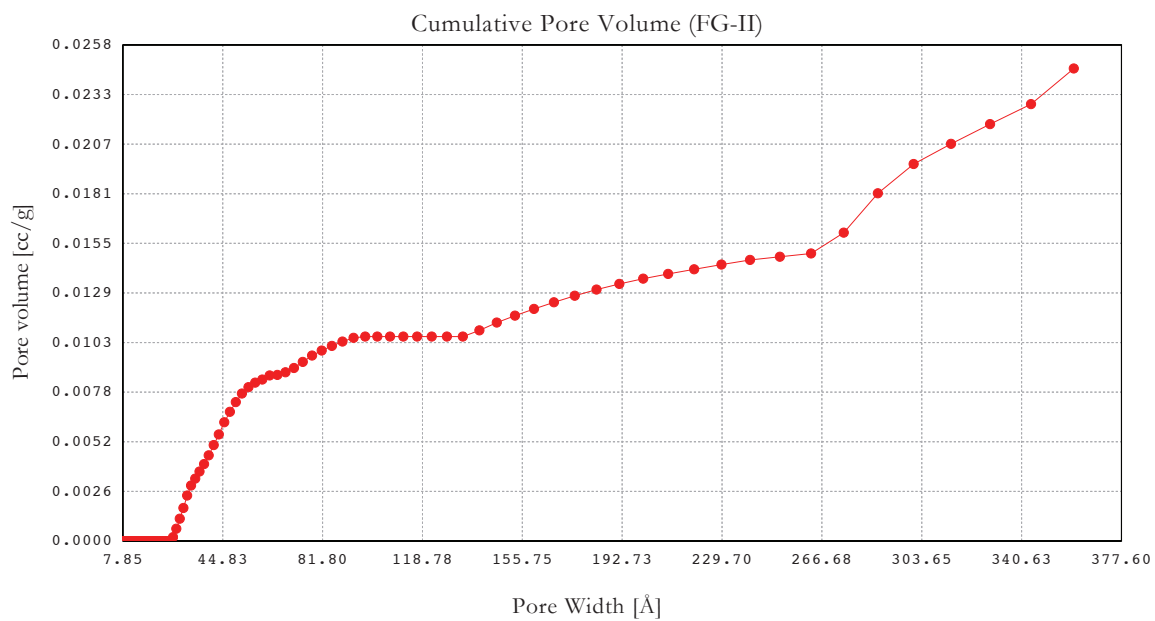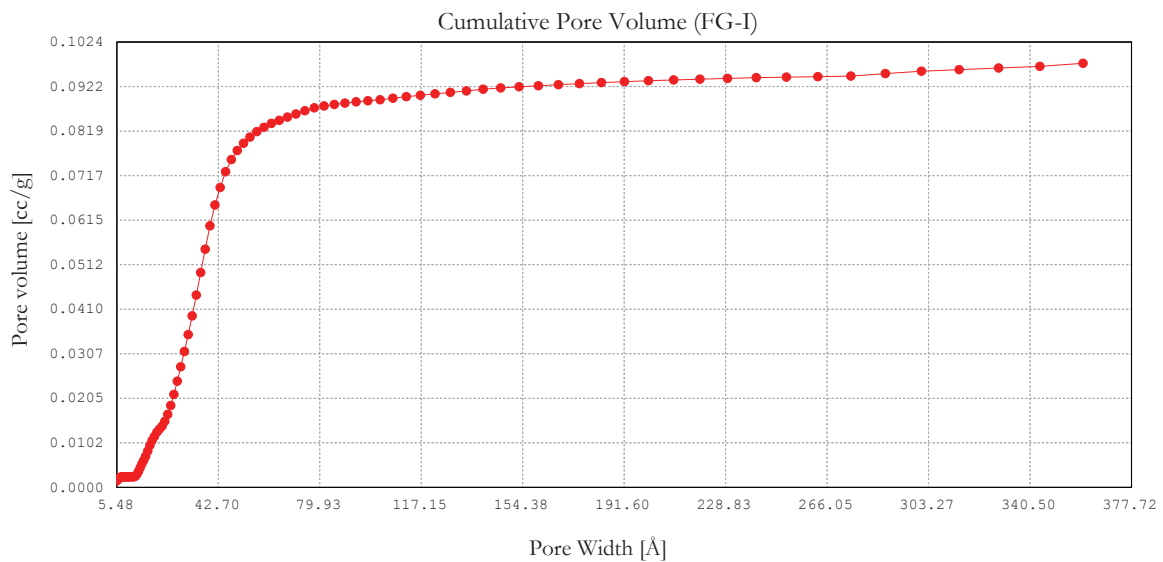Figure A4-1b: Cumulative surface area plot for PCO types FG-I, II

107

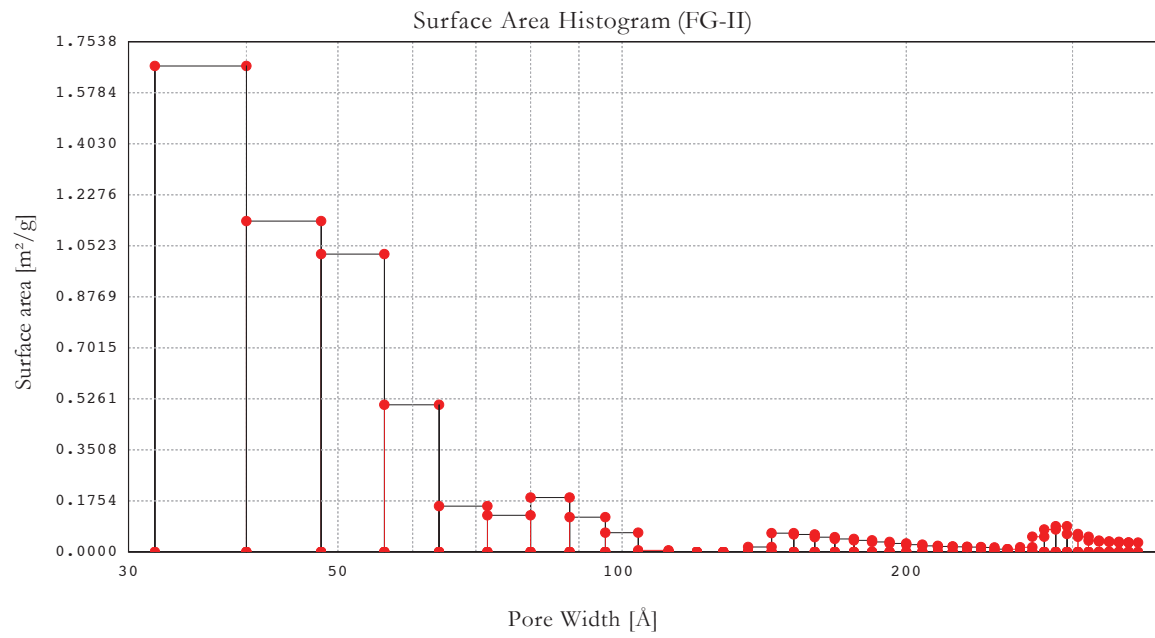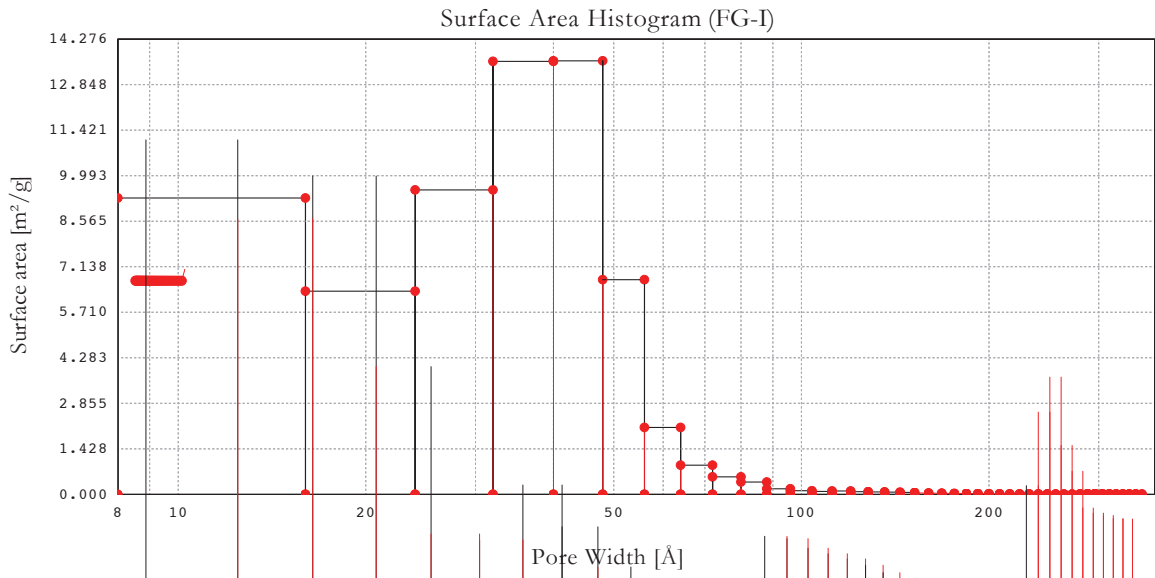Figure A4-1c: Cumulative pore volume plot for PCO types FG-I, II

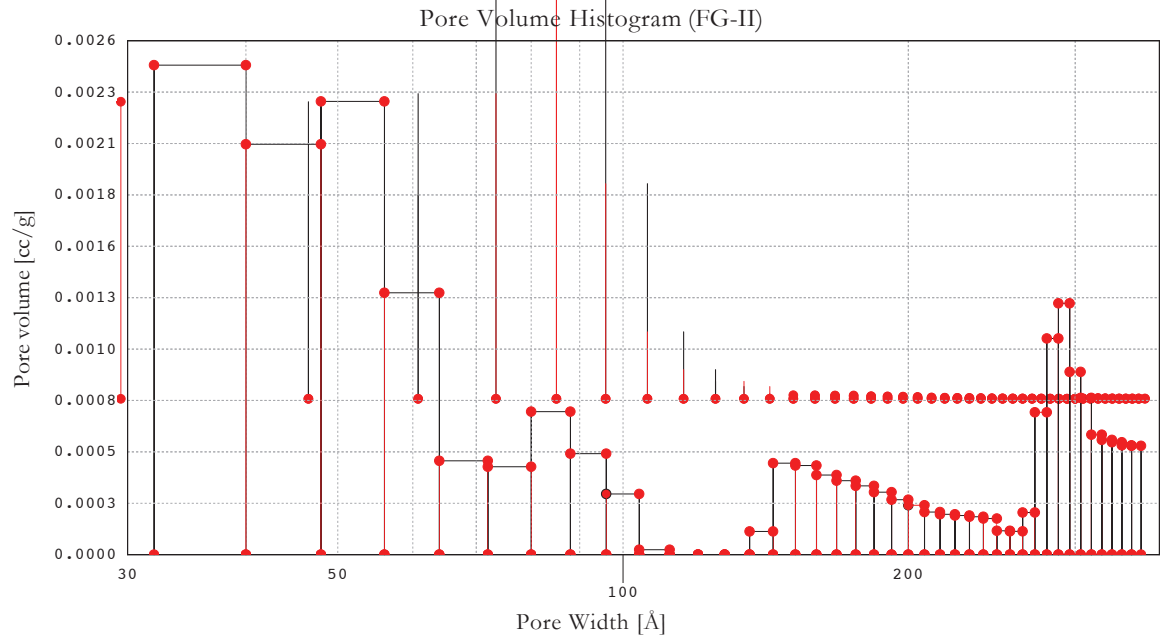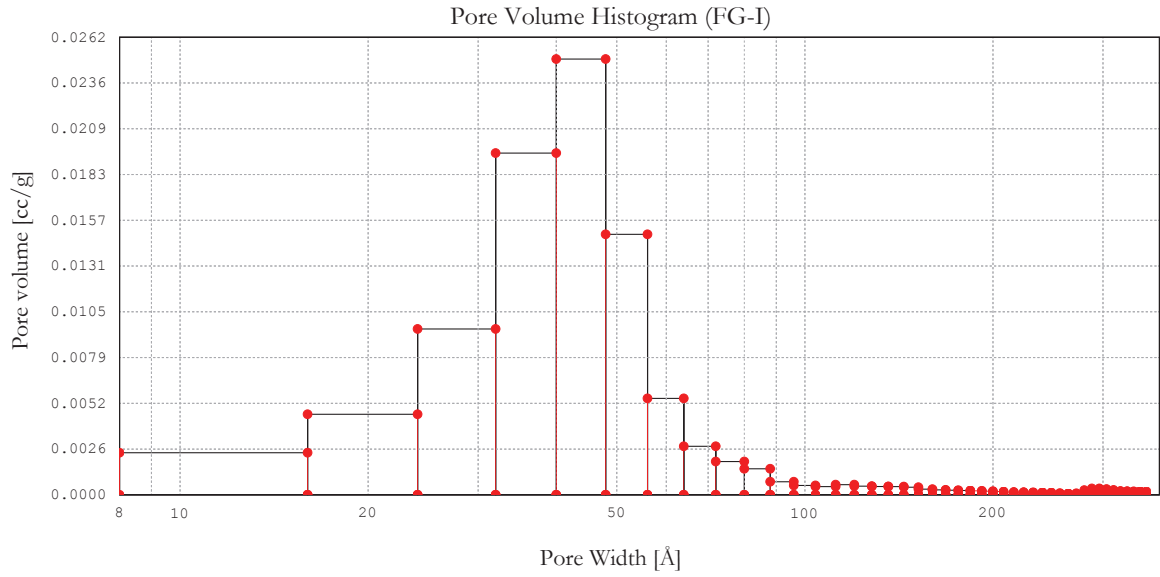Figure A4-1d: Surface area histogram for PCO types FG-I, II

Figure A4-1e: Volume histogram for PCO types FG-I, II

A4.2. X-ray diffraction

The X-ray powder diffraction (XRPD) experiment was used to identify the crystal phase and estimate the ratio of anatase-rutile of each phase. The experiments were carried out on a diffractometer with Cu Kα ($\lambda_{K\alpha}$ = 0.15418nm) with source of 45 kV and 40mA generator power. The diffraction pattern was recorded from 5 to 90º *2θ* in the step scanning mode with a step size of 0.02º and scan rate of 0.01333 and count time of 2s. The PDF+2 powder diffraction files database from the International Center for Diffraction Data was used for data analysis.
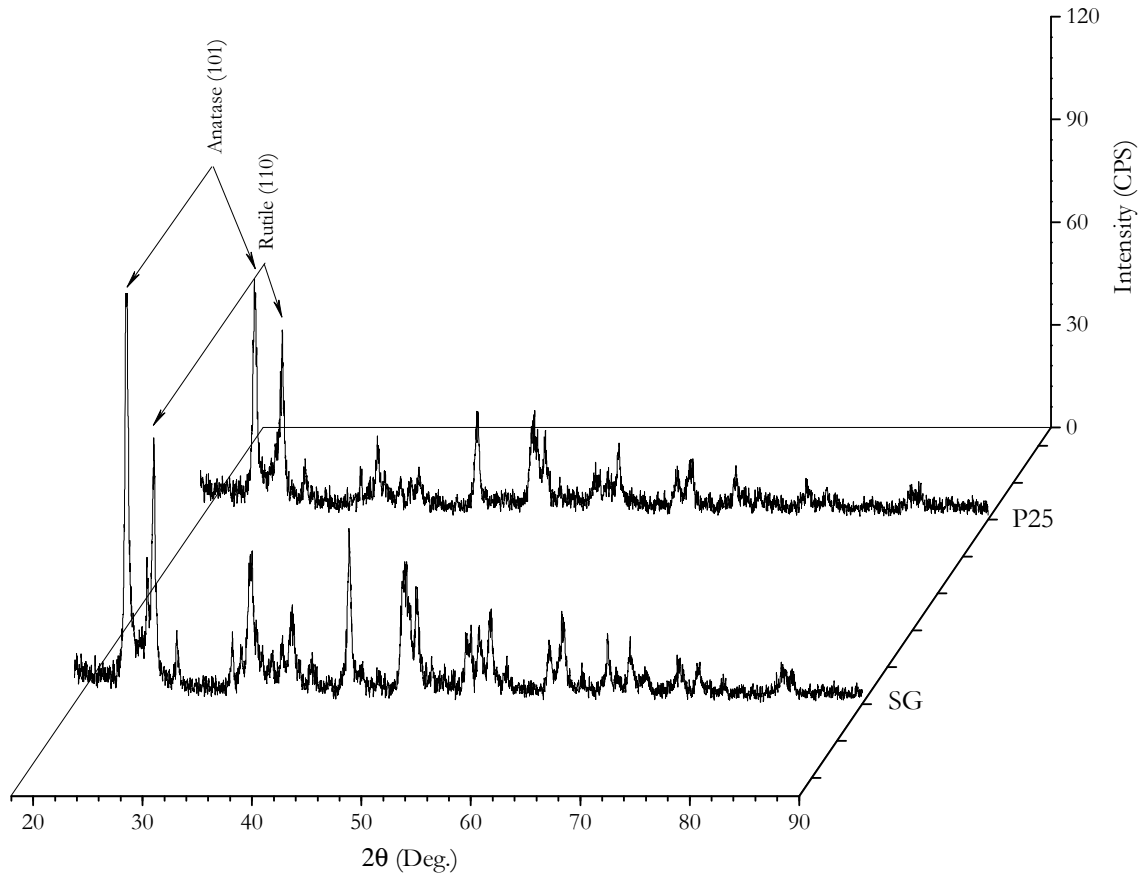

Figure A4-2. XRD pattern of two different type of TiO_2

Figure A4-2 shows XRD pattern of Degussa P25 nano particles and synthesized SG TiO_2 used for this study. The diffraction peaks are matched to a reference pattern from PDF ICDD database (21-2172). The two annotated peaks indicate the structure of titanium dioxide. It is obvious that the crystalline structures composites of anatase and rutile

phase. The diffraction intensity of anatase phase for TiO_2 (SG) is higher ratio in compare to the rutile phase. The diffraction peaks at 25.2, 38, 48.2, 55 and 62.5 characterizes different planes of anatase TiO_2 morphology and other peaks at 27.5, 36, 54 and 69 are the identifier of diffraction for different rutile surfaces.

The crystalline phase ratio was estimated by: $x = 1 / (1 + 0.8 (i_A/i_R))$ where x is the weight fraction of rutile phase; i_A and i_r are the diffraction peak intensity of anatase (101) and rutile (110) plane. The particle size was determined by *Scherrer* equation ($\tau = 0.9\lambda / \beta.\cos\theta$) where τ is the diameter of the average particles, λ is the wavelength of X-rays. The calculated average particle size was about 20nm for P25 and 35 for SG samples. The higher peak intensity of SG-TiO_2 indicates the higher coating quality, which still have similar elemental composition, comparable to P25-TiO_2 crystallite composition ratio.

Appendix 5: Multichannel Ozone Monitor

The ozone level of flowing gas was measured with a multichannel ozone monitor, 8 channel UV photometric ozone monitor (Model 465L, Teledyne Instruments). It was connected to the sampling ports near the INNOVA's sampling port. The multichannel ozone monitor was capable to monitoring up to eight parallel channels with high accuracy as low as ppb ozone level concentration. It sampled the upstream and downstream of all four ducts to monitor the ozone concentration through the test period. The ozone monitor measurement principle was based on absorption of 254nm UV light that results from an internal electronic resonance of the detected ozone molecules. Inside the instrument, a mercury lamp was located that emits UV lights at the 254nm wavelength. The emitted light from the UV lamps passed through a hollow quartz tube which already filled with the sampled gas, the tube content replaced with the scrubbed gas that is free from ozone molecules, the intensity difference between the light passed the sampled gas and scrubbed gas used to calculate the ozone concentration of test gas. This intensity difference can be expressed as ratio of the light intensities, which defines the basics of Beer-Lambert equation:

$$C_{O_3} = -\frac{10^9}{\alpha \times l} \times \frac{T}{273} \, [K] \times \frac{29.92}{P} \, [in\,Hg] \times \ln\frac{I}{I_o}$$

Where C_{O3} is the ozone concentration [ppb]; α is absorption coefficient; l is path length that light passed through the test gas and I/Io is the intensity ratio of light passed through the test gas and scrubbed gas (ozone free).

Considering the above equation, the concentration of ozone mainly depends on intensity ratio; temperature and pressure are the secondary parameters that can affect the intensity of the sample. The density can change the amount of absorbed ozone in the quartz tube. This can affect the light intensity which affect calculated ozone concentration. However, temperature and pressure are almost constant for the lab environment.